UNIVERSIDADE FEDERAL DE SÃO CARLOS
CENTRO DE CIÊNCIAS EXATAS E DE TECNOLOGIA
PROGRAMA DE PÓS-GRADUAÇÃO EM CIÊNCIA E ENGENHARIA DE MATERIAIS

FRACTURE OF REFRACTORIES AT ROOM AND ELEVATED TEMPERATURES ANALYZED WITH WEDGE SPLITTING TESTS AND IMAGE CORRELATION

Rafael Vargas Maginador

São Carlos-SP
2024

UNIVERSIDADE FEDERAL DE SÃO CARLOS
CENTRO DE CIÊNCIAS EXATAS E DE TECNOLOGIA
PROGRAMA DE PÓS-GRADUAÇÃO EM CIÊNCIA E ENGENHARIA DE MATERIAIS

FRACTURE OF REFRACTORIES AT ROOM AND ELEVATED TEMPERATURES ANALYZED WITH WEDGE SPLITTING TESTS AND IMAGE CORRELATION

Rafael Vargas Maginador

Thesis presented to the Graduate Program in Materials Science and Engineering as a partial requirement to obtaining the title of DOCTOR IN MATERIALS SCIENCE AND ENGINEERING

Director in Brazil: Dr. Rodrigo Bresciani Canto
Director in France (joint international supervision): Dr. François Hild
Financing agency: Fapesp - Processes: #2018/23081-0 and #2021/09238-6

São Carlos-SP
2024

CANDIDATE’S VITAE

Master degree in Materials Science and Engineering by UFSCar (2019),

Bachelor degree in Materials Engineering by UFSCar (2016).

UNIVERSIDADE FEDERAL DE SÃO CARLOS

Centro de Ciências Exatas e de Tecnologia
Programa de Pós-Graduação em Ciência e Engenharia de Materiais

Folha de Aprovação

Defesa de Tese de Doutorado do candidato Rafael Vargas Maginador, realizada em 20/02/2024.

Comissão Julgadora:

Prof. Dr. Sergio Persival Baroncini Proença (USP)

Prof. Dr. Rodrigo Bresciani Canto (UFSCar)

Prof. Dr. François Hild (CNRS)

Prof. Dr. Marco Aurelio Liutheviciene Cordeiro (UFSCar)

Prof. Dr. Sebastião Ribeiro (USP)

Prof. Dr. Rafael Estevez (UGA)

Prof. Dr. Farid Benboudjema (UPSaclay)

O Relatório de Defesa assinado pelos membros da Comissão Julgadora encontra-se arquivado junto ao Programa de Pós-Graduação em Ciência e Engenharia de Materiais.

ACKNOWLEDGMENTS

I am thankful for the privilege of working with Rodrigo and François, both of whom I strongly admire professionally and personally. I owe them a huge part of my formation, and I will always try to honor their efforts in this matter. Anchieta, whose advice was crucial for defining the composition of the material used herein, also has my thankfulness. I would like to thank the members of both research groups that helped me enormously, the Eikologie team from LMPS/UPSaclay and the MECM from DEMa/UFSCar, for every meeting and conversation, that ranged from deep technical matters to random interesting topics.

I also had the pleasure to work with competent and kind professors, engineers, and technicians, to whom I express here my gratitude, for helping with the theoretical background, the experimental setups, and the numerical tools that were used. Surely, this gratitude is extended to the administrative staff from both universities that allowed this thesis in joint international supervision to be successful.

I had the privilege of being born into a family that encouraged me to study in a country where higher education is not always valued. A huge thanks to my mother and sister for always giving me the strength to look for the best formation, even at the expense of long distances during some difficult times. Another huge thanks to my spouse, Dani, for always supporting my career choice and keeping my sanity, staying by my side with love and care. I am also thankful to our beloved dog, Lord, for staying around when I worked from home and for remembering the importance of taking a walk and playing around now and then. Last but not least, to all family members and friends who directly or indirectly helped me to remain on the right path, with a word of wisdom or an incentive when I needed the most.

I am grateful to IBAR (Indústrias Brasileiras de Artigos Refratários, Poá-Brazil) for formulating and providing the studied material. All this work was allowed by the financial aid from grant #2018/23081-0, São Paulo Research Foundation (FAPESP)[1], along with grants #2018/15266-0, #2020/08077-6 and #2021/09238-6. This study was financed in part by the Coordenação de Aperfeiçoamento de

---

[1] As opiniões, hipóteses e conclusões ou recomendações expressas neste material são de responsabilidade do autor e não necessariamente refletem a visão da FAPESP.

Pessoal de Nível Superior - Brasil (CAPES) - Finance Code 001. This study was also supported in part by the French “Agence Nationale de la Recherche” through the “Investissements d’avenir” program (ANR-10-EQPX-37MATMECA Grant). Last, my honest appreciation to both institutions, Universidade Federal de São Carlos (UFSCar) and Université Paris-Saclay (UPSaclay), for providing the necessary infrastructure for this project.

ABSTRACT

Industrial high-temperature processes relies on castable refractories, whose formulation and characterization become crucial for minimizing energy loss and costs. Increasing the failure predictability is key to reducing risks in such applications. Few high-temperature mechanical tests were analyzed with full-field measurement techniques that allow for the evaluation of fracture mechanisms directly for in-service temperature ranges. With complex microstructures, crack propagation is not always known through the depth of the specimen. This thesis aims to fill in this gap with the analysis of full-field measurements of Wedge Splitting Tests (WSTs) under two experimental configurations, namely, high-temperatures assisted by Digital Image Correlation (DIC), and room-temperature WSTs performed within a tomograph with Digital Volume Correlation (DVC). Experimental forces and full-field displacements provide trustworthy boundary conditions and robust data to validate simulations of crack propagation with Finite Element (FE) codes. Two furnaces suited for DIC were used for the thermomechanical experiments, one reaching up to 600 ℃ and another, built during this thesis, up to 900 ℃, with the former allowing for the visualization from one side and the latter from opposite sides of the sample. An alumina-based castable refractory with mullite-zirconia aggregates was used for the studies, providing technologically relevant toughening at higher temperatures and good contrast for X-ray imaging. Cohesive zone models were chosen to describe crack propagation, whose parameters were calibrated using the FE Model Updating (FEMU) technique. Several methodological developments were needed from exploiting a limited field-of-view, design and fabricating one furnace, to using additive manufacturing to produce molds for notched cylindrical specimens. Fracture parameters were obtained in different configurations, and are discussed considering changes arising from the specimen geometry, crack path definition, sintering and testing temperatures. Insight is given into fracture processes in this stable crack propagation test within the bulk of the specimen and in environments closer to the final application temperatures.

Keywords: in-situ experiments ; digital image (and volume) correlation ; high-temperatures ; tomography ; finite element model updating ; crack propagation ; damage.

RESUMO

FRATURA DE REFRATÁRIOS EM TEMPERATURAS AMBIENTE E ELEVADA ANALISADA COM O MÉTODO DA CUNHA E CORRELAÇÃO DE IMAGENS

Concretos refratários são essenciais para processos que envolvem altas temperaturas em indústrias de base, sendo sua formulação e caracterização cruciais para a otimização energética e redução de custos. A previsibilidade de falhas é indispensável para reduzir riscos nestas aplicações. Poucos ensaios termomecânicos são analisados com medidas de campo, que permitem a aferição de mecanismos de fratura na temperatura de serviço. Com microestruturas complexas, a propagação de trincas em refratários não é sempre conhecida no interior da amostra, mesmo em temperatura ambiente. Esta tese preenche esta lacuna com análises de ensaios em altas temperaturas pelo Método da Cunha (MC) com Correlação de Imagens Digitais (CID), e ensaios pelo MC em temperatura ambiente assistidos por tomografia e Correlação de Volumes Digitais (CVD). Com forças e campos de deslocamentos experimentais, é possível guiar e validar simulações de propagação de trincas usando códigos de Elementos Finitos (EF). Dois fornos foram usados para ensaios termomecânicos, um para até 600 ℃, permitindo a visualização de um lado da amostra, e outro, construído durante este doutorado, para até 900 ℃, possibilitando visualizar dois lados opostos da amostra. Foi utilizado um concreto refratário aluminoso com agregados de mulita-zircônia com mecanismos de tenacificação tecnologicamente relevantes em altas temperaturas e contraste adequado para tomografia de raios-X. A propagação de trincas foi descrita por modelos coesivos, cujos parâmetros foram calibrados utilizando uma técnica de atualização de EF (FEMU). Desenvolvimentos metodológicos foram necessários, como explorar um campo de visão limitado, projetar e construir um forno e produzir moldes por manufatura aditiva para a produção de amostras cilíndricas com entalhes. Parâmetros de fratura foram obtidos em diferentes configurações e discutidos considerando a geometria da amostra, o caminho da trinca e as temperaturas de sinterização e dos ensaios. Processos de fratura foram melhor compreendidos no interior da amostra e em ambientes semelhantes ao da aplicação final.

Palavras-chave: experimentos in-situ ; correlação de imagens (e volumes) digitais ; altas temperaturas ; tomografia ; atualização de modelo de elementos finitos ; propagação de trincas ; dano.

RÉSUMÉ

FISSURATION DE RÉFRACTAIRES À TEMPÉRATURES AMBIANTE ET ÉLEVÉES ANALYSÉE AVEC DES ESSAIS DE FENDAGE ET PAR CORRÉLATION DIMAGES

Les réfractaires sont essentiels pour de nombreuses industries de base. Leur formulation et leur caractérisation deviennent cruciales pour l'optimisation énergétique. Améliorer la prévision de défaillance est primordial pour réduire les risques à hautes températures. Peu d'essais mécaniques à haute température ont été analysés avec des techniques de mesure de champ, bien que ces matériaux soient très étudiés. L'approche proposée permettra d'évaluer les mécanismes de rupture pour une gamme de températures aussi élevée que possible. Avec des microstructures complexes, même à température ambiante, la propagation des fissures n'est pas connue dans le volume des échantillons. Cette thèse comble cette lacune avec l'analyse d'essais de fendage à hautes températures avec suivi par corrélation d'images et des essais à température ambiante effectués dans un tomographe et analysés par corrélation d'images volumiques. Avec ces résultats, il devient possible de guider et de valider des simulations de propagation de fissure avec des codes d'éléments finis. Deux fours ont été utilisés (permettant chauffer jusqu'à 600 ℃ et 900 ℃, respectivement). Le second, construit pendant cette thèse, permet la visualisation de deux surfaces opposées de l'échantillon. Un réfractaire alumineux avec des agrégats de mullite-zircone est sélectionné avec une augmentation anticipée de la ténacité avec la température et un bon contraste pour les images obtenues par tomographie aux rayons-X. Des éléments cohésifs sont utilisés pour décrire la fissuration dont les paramètres sont identifiés par recalage de modèles éléments finis (FEMU). Divers développements méthodologiques ont été nécessaires (conception d'un nouveau four, production d'échantillons cylindriques, champ de vision limité pour les essais en four). Les paramètres de fissuration sont obtenus pour différentes configurations et sont discutés en considérant la géométrie des échantillons, le chemin de fissuration, la température de frittage et celle des essais. La fissuration était mieux comprise dans l'intérieur de l'échantillon et dans les environnements similaires aux de service.

Mots clés : essais in-situ ; corrélation d'image (et volume) numérique ; hautes températures ; tomographie ; recalage de modèles éléments finis ; propagation de fissure ; endommagement.

PUBLICATIONS

PEER-REVIEWED PAPERS

JAILIN, C.; BOUTERF, A.; VARGAS, R.; HILD, F.; ROUX, S. Sub-minute in-situ fracture test in a laboratory CT scanner. In: Integrating Materials and Manufacturing Innovation 2019; 8(3):413–422.
DOI: `https://doi.org/10.1007/s40192-019-00151-6`

VARGAS, R.; TSITOVA, A.; BERNACHY-BARBE, F.; BARY, B.; CANTO R. B.; HILD, F. On the identification of cohesive zone model for curved crack in mortar. In: Strain, 2020; 56(6):e12364. DOI: `https://doi.org/10.1111/str.12364`

VARGAS, R.; PINELLI, X.; SMANIOTTO, B.; HILD, F.; CANTO, R. B. On the effect of sintering temperature on the fracture energy of Alumina-Mullite-Zirconia castable at 600 ℃. In: Journal of the European Ceramic Society, 2021; 41(7):4406–4418. DOI: `https://doi.org/10.1016/j.jeurceramsoc.2021.01.023`

VARGAS, R.; CANTO, R. B.; HILD, F. Fracture energy evaluation of refractories in wedge splitting tests from notch opening displacements. In: Journal of the European Ceramic Society, 2021; 41(10):5367–5379.
DOI: `https://doi.org/10.1016/j.jeurceramsoc.2021.02.055`

SCIUTI, V. F.; VARGAS, R.; CANTO, R.B.; HILD, F. Pyramidal adaptive meshing for Digital Image Correlation dealing with cracks. In: Engineering Fracture Mechanics, 2021; 256:107931.
DOI: `https://doi.org/10.1016/j.engfracmech.2021.107931`

VARGAS, R.; CANTO, R. B.; HILD, F. On the Calibration of Cohesive Parameters for Refractories from Notch Opening Displacements in Wedge Splitting Tests. In:

Journal of the European Ceramic Society, 2021; 41(14):7348–7361.
DOI: `https://doi.org/10.1016/j.jeurceramsoc.2021.07.011`

VARGAS, R.; CANTO, R. B.; HILD, F.; ROUX, S. On accounting for speckle extinction via DIC and PCA. In: Optics and Lasers in Engineering, 2022; 149:106813.
DOI: `https://doi.org/10.1016/j.optlaseng.2021.106813`

FABRIS, D. C. N.; MIGUEL, E. H.; VARGAS, R.; CANTO, R. B.; VILLAS-BOAS, M. O. C.; PEITL, O.; SGLAVO, V. M.; ZANOTTO, E. D. Microstructure, residual stresses, and mechanical performance of surface crystallized translucent glass-ceramics. In: Journal of the European Ceramic Society, 2022; 42(11), 4631–4642. DOI: `https://doi.org/10.1016/j.jeurceramsoc.2022.04.024`

SONEGO, M.; SCIUTI, V. F.; VARGAS, R.; CANTO, R. B.; PESSAN, L. A. Composite design bioinspired by the mesocarp of Brazil nut (Bertholletia excelsa). In: Bioinspiration & Biomimetics, 2022; 17(4):046011.
DOI: `https://doi.org/10.1088/1748-3190/ac6f37`

VARGAS, R.; CANTO, R. B.; HILD, F. Cohesive properties of refractory castable at 600 °C: Effect of sintering and testing temperature. In: Journal of the European Ceramic Society, 2022; 42(14):6733–6749.
DOI: `https://doi.org/10.1016/j.jeurceramsoc.2022.06.070`

VARGAS, R.; CANTO, R. B.; SMANIOTTO, B.; HILD, F. Calibration of cohesive parameters for a castable refractory using 4D tomographic data and realistic crack path from in-situ wedge splitting test. In: Journal of the European Ceramic Society, 2023; 43(2):676–691.
DOI: `https://doi.org/10.1016/j.jeurceramsoc.2022.09.040`

SCIUTI, V. F.; VARGAS, R.; CANTO, R. B.; HILD, F. Modal characterization of crack network development in an MgO containing refractory castable. In: Journal of Strain Analysis for Engineering Design, 2023; 58(6):490–500.
DOI: `https://doi.org/10.1177/03093247221141490`

SCIUTI, V. F.; VARGAS, R.; GUERRERO, N.; MARANTE, M. E.; HILD F. Digital image correlation analyses of masonry infilled frame: Uncertainty-based mesh refinement and damage quantification. In: Mathematics and Mechanics of Solids. 2023;0(0). DOI: `https://doi.org/10.1177/10812865231174840`

ZAGO, I. P.; VARGAS, R.; SCIUTI, V. F.; CANTO, B. C.; ANGÉLICO, R. A. DIC to evaluate a model composite system cracking due to CTE mismatch. In: Theoretical and Applied Fracture Mechanics. 2024.
DOI: `https://doi.org/10.1016/j.tafmec.2024.104330`

VARGAS, R.; ZAGO, I. P.; SCIUTI, V. F.; FURLAN, M.; ANGÉLICO, R. A.; HILD, F.; CANTO, R. B. Multi-window setup for thermomechanical experiments assisted by DIC up to 900℃. Submitted for publication.

BOOK CHAPTERS

LUCAS, A. A.; OLIVEIRA, B. S.; SCURACCHIO, C. H.; AFONSO, C. R. M.; LEIVA, D. R.; FIGUEIRA, G.; GALETTI, H. V. A.; MARCOS, L. P.; COSTA, L. C.; PAULILLO, L. F. O.; CORDEIRO, M. A. L.; PEZZO, M. R.; MAGINADOR, R. V.; SERRA, S. M. B. Capítulo 5: Movimenta Materiais: transformação da Educação em Engenharia no Centro de Ciências Exatas e de Tecnologia da UFSCar. In: Planejamento e Primeiros Resultados dos Projetos Institucionais de Modernização da Graduação em Engenharia (2019-2020) - Programa Brasil-Estados Unidos de Modernização da Graduação em Engenharia (PMG), 2021; 97–120.
ISBN: 978-65-87897-01-1

CONFERENCE PROCEEDINGS

VARGAS, R.; HILD, F.; CANTO, R. B. Defining specimen size for the wedge splitting test to analyze the fracture process zone. In: 5th Brazilian Conference on Composite Materials (BCCM 5). São Carlos (online), Brazil; 21-24 July 2021, p.12.

VARGAS, R.; CANTO, R. B.; HILD, F. Fracture properties of a refractory castable extracted from 600℃ wedge splitting tests. In: 18th European Mechanics of Materials Conference (EMMC 18). Oxford, England; 4-6 April 2022.

VARGAS, R.; SMANIOTTO, B.; CANTO, R. B.; HILD, F. In-situ monitoring of castable refractory fracture. In: 5th International Conference on Tomography of Materials & Structures (ICTMS 2022). Grenoble, France; 27 June - 1 July 2022.

VARGAS, R.; CANTO, R. B.; HILD, F. Effect of Sintering Temperature on Fracture parameters for an alumina-mullite-zirconia refractory via Wedge Splitting Tests at 600℃. In: 9th International Congress on Ceramics (ICC 9). Krakow, Poland; 10-14 July 2022.

VARGAS, R.; CANTO, R. B.; HILD. F. De l'analyse d'essais de fissuration par enfoncement d'un coin pour l'obtention de paramètres cohésifs à hautes températures. In: Congrès Français de Mécanique 2022 (CFM 2022). Nantes, France; 29 August - 2 September 2022.

CONTENTS

LIST OF TABLES

LIST OF FIGURES

LIST OF ABREVIATIONS

BCc Boundary Condition correction

CDP Concrete Damaged Plasticity

CMOD Crack Mouth Opening Displacement

COD Crack Opening Displacement

CZM Cohesive Zone Model

DIC Digital Image Correlation

DVC Digital Volume Correlation

F600 furnace for thermomechanical experiments from LMPS, capable of reaching up to 600℃

F900 furnace for thermomechanical experiments built in Brazil during this thesis, capable of reaching up to 900℃

FE Finite Element

FEM Finite Element Method

FEMU Finite Element Method Updating

FEMU-COD FEMU with COD in the cost function

FEMU-F FEMU with forces in the cost function

FEMU-F-NOD FEMU with forces and NODs in the cost function

FEMU-U FEMU with displacements in the cost function

FEMU-UF FEMU with displacements and forces in the cost function

FOV Field Of View

FPZ	Fracture Process Zone
G-FEM	Generalized Finite Element Method
IPCC	Intergovernmental Panel on Climate Change
LMPS	Laboratoire de Mécanique Paris-Saclay (Paris-Saclay University)
NOD	Notch Opening Displacement
PCA	Principal Component Analyses
P-DVC	projection based DVC
PPR	cohesive traction-separation law named after the three authors, Park, Paulino, and Roesler
ROI	Region Of Interest
SEM	Scanning Electron Microscopy
SNR	Signal to Noise Ratios
UEL	User ELement
WST	Wedge Splitting Test
X-FEM	eXtended Finite Element Method

LIST OF SYMBOLS

BCc - Boundary Condition correction

c - Affine-fit slope of the NOD vs. CMOD curve in the post-peak regime

E - Young's modulus

f - Gray level image of the reference state

$\{\mathbf{F}\}$ - Column vector gathering the external nodal forces

F_h - Horizontal splitting force in a WST

F_v - Vertical force in a WST

g - Gray level image of the deformed state

$\tilde{g}$ - Gray level image of the deformed state corrected (deformed back) by the measured displacement field

$\{\mathbf{h}\}$ - Right-hand member for FEMU linear systems

$[\mathbf{H}]$ - Hessian matrix for FEMU linear systems

J_c - Fracture energy for the PPR law

$[\mathbf{K}]$ - Stiffness matrix

ℓ_H - Hillerborg length

$[\mathbf{L}]$ - Auxiliary matrix to enforce constraints by Lagrange multipliers

n - Related to the n-th iteration

N - Number of time steps for experimental measurements

$\{\mathbf{p}\}$ - Vector gathering the parameters of interest

$\{\tilde{\mathbf{p}}\}$ - Vector gathering the actualized guess of the parameters of interest

R - Ratio of CMOD and NOD at the ultimate load

$[\mathbf{S}]$ - Sensitivity matrix

t - Time steps for experimental measurements

$\mathbf{u}$ - Displacement vector

U - Internal energy of medium

W - Work done by outer forces

$\mathbf{x}$ - Position vector

α - Shape parameter for the PPR law

β - Wedge angle between the lateral face and the symmetry axis

γ - Experimental standard uncertainty

$\overline{\delta}$ - NOD normalized by the NOD at the ultimate load

$\overline{\Delta}$ - CMOD normalized by the CMOD at the ultimate load

$\{\delta \mathbf{p}\}$ - Parameter corrections wrt. their current estimates

$\{\delta \boldsymbol{\upsilon}\}$ - Correction of $\{\boldsymbol{\upsilon}\}$

ϵ_1 - maximum principal strain

$\{\lambda\}$ - Column vector that gathers the so-called Lagrange multipliers

π - Potential energy

σ_I - Mode I tractions

σ_f - Cohesive strength for the PPR law

υ_i - Amplitudes (or degrees of freedom) of $\boldsymbol{\Psi}_i$

ϕ - Global gray level residual

χ^2 - Sum of normalized squared differences

$\boldsymbol{\Psi}$ - Basis of displacement fields

1 INTRODUCTION

Castable refractories are materials of choice for high-temperature and corrosive environments, and thus are key for various transformation industries. In aggressive environments, the understanding of fracture processes is crucial since cracks are unavoidable. One test that allows for the estimation of the work of fracture is the so-called Wedge Splitting Test (WST). By using a wedge and cylinders to apply a mode I loading, it decreases the elastic energy stored in the testing machine and enables for stable crack propagation in quasi-brittle materials. However, the test is quite laborious, which leads to the search for a better understanding of the material behavior from one single test to exploit its richness of information.

One recent approach is using full-field measurement techniques such as Digital Image Correlation (DIC) instead of point data, primarily to assess crack propagation. Quite often, this test is also simulated using the Finite Element Method (FEM) to calibrate constitutive models that may allow not only the comparison among various materials but also to simulate parts with different geometries or even in-service conditions.

This thesis aims to look further, performing high temperature WSTs to assess fracture parameters closer to in-service conditions. Moreover, in-situ tests inside a tomograph were conducted to obtain bulk measurements. Both experimental configurations were analyzed via full-field measurements and coupled to parameter identification and numerical simulations. This work bring insights into new experimental setups and characterization methodologies, with innovative experiments and state-of-the-art numerical approaches to better understand fracture mechanisms and the development of fracture process zones in castable refractories.

2 BIBLIOGRAPHIC REVIEW

This section summarizes the theoretical background of this thesis, focusing on points to guide the understanding of the choices made herein, from the material and methods up to the analysis of the results. A brief conclusion highlighting what was found in the literature is given at the end of this section.

2.1 Castable refractories

Castable refractories consist of monolithic refractories that need no preforming (*e.g.,* into bricks) [1]. They are endowed with better resistance to corrosion due to the absence of solder lines, and they are often cheaper and faster to be implemented. They are mainly composed of coarse microstructures with aggregates (between 40 and 80 wt% and with dimensions ranging on average from 100 µm to 20 mm bound by fine powders and binders that define the matrix [1, 2]. The different particle sizes, components, composition and processing routes dictate the final phases and therefore the properties of these materials, and each of these points may lead to interesting study lines [2]. Depending on the application requisites, all these factors can be engineered to improve the quality of the final product [3]. For example, zirconia particles can be finely dispersed into an alumina matrix for producing refractory valves for casting processes where other materials would rapidly fail under the inherent combined thermal shocks and erosion [4]. Even though empirical rules help selecting and developing good materials for a given application, the complexity of the involved mechanisms and their interactions drives the need for always critically analyzing each given case.

It is hard to imagine nowadays technologies without refractories. They are used for every high-temperature industrial transformation process and allowed many industries to develop [2]. They are vital for processing steel, oil, glass, cement, and many other products [5]. They are utilized in furnaces, cauldrons and other high-temperature applications, often within corrosive environments. Thus, their main characteristics is their ability to sustain properties in acceptable levels even in aggressive conditions. However, damage is inevitable in such conditions [3], and their maintenance and substitution must be considered. In hazardous processes, the involved risks lead to the constant search for improvement of various properties, and for the understanding of damage mechanisms in these materials to avoid accidents, predict their lifetime, reduce costs and improve their performance. Moreover, climate change due to greenhouse gases is already in dangerous levels, with several consequences if fast and coordinated international action is not made as clearly stated in the latest Intergovernmental Panel on Climate Change (IPCC) report [6]. Among their suggestions of possible actions, increasing material and energetic efficiency are cited, which shed light on the importance of studying and improving refractories since they are needed in various industrial branches. Although not within the scope of this work, some trends are observed for the development of new refractories [2]. One of these trends consists in using raw material nanoparticles [7, 8] (*e.g.,* for reducing the sintering temperature and therefore improving the densification while reducing coarse graining). However, the nanoscale route presents numerous challenges such as how to properly disperse the components, and the cost-benefit trade-off since they are usually expensive. Another approach is trying to mimic natural microstructures as those found, for instance, in nacre [9, 10]. It is possible to increase the toughness while maintaining high strength, which is impossible in usual materials. This route still needs to deal with up-scaling models since most cases are lab-designed materials. Substituting the usual calcium aluminate cement is also a current trend in order to improve final properties and avoid challenges on the initial heating protocols [11], which, if not mastered, may cause porosity that is deleterious to the strength. For instance, geopolymers (*i.e.,* polymerized inorganic nanoparticles) may be used as a substitute with benefits for high-temperature applications [12].

For the present work, the composition of interest consists of alumina, mullite, and zirconia. The so-called high-alumina composition (*i.e.,* high-alumina aggregates in a low iron refractory cement with alumina content above 60 wt% [13]) exhibits interesting thermal, mechanical and electrical properties, which are often maintained at satisfactory levels above 1600 °C. These compositions become appealing for many engineering applications when combining the necessary properties with high availability and low price [14]. The addition of mullite-zirconia aggregates has been shown to improve the work of fracture and thermal shock resistance [15], and also to promote toughening by the interaction between a propagating crack and the material microstructure when coarse aggregates are used [16]. The presence of zirconia is specifically used when chemical inertness and low thermal conductivity are of interest. However, one critical point is the tetragonal to monoclinic (martensitic) phase transformation [17], which will be discussed in Section 2.3. Last, the composition with zirconia is chosen herein as a model material in order to develop methodologies using tomographic data since it improves the contrast between phases, given their difference in atomic weight and number.

2.2 Imaging of refractories

Different material imaging techniques are available, ranging from several orders of magnitude in magnification. The meaning of the obtained 2D image and its pixels (*i.e.,* , the smallest subdivision of it) depends on which interaction with the matter the sensor detects. Usually, these sensors are made with semiconductors or scintillators (and their variations/combinations). For instance, visible light is detected by usual digital photographic cameras and the resulting electrical signal encodes the luminosity (or color) of the object of interest at a given time. One pixel in such images may encode information from few micrometers, as will be exemplified throughout this work, up to above meters [18], depending on the employed optical system. For refractories, this device allows surface visualization ranging from localized deformations, crack propagation and post-mortem fracture topography (with a confocal microscope) up to macro deformations in full structures (*e.g.,* outside industrial furnaces to check for possible damage). For smaller scales from mm down to nm, Scanning Electron Microscopy (SEM) is used to gather the interaction of an electron beam with the sample surface and give topographic [19] or chemical composition information [20]. The smaller fields-of-view are used to investigate the presence and conformation of phases in the microstruture or fracture surface, but care should be taken to ensure the images are representative in heterogeneous materials. One considerable difference between both previous examples is that the image is directly gathered by photographic cameras. However, as the name suggests, in SEMs the image is built one line at a time by scanning several points, which calls for corrections when full-field measurements are used [21]. Another example of obtaining indirect images is the so-called X-ray computed tomography, in which each radiograph gathers the matter X-ray attenuation. Such images are gathered at numerous angles, and then a 3D image is built after numerical integration based on the (inverse) Radon transform [22]. Bulk information is obtained with the limitation coming from the sample size (from nm to few cm) and the power source. Generally, the higher the density and thickness of the sample, the more powerful source is needed. Laboratory scanners are commercially available, but depending on the sought resolution or the investigated material, one may go to synchrotron facilities for higher quality/intensity X-ray sources [23, 24].

2.3 Mechanical properties of refractory ceramics

Ceramics are known to present strong ionic-covalent atomic bonds. The directionality of the covalent bonds leads to low packing crystals with high activation energy for dislocation motions and few sliding planes, which result in the brittleness of these materials, especially at room-temperature with a quasi-absence of plasticity. These features lead to interesting properties such as high abrasiveness, hardness, refractoriness, stiffness, thermal and electrical resistance, and thermal and chemical stability [25, 26]. For castable refractories (the scope of this work), the processing route leads to inherent porosity and the presence of aggregates in the final microstructure.

Since crack initiation is inevitable in extreme service conditions [3], these materials are usually engineered to exhibit toughening mechanisms that make it difficult for cracks to propagate. Although different mechanisms exist [27], there are two major ones for castable refractories [28]. The first one dissipates energy by deflecting the crack and therefore creating more surfaces where the bond energy of bulk atoms is converted into surface energy through atoms with fewer neighbors (*i.e.,* in a higher energy state) [26]. It may be induced by material heterogeneity, like a strong aggregate that is difficult for the crack to traverse and causes the crack to go around it, therefore initiating few intragranular damage and inducing a majority of intergranular cracks. The second one occurs when some phenomena alleviate the tensile stresses in the vicinity of the crack tip. This property can be caused by microcracks around the crack tip, phase changes (*e.g.,* zirconia that expands and compresses its surroundings), aggregate bridging, ramifications, and glassy phases [4, 27–29].

In the context of this work, phase changes that can induce crack tip shielding are of special interest since the studied composition contains mullite-zirconia aggregates. Zirconia exhibits a martensitic phase change (from tetragonal to monoclinic lattices), which occurs very quickly, leading to a 4% volume expansion with a 16% shear strain, and takes place around 950 ℃ upon cooling down (reversible on heating up around 1150 ℃) [30]. This transformation has been the subject of many studies in the 1970s, and from 1975 onward [31], it was understood and developed to be beneficially used in refractories. For this effect to take place, it is important that this transformation is confined in the matrix, and that it activates the phase change at stresses less than the matrix strength. When it occurs, it may induce compressive states and add shear strain energy at the crack tip, which needs to be surpassed for the crack to continue to propagate. Therefore, it hinders crack propagation and increases the material toughness and strength [30].

Some toughening mechanisms were already studied at high-temperatures, for a mullite composite reinforced with carbon-fibers, whose strength increases from 25 to 1200 ℃ thanks to the interface properties [32]. The toughness also presents a six-fold increase at room-temperature, compared to the raw materials alone. Further, the authors used DIC analyses to highlight crack bifurcations. Another interesting example concerns bio-inspired microstructures in which stable crack propagation and crack deflection, branching, and bridging mechanisms were observed up to 1200 ℃, along with high strength and toughness [33]. However, especially when discussing ceramics, it can be stated that "*toughening mechanisms that remain effective at high temperatures are still not totally understood.*" [34].

2.4 Wedge Splitting Test (WST)

When discussing castable refractories one has to deal with brittle materials, in which crack propagation is very important. However, in many experimental setups cracks propagate catastrophically, which makes the visualization and analysis of toughening mechanisms difficult. The Wedge Splitting Test (WST) is one setup that converts an applied vertical compressive force (which is easier to perform) on a wedge into amplified horizontal opening forces (mode I), transmitted to the specimen through two cylinders, to achieve stable crack propagation even in quasi-brittle materials. This stability is promoted by decreasing the elastic energy stored in the testing machine [35, 36]. Therefore, when cracks propagate incrementally, there is no sudden release of elastic energy that would lead to catastrophic propagation and failure. The horizontal force F_h intensifies the applied vertical force F_v, depending on the wedge angle β between the wedge surface and the symmetry axis

$$F_h = \frac{F_v}{2\tan\beta} \tag{2.1}$$

where $\beta \approx 5°$ in this work (*i.e.,* $F_h \approx 5.715F_v$), as illustrated in Figure 2.1(a) together with its dimensions and other parts used in the setup. The chosen angle was empirically optimized since a smaller β may lead to experimental difficulties,

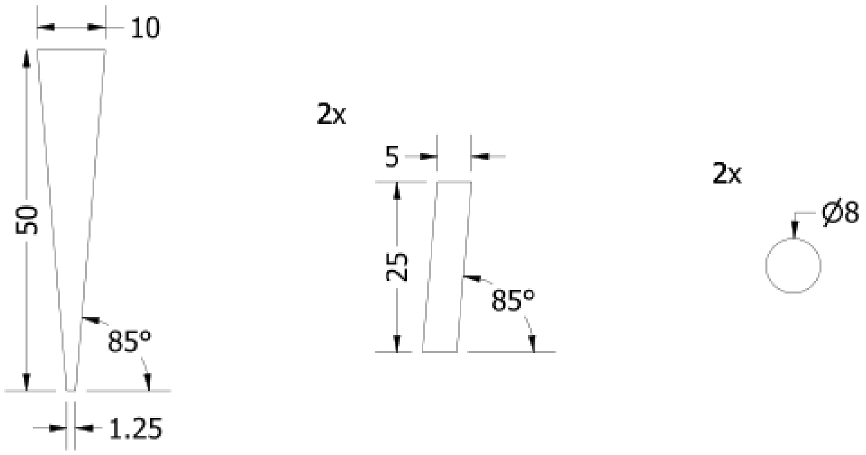

(a) (b) (c)

Figure 2.1: Frontal view of the parts used for the WST setup. (a) One wedge, (b) two blocks, and (c) two cylinders. Their out-of-plane length is 75 mm. Dimensions are in mm.

while higher angles intensify less the applied load and could promote instabilities in the propagation stage (caused by the higher stored elastic energy in the testing machine) [36]. Another advantage of the technique is the possibility to test samples extracted from real structures, after just sawing a pre-notch. In the present work, a parallelepipedic geometry [37] is considered for the high-temperature tests, as shown in Figure 2.2(a-c), for monitoring crack propagation on flat surfaces. For the tests performed inside an X-ray tomograph, a cylindrical geometry (Figure 2.2(d-f)) is preferred to improve the image quality [38] to study crack propagation in the bulk.

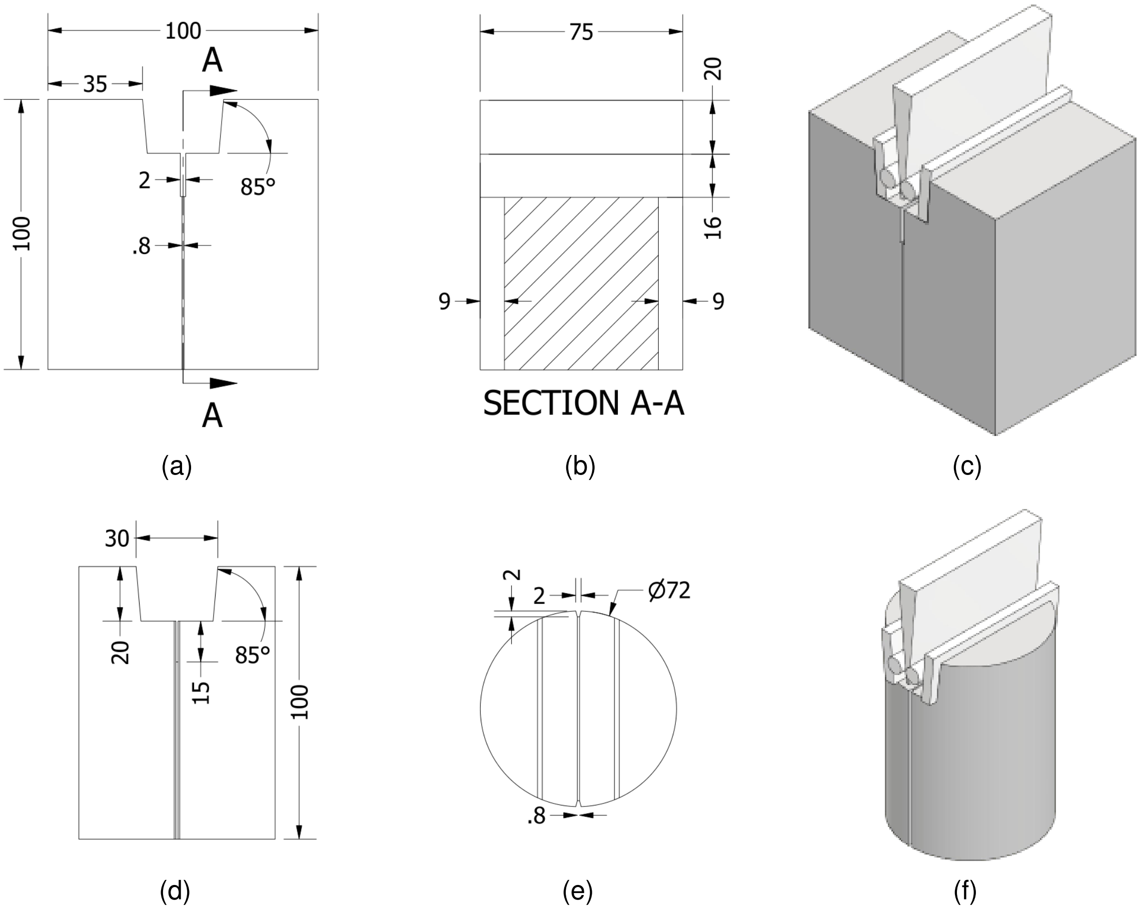

(a) (b) (c)

(d) (e) (f)

Figure 2.2: Prismatic and cylindrical samples used in this project, in the first and second rows, respectively (dimension are expressed in mm). (a,d) Frontal views. (b) Lateral A-A section of prismatic sample (a). (c,f) Isometric views with the other parts of the WST setup (see Figure 2.1). (e) Top view of cylindrical sample.

WSTs are mainly used for obtaining the work of fracture since high fractured area to volume ratios [29, 39] allow for representative mechanisms to occur with considerably smaller specimens even with complex microstructures. Since stable crack propagation is usually reached in WSTs, one may integrate the load-crack opening displacement curve to estimate the energy used to propagate the crack, and then divide it by the projected cracked area to evaluate the fracture energy. To evaluate the crack opening displacement, extensometers are commonly used. However, with full-field measurement techniques, it is possible to obtain more data from a single test.

Since refractories are utilized in high-temperature environments, it is of interest to obtain properties at application temperatures. Some work can be found on the utilization of WSTs at high temperatures. For instance, results for magnesia-chromite bricks may be affected by the viscosity and therefore by the loading velocity on tests performed at 1000 °C [40]. In Ref. [41], the authors used WSTs at temperature levels equal to 1000, 1250 and 1500 °C for magnesia-based compositions as a tool for material selection and product development. More recently, WSTs were performed at 1400 °C for a MgO-C refractory with argon atmosphere to prevent carbon to be oxidized [42]. None of the cited papers (in this section) used or reported full-field measurements. Such studies will be presented in the following Sections.

2.5 Digital Image Correlation (DIC)

The full-field measurement technique known as DIC [43, 44] allows displacement *fields* to be measured instead of point data (*e.g.,* taken from extensometry). Therefore, information about localized phenomena can be assessed and was already successfully applied for crack propagation analyses [45–49]. Hereafter, a brief introduction on DIC principles is given, followed by a discussion about its application in images acquired in high-temperature experiments, and also when volumes (*i.e.,* 3D images) were used instead of usual 2D images.

2.5.1 DIC principle

First, let us consider the optical flow, namely, the gray level conservation

$$f(\mathbf{x}) = g(\mathbf{x} + \mathbf{u}(\mathbf{x})) \tag{2.2}$$

where f is the gray level of the reference image, g that of the deformed state, $\mathbf{x}$ the position vector, and $\mathbf{u}$ the displacement vector. The global gray level residual, ϕ^2, is defined as

$$\phi^2 = \sum_{\text{ROI}} [f(\mathbf{x}) - g(\mathbf{x} + \mathbf{u}(\mathbf{x}))]^2 \tag{2.3}$$

and consequently, the sought displacement field $\mathbf{u}$ should minimize ϕ^2 over the whole Region Of Interest (ROI). If the displacements are sought pixel-wise, such analysis is ill-posed *per se*. One usual regularization consists in defining the displacement field in a selected kinematic basis of fields $\boldsymbol{\Psi}$, and the respective amplitudes (or degrees of freedom) gathered in the column vector $\{\boldsymbol{\upsilon}\}$ then become the unknowns to be determined

$$\mathbf{u}(\mathbf{x}) = \sum_i \upsilon_i \boldsymbol{\Psi}_i(\mathbf{x}) \tag{2.4}$$

in which $\boldsymbol{\Psi}_\mathbf{i}$ can be defined in several ways [43, 44], but for this work the main interest is using FE shape functions (*e.g.,* four-noded quadrilaterals [50] or three-noded triangles [51], the latter used herein). In order to proceed with an iterative Gauss-Newton scheme to minimize the cost function ϕ^2 [52], let us consider the result for iteration n, and the corrections $\delta\upsilon_i$ are sought such that

$$\upsilon_i^{(n+1)} = \upsilon_i^{(n)} + \delta\upsilon_i \tag{2.5}$$

A first order approximation of g leads to

$$g(\mathbf{x} + \sum_i (\upsilon_i^{(n)} + \delta\upsilon_i)\boldsymbol{\Psi}_i(\mathbf{x})) \approx \tilde{g}(\mathbf{x}) + \nabla\tilde{g}(\mathbf{x}) \cdot \sum_i \delta\upsilon_i \boldsymbol{\Psi}_i(\mathbf{x}) \tag{2.6}$$

with

$$\tilde{g}(\mathbf{x}) = g(\mathbf{x} + \sum_i \upsilon_i^{(n)} \boldsymbol{\Psi}_i(\mathbf{x})) \tag{2.7}$$

where $\tilde{g}$ is gradually backdeformed to match the reference state using the current displacement field estimate. The approximation $\nabla\tilde{g} \approx \nabla f$ leads to a reduction of processing time, since ∇f is calculated only once, and this hypothesis is truer as convergence is approached. Last, Equation (2.6) is substituted in Equation (2.3).

The global approximate residual is differentiated with respect to the displacement increments $\delta \upsilon_j$, and is equaled to zero to reach an extremum (actually a minimum), which leads to the following system of equations

$$\left[\sum_{\text{ROI}} (\boldsymbol{\Psi}_i \cdot \nabla f)(\mathbf{x})(\boldsymbol{\Psi}_j \cdot \nabla f)(\mathbf{x})\right] \delta \upsilon_j = \sum_{\text{ROI}} [f(\mathbf{x}) - \tilde{g}(\mathbf{x})](\boldsymbol{\Psi}_i \cdot \nabla f)(\mathbf{x}) \tag{2.8}$$

where the column vector $\{\boldsymbol{\delta \upsilon}\}$ gathers the displacement corrections $\delta \upsilon_j^{(n)}$ to the current nodal displacement estimate $\{\boldsymbol{\upsilon}^{(n)}\}$. The measured displacements are then obtained after $\{\boldsymbol{\delta \upsilon}\}$ reaches a user-defined convergence criterion (*i.e.,* its norm becomes less than 10^{-4} px).

An example of DIC result from previous works using WSTs [53, 54] is shown in Figure 2.3. The reported displacement field was measured with the DIC code Correli 3.0 [51], which is developed at Laboratoire de Mécanique Paris-Saclay (Paris-Saclay University) (LMPS). The rigid body motions were removed from these fields to keep only the mechanically relevant information. A clear mode I (opening) contribution in the horizontal displacements is observed, and no visible mode II (in-plane shearing) component in the vertical displacements. In the present case, the physical size of one pixel was 62 µm, meaning that the reported displacement field at the peak load had a maximum range in the order of 1 px. In other words, for most of the test (time and space-wise) the measured displacements were in the sub-pixel domain. In common setups, when using properly sized finite elements as the kinematics basis, it is usual to achieve displacement uncertainties in the order of few centipixels [55, 56].

Other examples of the use of DIC for analyzing WSTs for refractories have been reported in the last years [53, 57–64], often qualitatively evaluating the length and the fracture process zone size. It is worth remembering that for brittle and quasi-brittle materials, displacement amplitudes are generally very low, which require robust DIC codes with sub-pixel resolutions (as illustrated in Figure 2.3).

2.5.2 DIC at high-temperatures

One of the main advantages of DIC over conventional extensometry, apart from its high-resolution and full-field nature, is that no contact with the specimen is

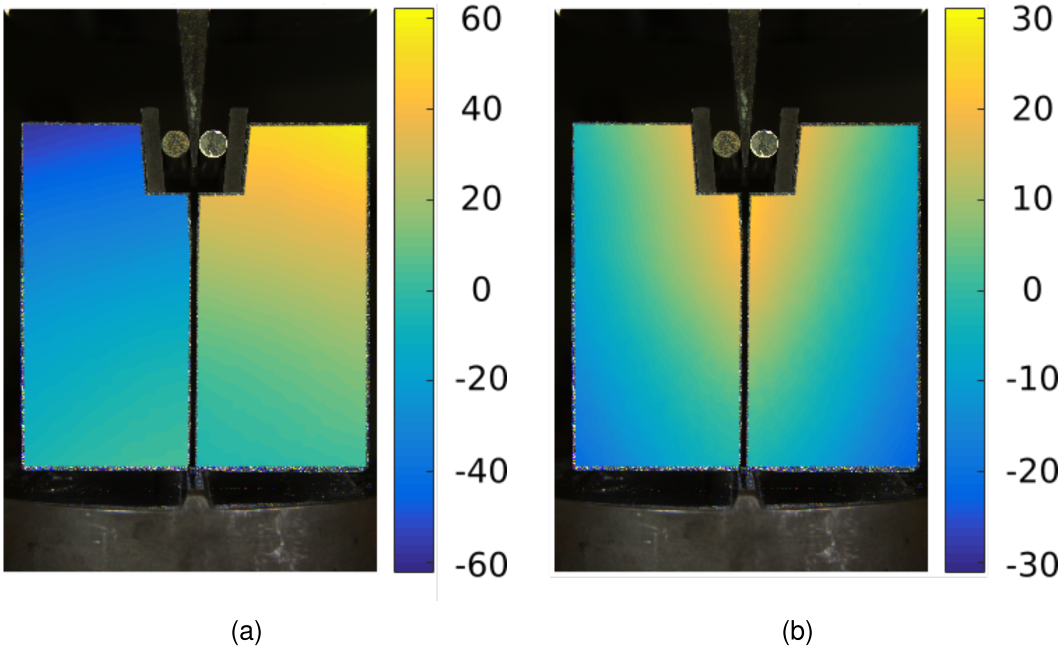

(a)

(b)

Figure 2.3: Displacement fields (expressed in µm) measured via DIC for the peak load of one WST (discussed in Refs. [53, 54]). The specimen height is ≈100 mm and one pixel represents 62 µm. (a) Horizontal and (b) vertical displacement components.

needed. This is especially true for high-temperature applications. Moreover, full-field results also provide data for the identification of material parameters and the validation of constitutive models. A further motivation can be found in Ref. [65], whose main discussion was related to challenges for assessing refractory properties at high-temperatures, namely, closer to their application conditions. The idea of further characterization of these materials is to better predict their degradation and help for the development and design of materials and products.

The main challenges of high-temperature tests are related to the heat haze and black body radiations above 800 °C [65, 66], and very small displacements due to their quasi-brittleness. If heat haze effects occur, it is possible to temporally regularize the DIC solution. Temporal continuity can be enforced, which was shown to mitigate such effects at temperatures above 1200 °C [67]. At very high-temperatures, the gray level conservation may also be relaxed since the “color” of the material changes due to black body radiations [66]. These changes can be corrected with brightness and contrast correction fields as shown for cases up to 1860 °C [68]. It is worth noting that the last two cited approaches were implemented within the same Correli 3.0 [51] framework that is used in this work.

A first paper using the WST and DIC up to 1200 °C was recently published [69], which shows that it is a current research topic. The authors identified fracture parameters for a cohesive zone model by finding the best fit between the experimental and simulated force and crack length (measured by the displacement jump evaluated from DIC) for three temperatures: 25, 800 and 1200 °C. It is worth noting that full-field data were not used in the cost function to be minimized or in the validation of the cohesive model. Further, information from both sides of the specimen could be useful to capture 3D effects [53, 70]. For the FE analysis, the crack path could be defined more precisely on the gray level residuals instead of the strain fields [71], and the cohesive zone model could be extended to have temperature-dependent parameters.

2.5.3 Extension to 3D images

Another approach for analyzing such materials with complex microstructures and quasi-brittle fracture is through 3D imaging. A review about Digital Volume Correlation (DVC) [72] discusses several examples with different materials. At the very beginning, local approaches were used to measure displacements and calculate strains in optically opaque materials. Developments of global techniques and hardware allow for more robust approaches, even integrating the measurements directly with the simulations to calibrate mechanical properties.

For example, the 3D crack profile could be detected inside a sample by combining synchrotron tomography and image analyses [73]. Displacement fields measured via DVC were post-processed to obtain stress intensity factor profiles for modes I, II and III in a nodular graphite cast iron specimen. A similar technique was also performed on another cast iron sample with in-situ tomography [74] at a smaller scale. Integrated DVC (in space and time) can also be utilized to directly measure mechanical properties [75]. Experimentally measured boundary conditions (via DVC) were prescribed to the FE model, which provided the kinematic bases to minimize the offset to the gray level conservation.

It is important to note that the three examples of mechanical parameter extraction from DVC were performed on cast iron samples, which are endowed with good microstructural contrast. References [76, 77] show that the microstructure of ceramic materials may also exhibit natural contrast sufficient for DVC purposes. As another example, a Chevron-notched graphite specimen was loaded with a wedge inside a lab tomograph and analyzed via DVC, allowing for comparisons of experimental displacements with numerical models considering prescribed crack positions, followed by the extraction of stress intensity factors [78]. Later on, the same authors performed a similar experiment but in a synchrotron facility, and showed that the experimental displacements could be made closer to the simulation if a cohesive zone model was used [79]. A similar experiment was performed on the material studied herein to measure crack propagation with projection-based DVC, showing the feasibility of using this material, which provided sufficient contrast, especially related to mullite-zirconia aggregates [38]. However, the wedge was directly pressed on the sample in the three aforementioned references, such that the force measurements were not exploitable since friction was unknown. To the best of author's knowledge, no other application of DVC to WSTs has been reported so far, apart from what is discussed in the results section.

2.6 Finite Element Method (FEM)

Many engineering problems can be formulated as partial differential equations (*e.g.,* the analysis of stresses, fluid flows, heat transfer, propagation and interference of electromagnetic waves). Among other possible methodologies, the Finite Element Method (FEM) is one numerical approach used to solve these equations [80]. One of its greatest benefits is accounting for complex geometries, which can be very costly for other methods such as the finite difference techniques. An interesting history of the method development is given in Ref. [81] by the author who first introduced the “finite element” terminology. It consists in subdividing the domain of interest into small elements connected through their nodes, in which the sought solutions are approximated at these nodal positions. Nowadays, it is used by many companies, is taught in most undergraduate engineering courses, and there are plenty of commercial softwares dedicated to such analyses.

For a detailed development of this formulation, the interested reader is referred to Refs. [80, 82, 83], and for the description hereafter, especially to Ref. [83]. Let us consider the formulation derived from the minimization of the potential energy in an FE mesh, π, under the hypothesis of a linear and isotropic elastic medium, without changes in temperature or internal body force effects. In summary, π is defined as

$$\pi = U + W \tag{2.9}$$

where U is the internal energy of the solid, and W the work done by outer forces. In an elastic body, the internal strain energy reads

$$U = \frac{1}{2}\{\boldsymbol{v}\}^{\mathsf{T}}[\mathbf{K}]\{\boldsymbol{v}\} \tag{2.10}$$

where the column vector $\{\boldsymbol{v}\}$ gathers the nodal displacements, and $[\mathbf{K}]$ denotes the stiffness matrix, which includes the elastic properties and the spatial derivatives of the FE shape functions. The external work is defined as

$$W = \{\boldsymbol{v}\}^{\mathsf{T}}\{\mathbf{F}\} \tag{2.11}$$

where $\{\mathbf{F}\}$ is the column vector gathering the external nodal forces. To minimize π, it is differentiated with respect to the displacement vector (and made equal to zero)

$$\frac{\partial \pi}{\partial \{v\}^{\mathsf{T}}} = [\mathbf{K}]\{v\} - \{\mathbf{F}\} = 0 \implies [\mathbf{K}]\{v\} = \{\mathbf{F}\} \tag{2.12}$$

Equation (2.12) highlights how the displacements can be obtained in such case. If the displacements are prescribed instead of forces, few adaptations must be performed in Equation (2.12) but the main idea remains [84]. Starting from the system shown in Equation (2.12), one may want to enforce, say, equality among certain degrees of freedom. In this case, an auxiliary matrix $[\mathbf{L}]$ is necessary, in which each column accounts for one constraint and each row is related to one degree of freedom. For instance, if the only desired constraint is that the displacements are the same for the degrees of freedom k and m (*i.e.,* $v_k - v_m = 0$), $[\mathbf{L}]$ will consist of a zero column vector, with a value of 1 in the k-th position and

-1 in the m-th position. After all the constraints are accounted for constructing $[\mathbf{L}]$, the new system to be solved becomes

$$\left[\begin{array}{c|c} [\mathbf{K}] & [\mathbf{L}] \\ \hline [\mathbf{L}]^{\mathsf{T}} & [\mathbf{0}] \end{array}\right] \left\{ \begin{array}{c} \{\boldsymbol{v}\} \\ \{\boldsymbol{\lambda}\} \end{array} \right\} = \left\{ \begin{array}{c} \{\mathbf{F}\} \\ \{\mathbf{0}\} \end{array} \right\} \tag{2.13}$$

where $\{\boldsymbol{\lambda}\}$ is a column vector that gathers the so-called Lagrange multipliers. They are physically interpreted as the forces necessary to enforce each constraint. One of the advantages of such method is that the stiffness matrix $[\mathbf{K}]$ does not need to be recomputed when constraints are added. However, one drawback is that the number of variables increases with each new constraint. One additional comment is related to the conditioning of the global system. Instead of using values equal to ± 1 in matrix $[\mathbf{L}]$, any multiplicative constant would mathematically yield the same result. However, numerically, its order of magnitude should be that of the elements of the stiffness matrix $[\mathbf{K}]$.

Further, the similarity of Equation (2.12) and Equation (2.13) to Equation (2.8) is noticeable, highlighted on purpose using the same v nomenclature for the nodal displacement (Equation (2.4)). This observation shows one advantage of using FE meshes in DIC analyses, since the exact same discretization can be used for posterior FE analyses or in regularized DIC [85, 86]. In the former case, the measured displacement field may be used as (Dirichlet) boundary conditions for (robust) validation purposes [87]. Moreover, interpolation errors are mitigated since the quantities are measured and calculated at the very same positions (*i.e.,* nodes). In this context, Lagrange multipliers can be used, as example, for enforcing displacement of hanging nodes on mesh adaption [88] or for checking kinematic compatibility hypothesis [89], but also has the potential to be applied directly in the crack path and subsequently relaxed once damage starts.

Some studies can be found using FE analyses to simulate WSTs. A numerical study via thermomechanical simulations of the WST was reported in Ref. [90]. The authors used multiscale FE modeling, coupling one macroscale damage variable and a microscale fracture model, which was also suitable for thermal shock simulations. Fracture parameters were estimated by an inverse procedure searching for the best force vs. displacement fit between experiments and simulations [91]. A heterogeneous continuum model was implemented to investigate the fracture process in refractories. The loading curve was fitted to experimental data. The strain fields extracted from DIC analyses were qualitatively compared with the simulated cracking behavior [92]. However, none of the previously cited studies utilized full-field measurements in the identification schemes. In previous works related to the present thesis project, DIC results were used to drive FE simulations, and also validate them using displacement and gray level residuals, to find crack tip positions and stress intensity factors [54], and finally to calibrate the parameters of a cohesive zone model [70]. More details about these last two studies can be found in the Master thesis of the present author [93].

2.7 Constitutive models

When defining an FE model, apart from defining the mesh that comprises the geometry and the boundary conditions, another critical ingredient is used constitutive model. It parameterizes the stiffness of the studied body ($[\mathbf{K}]$ in Section 2.6) and should consider stress softening when crack propagation in quasi-brittle refractories are to be simulated. In this context, so-called cohesive laws are commonly used, as introduced by Hillerborg [94], describing the stresses in a pre-defined region (*i.e.,* in cohesive elements) suitable to be damaged as a function of its opening. Such traction-separation laws are defined using usually from two to four parameters, and for concrete generally take the form of bi or trilinear models [95], depending on the underlying damage mechanisms. One drawback of this approach is having to define *a priori* the crack path, which is not always known. This can be circumvented by using enriched FE shape functions that allow for displacement discontinuities on predefined regions or where thresholds (*e.g.,* of stress or strain) are locally reached. Such approaches are known as Generalized Finite Element Method (G-FEM) [96, 97] or eXtended Finite Element Method (X-FEM) [98, 99] , “basically identical methods” [100], whose nomenclatures came from developments of similar procedures in different universities. An interesting review about its application for modeling different materials and phenomena (*e.g.,* fracture, grain boundary, and interfaces) is presented in Ref. [100].

It is worth noting that implementing and developing any of the aforementioned models is a research topic *per se*, which is out of scope of the present thesis.

From a user perspective, focus was given on models that were already implemented in the Abaqus software, available in both universities in which this thesis was developed. The PPR [101], which is based on a unified polynomial-based potential, aims to provide a general framework suitable for a wide range of cases (*e.g.,* brittle or ductile materials under pure or mixed-mode loading) while curing some non-physical responses that may happen in some cases when using standard Abaqus cohesive elements [102]. Although not directly available in the software, the authors wrote an Abaqus User ELement (UEL) and made it available [103], along with tutorials and examples to facilitate its usage and modifications. Another possibility is to use the plastic-damage model proposed by Lee and Fenves [104] after some modifications of the model of Lubliner et al. [105], implemented in Abaqus under the nomenclature Concrete Damaged Plasticity (CDP), especially interesting for simulating cyclic cases. This model decouples the damage variable in tension and compression while also allowing for plastic deformation, useful for simulating unloading in ceramics with toughening mechanisms, where, for instance, there may be friction among the crack surfaces upon unloading.

2.8 Finite Element Model Updating (FEMU)

Several mechanical experiments were developed to isolate known loading states in order to obtain one property of interest analytically. For instance, tensile and compressive tests give direct access to the Young's modulus and Poisson's ratio, three or four point-bend tests are performed for obtaining the ultimate tensile strength, and the WST is mainly used for estimating the fracture energy. However, even for these setups, the rich data provided by full-field measurement techniques such as DIC when coupled to numerical simulations (for instance, with FE simulations) may provide further insight into the material behavior.

Introduced in the early 1970s [106], Finite Element Model Updating (or Finite Element Method Updating (FEMU)) is one technique that allows experiments and numerical simulations to be coupled. One interesting review about full-field based identification methods can be found in Ref. [107], in which the authors discuss how FEMU is “conceptually the most intuitive approach” among the ones addressed, being able to tackle a multitude of cases with the drawback of sometimes being computationally intensive. Similarly, in Chapter 9 of the book *Full-Field Measurements and Identification in Solid Mechanics*, devoted entirely to FEMU [108], words like versatility and flexibility appear due to the large number of situations and data that it may handle. Another discussion about going from “big data” to “key data” is presented in Ref. [109], providing insights into how to master and optimize the data flow through parameter identification steps with minimum uncertainties and maximum robustness. Hereafter, the FEMU framework discussed herein is based on Ref. [110], with an optimal metric accounting for experimental uncertainties.

In general terms, the cost function to be minimized consists in the sum of normalized squared differences, χ^2, among the measured quantities, indicated herein by the subscript m, and their simulated counterparts, with subscript FE, weighted by the experimental standard uncertainty γ [87]. In order to exemplify such usage, some particular cases of interest are discussed. First, FEMU-F consists in using only the forces measured by, say, one load cell in the calibration scheme. In that case, force acquisitions are gathered at different time steps t_F and the number of force measurements in time is N_{t_F}. Last, if γ_F is the force uncertainty (*e.g.,* from the load cell or from the numerical simulation) the cost function χ_F becomes

$$\chi_F^2(\{\mathbf{p}\}) = \frac{1}{N_{t_F}} \sum_{t_F=1}^{N_{t_F}} \left(\frac{F_m(t_F) - F_{FE}(t_F, \{\mathbf{p}\})}{\gamma_F} \right)^2 \qquad (2.14)$$

The vector $\{\mathbf{p}\}$ gathers all the parameters of interest that are subject to calibration, and may include material parameters, boundary conditions, and/or geometric features. It is worth noting in Equation (2.14) that χ_F tends to unity if the errors are only due to experimental noise. Moreover, the resulting χ_F value is a direct indicator of how many times the experimental force uncertainty is not well described by the FE model.

Similarly, FEMU with displacements in the cost function (FEMU-U) is used if only nodal displacements $\{\upsilon\}$ measured via DIC (or DVC) from a finite element mesh are considered. Instead of only one measurement per time step, in the present case, their number is directly related to the number of degrees of freedom N_{DOF}, *i.e.,* twice or thrice the number of nodes, depending if 2D or 3D cases are considered. A total of N_{t_u} different t_u time steps in which the images (or volumes) were acquired is considered, and consequently, χ_U is written as

$$\chi_U^2(\{\mathbf{p}\}) = \frac{1}{N_{DOF}} \sum_{j=1}^{N_{DOF}} \frac{1}{N_{t_u}} \sum_{t_u=1}^{N_{t_u}} \left(\frac{\upsilon_{j,m}(t_u) - \upsilon_{j,FE}(t_u, \{\mathbf{p}\})}{\gamma_{\upsilon_j}} \right)^2 \tag{2.15}$$

where γ_{υ_j} is the standard uncertainty for the displacement of a given degree of freedom, which can be substituted by a constant γ_U if the standard uncertainty is identical in the whole mesh. Presently, χ_U also tends to unity if errors are only due to experimental uncertainties.

To combine the two aforementioned cases, FEMU with displacements and forces in the cost function (FEMU-UF) consists in minimizing the weighted cost function χ_{UF} instead

$$\chi_{UF}^2(\{\mathbf{p}\}) = \frac{1}{(N_{DOF}N_{t_u} + N_{t_f})} \left[\sum_{j=1}^{N_{DOF}} \sum_{t_u=1}^{N_{t_u}} \left(\frac{\upsilon_{j,m}(t_u) - \upsilon_{j,FE}(t_u, \{\mathbf{p}\})}{\gamma_{\upsilon_j}} \right)^2 + \sum_{t_F=1}^{N_{t_F}} \left(\frac{F_m(t_F) - F_{FE}(t_F, \{\mathbf{p}\})}{\gamma_F} \right)^2 \right] \tag{2.16}$$

Force data acquired via different load cells and displacement or temperature for different regions can be included in cost functions provided their numerical twin exists. For instance, the calibration of parameters using FEMU-F-NOD is discussed in Section 4.1. Moreover, they can also be assessed at different frequencies throughout the experiment, as exemplified in Equation (2.16) with t_F not necessarily equal to t_u. This is commonly the case for images (or volumes) being acquired at slower rates than point data from the testing machines (*e.g.,* load cell, extensometers, strain gages).

It is important to first check whether the measured quantities are sensitive to the chosen parameter. This study can be performed by analyzing sensitivity matrices, as exemplified for force measurements

$$[\mathbf{S_F}] = \frac{1}{\gamma_F}\left[\frac{\partial F_{FE}}{\partial\{\mathbf{p}\}}(\{\tilde{\mathbf{p}}\})\right] \tag{2.17}$$

that are calculated, for instance, by finite differences, using an initial guess for the parameters ($\{\mathbf{p_0}\}$), since analytical solutions are usually not available. If the sensitivity is too low for some parameters, it may cause ill-posedness of the problem, and it is advised to check if the initial guess or parameterization may be somehow improved (*e.g.,* removing or coupling some parameters). Although not always practical, adding new quantities to the minimization scheme may also cure ill-posed solutions, provided their numerical counterparts are sensitive to variations of some (or all) of the sought parameters. Another point worth mentioning is that, as written in Equation (2.17), normalized by γ_F, such sensitivities are expressed as a signal to noise ratio (SNR). Therefore, ideally, the sensitivity (in absolute value) should be above unity overall for the well-posedness of the calibration, meaning that when parameters are changed, the calculated quantity changes more than its uncertainty. Care should be taken since the temporal evolution also plays an important role and even cases with SNRs less than unity (for some time steps) may be used, if their sensitivity is temporally different from other quantities. For example, on the WST, nodal displacements in regions close to the pre-notch may be relevant for all the time steps while nodes at the bottom of the sample may provide significant displacement only after the crack propagated close to it. Similarly, for the parameters, sensitivities for the fracture energy of the cohesive elements is usually very low at the beginning but increases as more elements start to be damaged.

Continuing the example about the force measurements, Equation (2.14) is then minimized through an iterative procedure where the parameters for the current iteration $\{\mathbf{p^{(n)}}\}$ are updated by solving linear systems

$$[\mathbf{H_F}]\{\delta\mathbf{p}\} = \{\mathbf{h_F}\} \tag{2.18}$$

in which the Hessian matrix $[\mathbf{H_F}]$ reads

$$[\mathbf{H_F}] = [\mathbf{S}_F]^{\mathsf{T}}[\mathbf{S}_F] \tag{2.19}$$

and the right-hand member $\{\mathbf{h_F}\}$

$$\{\mathbf{h_F}\} = [\mathbf{S}_F]^{\mathsf{T}}\left\{\frac{F_m(t_F) - F_{\mathsf{FE}}(t_F, \{\mathbf{p_n}\})}{\gamma_F}\right\} \tag{2.20}$$

where $\{\delta\mathbf{p}\}$ are the parameters corrections wrt. their current estimates. It is worth noting that the previously mentioned sensitivity fields together with the residuals (needed to calculate $\{\mathbf{h_F}\}$) provide interesting sources of insight into improving the identification quality, highlighting where (or/and when) the numerical model has to be improved [111], no matter what modality of measurements is used in the cost functions. Moreover, the construction of sensitivity fields, Hessian matrices, and right-hand members for FEMU calibrations with other measurements than force are analogous to what is exemplified above [52, 87]. Pierron and Grédiac [112] refer to the trend of improving experimental setups to fully exploit full-field measurement as “Material Testing 2.0”. Ref. [113] brings one recent review about applications in this context, with most references discussing polymer matrix composites or metals. From the 203 references, only five discuss ceramic materials (and on dynamic loading), shedding light on all the opportunities in that area.

2.9 Conclusion of the bibliographic review

This bibliographic review aimed to highlight the theoretical background of this thesis. First, the importance of castable refractories was discussed since they are key enablers for many industries. High risks associated with hazardous environments in which they are used, together with their crucial role on mitigating climatic changes and their inherent complex microstructure with the inevitable presence of cracks, lead to a constant search for a better understanding of fracture mechanisms and improved formulations with enhanced properties.

Stable crack propagation can be achieved in such brittle materials using the WST setup, and thus can be used to study toughening mechanisms and evaluate fracture properties. However, its richness of information is often unused and can be further explored. In this work, it is proposed to develop the required tools to perform this potentially rich mechanical test in high-temperature environments for understanding toughening mechanisms closer to the application temperature. Further, bulk analyzes using volumetric data from room-temperature in-situ tests in a tomograph were also conducted.

DIC, DVC, and FEM are the chosen numerical tools to fully exploit all these data. DIC and DVC give access to full-field measurements instead of point-data, to better understand and quantify localized phenomena such as cracks or phase transformation in aggregates. They also give access to actual boundary conditions for FE models, and crucial data for validation purposes. The identification of parameters for FE simulations via FEMU aims to calibrate numerical models with high robustness and exploiting all the gathered experimental data. Once these models are calibrated, they may be used to provide further insight into the thermomechanical behavior of the studied material, and allow for simulating parts directly with the application geometries to optimize projects and predict the in-service lifetime.

3 MATERIAL, METHODOLOGICAL DEVELOPMENTS, AND METHODS

Before introducing the material in this section, it is important to remember that the objective is to study crack propagation in two WST setups, namely, high-temperatures assisted with DIC and room-temperature inside a tomograph assisted with DVC. In this chapter, the material selected for this thesis is first introduced, highlighting the required features for the proposed studies in both setups. Then, focus is given on the methods that needed to be developed. For example, the setup for thermomechanical experiments with windows for visualization and lighting the specimen inside the furnace for the former and the sample geometry for tomographic analyses with crack propagation for the latter. Last, the methods that were used for each case are introduced.

3.1 Material selection and samples

The castable refractory selected for the present thesis is a commercial composition, kindly provided by IBAR, called SUPERCASTIBAR 85 MZ. It consists of a high-alumina castable with low cement and aggregates made of fused mullite-zirconia. The data sheet from IBAR is provided in Annex A, showing that this material contains Al_2O_3, ZrO_2, SiO_2, CaO and Fe_2O_3 in decreasing content order (86.0, 8.0, 4.0, 1.8 and 0.1wt%, respectively) along with some other pieces of information.

For producing the samples, the mixture was homogenized after the addition of 5.2wt% of water and then molded in the desired geometries (Figure 2.2) as described in the following sections. The samples were then cured for 24 h at room-temperature with 80% humidity, and then dried at 110℃ for another 24 h. For sintering, a heating rate of 3℃/min was used, and then a 5 h dwell at 1400℃ for the first batch of samples, and 1450℃ for the second one. Last, cooling down was set to the same rate of 3℃/min.

To check the phases of the underlying composition, Energy Dispersive X-Ray Spectroscopy was considered, using 25 kV in two regions, namely, one comprising only the matrix and one only for one mullite-zirconia aggregate. In the matrix, the material consists of alumina. An SEM image of one aggregate is shown in

Figure 3.1, in which the oxide composition was found to be 53 wt% Al_2O_3, 14 wt% SiO_2, and 33 wt% ZrO_2. Primary zirconia particles in the darker matrix are shown in the bottom region, while acicular zirconia formations are seen at the top in a brighter matrix. Having these different formations in the microstructure is interesting for crack propagation studies since they may lead to different toughening mechanisms, for instance, deflecting the crack differently, although their individual contributions would be hardly distinguishable in this case.

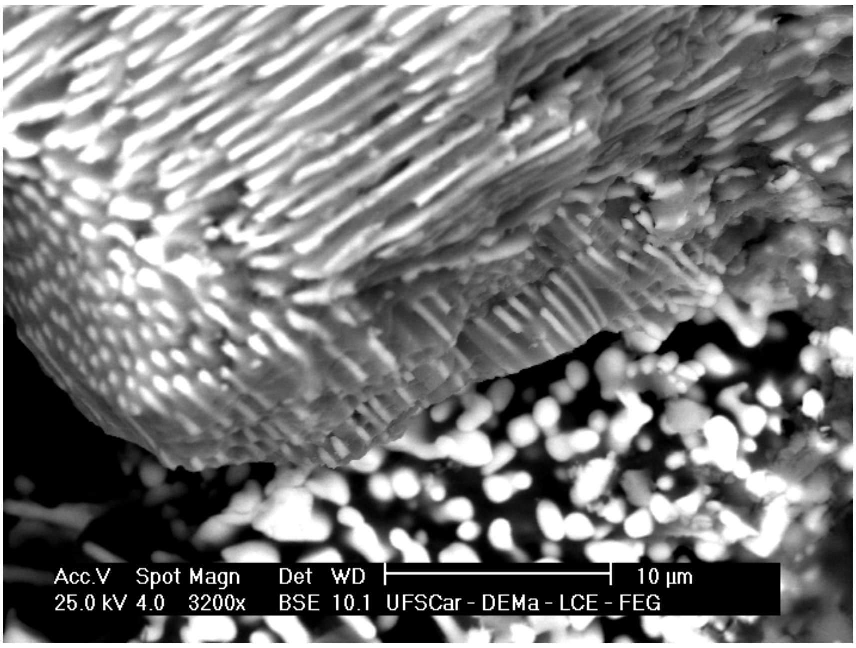

Figure 3.1: SEM image of fused mullite-zirconia aggregate showing acicular and nodular formations of zirconia in brighter hues.

The aggregate composition is shown inside the Al_2O_3-SiO_2-ZrO_2 composition triangle in Figure 3.2, on the boundary of the zirconia-mullite compatibility region [114], where a solid solution with mullite is possible. In Ref. [114], the authors analyzed several compositions of the same system, among which 55-15-30 and 50-15-35, which are very close to the 53-14-33 composition obtained herein. In both (similar) compositions, the authors found alumina, mullite, and zirconia phases. Moreover, these compositions lie close to the eutectic point involving alumina, mullite, and zirconia [114] (at 58-11-31 composition), which is consistent with the acicular formation seen in Figure 3.1. The aggregates of the material studied herein is thus believed to contain these very same phases, with little alumina since it is in the periphery of the zirconia-alumina-mullite compatibility triangle, very close to the mullite-zirconia side. Such observation is further confirmed by the X-ray diffractometry of the mullite-zirconia aggregates provided by IBAR (Annex B), whose peaks indicate that the zirconia in the raw material at room temperature was monoclinic [115]. It is worth noting that during sintering it may transform to a tetragonal phase and be kept metastable after cooling due to mechanical constraints from the sintered matrix [30].

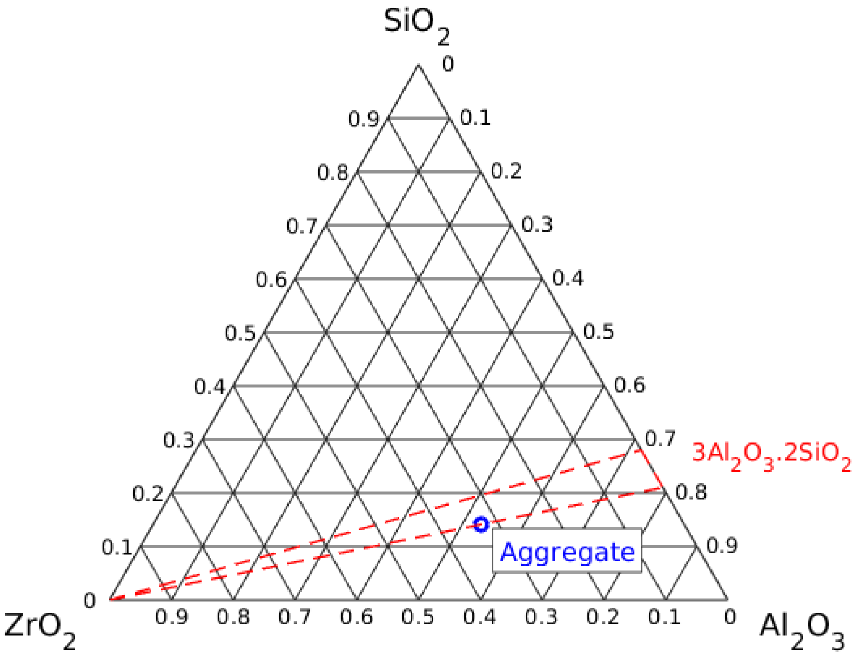

Figure 3.2: Aggregate composition in the Al_2O_3-SiO_2-ZrO_2 composition triangle (in wt%). The region inside the red dashed lines represents the Alkemade line between zirconia and mullite (after Ref. [114]).

A total of 11 WSTs are reported along this thesis. Each sample will be called in chronological order and divided into two groups, prismatic or cylindrical samples, always preceded by MZ to remind the mullite-zirconia composition of the aggregates. For the prismatic samples, they will have an indicator of the sintering temperature and the presence or not of lateral grooves to guide the crack. This nomenclature was first introduced with part of these experiments in Ref. [116]. For example, MZ1-S1450G is the first sample, sintered at 1450℃ with lateral grooves, and MZ2-S1400 is the second sintered at 1400℃ and with no lateral grooves. The first five samples were tested up to 600℃ and are discussed in Section 3.3.2 while the last one was performed at 900 ℃ and described in Section 3.3.3. For the cylindrical samples, a similar nomenclature will be used, restarting the counting for conciseness and indicated with a C (*e.g.,* MZC1-S1450G or MZC3-S1450). These samples were all sintered at 1450 ℃, but the temperature indication is kept for comparison purposes. It is worth noting that the first two cylindrical samples were slightly smaller than the others (by 12 mm and 15 mm, respectively) since the molds were not fully filled during their production. Moreover, since their notches were made by a razor blade, their depth slightly differed between samples ranging from 13 mm to 15 mm.

The studied material has not only technological relevance, but also a well known toughening mechanism related to zirconia phase transformation. This feature may significantly alter its mechanical behavior, especially around 900 ℃, and therefore was a suitable choice for the thermomechanical experiments. This material system also contains phases in its microstructure with different X-ray attenuation coefficients, namely, the alumina matrix and the zirconia aggregates, which increase the gray level contrast in the reconstructed volumes in tomographic analyses, allowing DVC to be performed. Such contrast is seen in the 3D renderings shown in Figure 3.3, where porosities appear in black, the alumina matrix in darker gray and zirconia-rich aggregates in brighter gray levels.

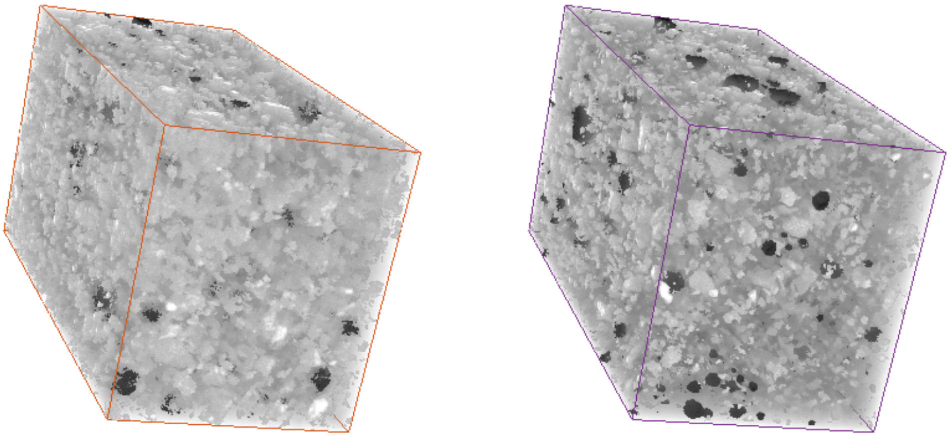
(a)

(b)

Figure 3.3: 3D rendering of $\approx 29 \times 25 \times 52$ mm^3 tomographic volumes of samples (a) MZ2-S1400 and (b) MZ4-S1450 (adapted from Ref. [117]).

3.2 Methodological developments

This section gathers all the needed methodological developments in order to have suitable setups for performing WSTs, whether at higher temperatures or inside the tomograph (at room temperature), and for analyzing the resulting data. First, Section 3.2.1 studies the relationship between displacements close to the notch and to the load application area, since the latter was not visible in the 600 ℃ setup, that will be referred to as F600 hereafter. Such relationship was used in FEMU calibrations of material parameters. Second, a furnace partially based on the F600 setup was designed and built, allowing WSTs to be performed up to 900 ℃ while monitoring opposite faces of the tested samples. This second furnace (F900) is further detailed in Section 3.2.2. It is worth noting that bigger windows were designed for the F900 setup, which made it possible to visualize both the load application area and the crack propagation path, with some limitations that will be discussed. Last, molds were developed to make cylindrical samples suited for *in-situ* (inside the x-ray tomograph)[1] WSTs, as discussed in Section 3.2.3, in order to diminish tomographic artifacts.

3.2.1 Out of sight boundary conditions

Part of the experiments were performed in a furnace (F600) where the limited dimensions of the window did not allow the vision of an important region of the sample where the cylinders and plates apply the load, as shown in Figure 3.4(a). With a limited FOV, the choice was to focus on crack propagation instead of the force application region. Therefore, for setting the FE simulations, developments were needed to properly address the definition of boundary conditions. For such task, previous WSTs performed at room temperature, on another material, but with the whole surface visible as shown in Figure 3.4(b), were used to derive the relationship between the opening displacements at the crack mouth (CMOD, cyan in Figure 3.4) and in the notch (NOD, yellow in Figure 3.4). For these experiments, images from both sides of the sample were also available, thereby allowing for further verification of possible errors related to having windows for only one side of the furnace.

---

[1] From this point onward, *in-situ* will be used to recall the setup inside the tomograph

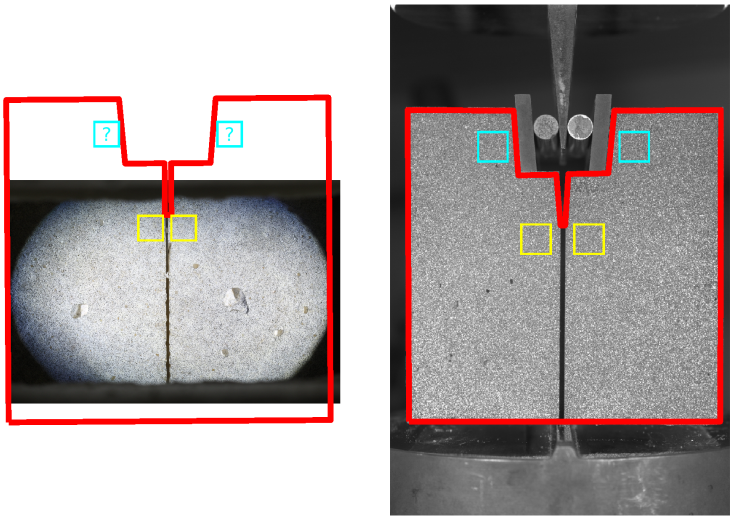

(a) (b)

Figure 3.4: Reference images for WSTs with (a) the F600 setup with a limited FOV and (b) previous room temperature tests with the whole sample surface accessible. The yellow boxes depict the regions used for NOD measurements, while the cyan boxes are the areas to evaluate CMODs (adapted from Ref. [118]).

Two experiments performed on an anti-erosive commercial refractory castable (grade DD40 [119–121]) were used in such analyzes. Their loading curves are shown in Figure 3.5. The first one consisted in a monotonic loading down – after ultimate load – to very low force levels (Figure 3.5(a)), while the second had five cycles (Figure 3.5(b)) and stopped at 70% of the ultimate load, aiming to arrest the crack about half the height of the sample. For the former, both lateral surfaces of the specimen could not be seen in the image since a zoom was made on the propagation path and CMOD region, while for the latter the whole sample was visible as shown in Figure 3.4(b).

From the experimental NOD vs. CMOD curves shown in Figure 3.6, it was proposed to use a quadratic relationship in the pre-peak regime

$$\bar{\delta} = \left(\frac{R}{c} - 1\right)\bar{\Delta}^2 + \left(2 - \frac{R}{c}\right)\bar{\Delta} \tag{3.1}$$

while an affine function could be used beyond the ultimate load

$$\bar{\delta} - 1 = \frac{R}{c}\left(\bar{\Delta} - 1\right) \tag{3.2}$$

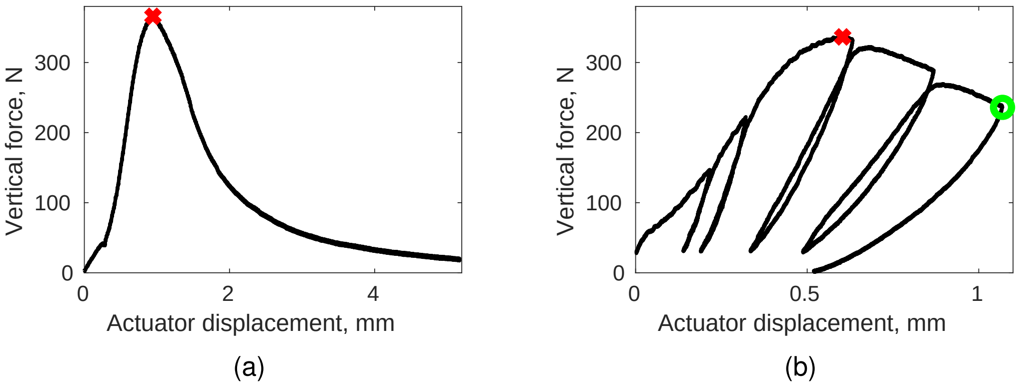

Figure 3.5: Load history of the (a) monotonic and (b) cyclic WSTs carried out on the DD40 grade. The red cross depicts the ultimate force level. In sub-figure (b), the green circle represents 70% of the ultimate load (*i.e.,* the end of the envelope) (adapted from Ref. [118]).

where $\overline{\delta}$ and $\overline{\Delta}$ are the NOD and CMOD normalized by their respective levels at the ultimate load, c the affine-fit slope, and R the ratio of CMOD and NOD at the ultimate load. Both curves are made C1 continuous at the ultimate load. Provided the NOD is known, only two parameters (*i.e.,* c and R) are needed in this framework to obtain an estimate of CMOD. Such extrapolation of CMOD from NOD data are shown as dots in Figure 3.6, designated as “initiation” and “propagation,” respectively, and their R-squared values are given above the graphs, showing how well this hypothesis is consistent with experimental data.

For further details about these equations and developments, the interested reader is referred to Ref. [118], which resulted from this thesis, where it was first presented. Although the needed c and R parameters are not directly available when CMOD is not measured, they were calibrated together with cohesive parameters via FEMU using both force and NOD data in the cost functions [122] for the same experiments, further validating the methodology. It is worth noting that Equations (3.1) and (3.2) are not suitable for unloadings and reloadings in cyclic cases, which still needs further developments.

3.2.2 Furnace for thermomechanical experiments assisted by DIC

In the context of this thesis, the so-called F900 furnace that allows for temperatures reaching up to 900 ℃ and photographing both opposite sides of the sample

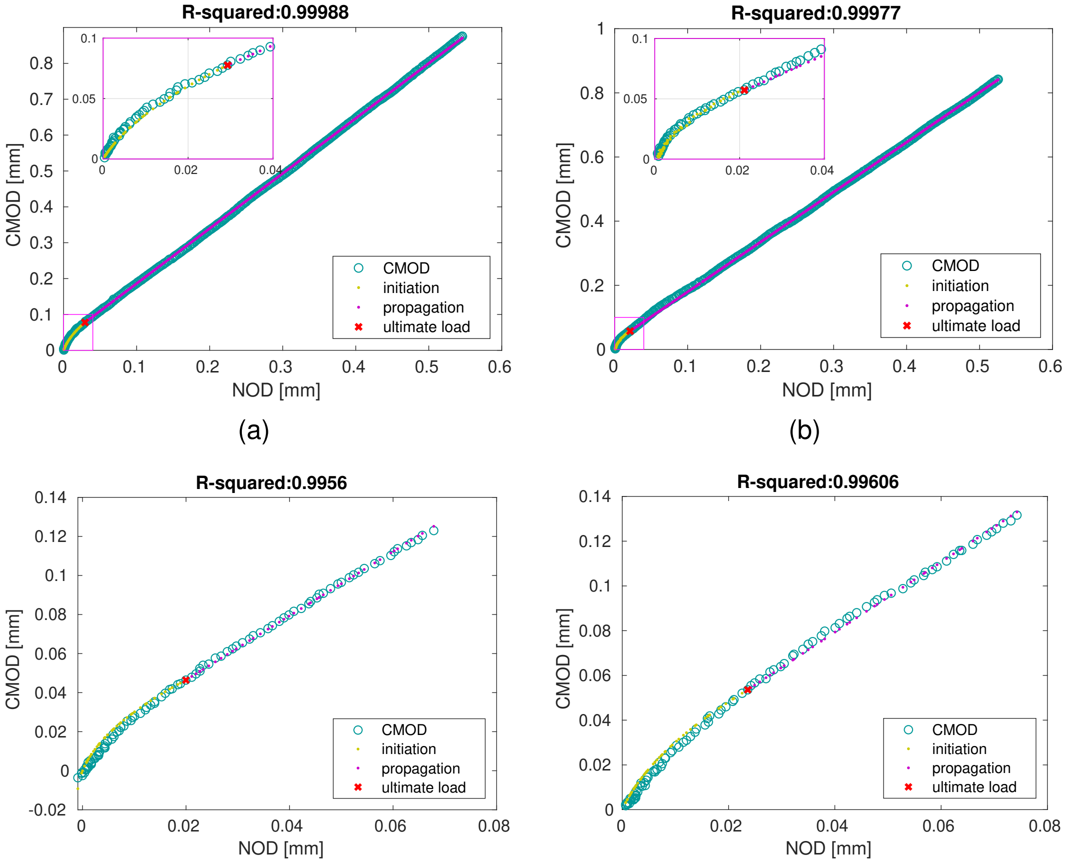

(a) (b)

(c) (d)

Figure 3.6: CMOD vs. NOD histories in the monotonic (a,b) and envelope of the cyclic (c,d) WST on DD40, for the front (a,c) and back faces (b,d). The quadratic and affine fits are also shown in yellow and purple, respectively, while the ultimate load is depicted as a red cross. The insets (purple boxes in sub-figures (a,b)) concentrate on low levels of NOD and CMOD (adapted from Ref. [118]).

was designed and built. It was also conceived to be coupled to the electromechanical testing machine available at the Brazilian laboratory, namely, one MTS E44.304 (30 kN capacity) model. All the parts were drawn in the Inventor CAD software, and the main features are highlighted in Figure 3.7(a). Two controllers are used to have two heating zones along the vertical direction to decrease the temperature gradients on the monitored region. It was necessary to plan how to move the setup in and out of the testing machine, since it was not exclusively dedicated to such experiments. Such modular approach consists of a U beam with rails for easier alignment and positioning of the whole setup together with detachable parts, which is shown in Figure 3.7(b). For instance, the central part of the furnace is put in the center of the U beam over four guiding pins to ensure the alignment of the hole made for the actuator. Moreover, the windows are also attached over the guiding pins, but on gliding supports that allow the furnace to be opened and closed. Similarly, the supports for the cameras and illumination are put on the rails to maintain the alignment and for easy adjustment of the distances from the sample surfaces. An image of the heated sample inside the setup is shown in Figure 3.7(c).

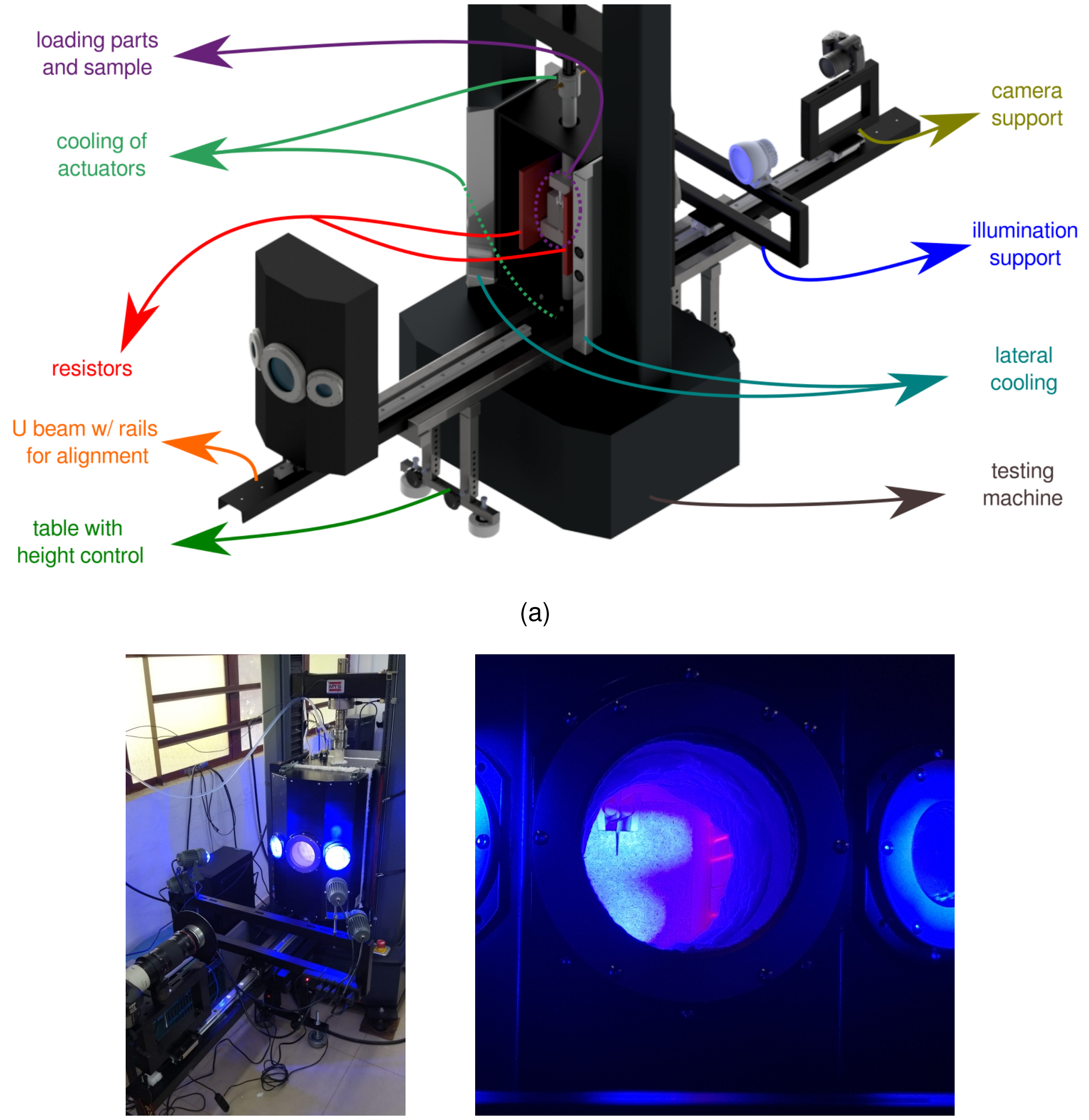

(a)

(b)

(c)

Figure 3.7: (a) 3D assembly of the developed setup to perform WSTs up to 900 ℃ and (b) the resulting setup, with (c) a zoom in the WST specimen at 900 ℃

.

Cooling parts had to be added not to damage neither the lateral columns of the testing machine nor its load cell. A system made of aluminum sheets and small fans was designed and attached in the 20 mm gap between the furnace and the columns, to avoid the columns of the testing machine to overheat. Another cooling part is used at the outer end of each actuator, with inner water channels linked to a pump whose objective is to remove heat from the system and to keep the load cell temperature below 40 °C (the limit given by the manufacturer for temperature compensation). All this setup was mounted over a table with height adjustment, which could also be used for easier alignment of cameras on other mechanical experiments without the furnace. The U beam also allows this setup to be used out of the testing machine (*e.g.,* for performing dilatometry tests).

Loading parts

To perform WSTs in the F900 setup, dedicated loading parts, shown in Figure 3.8, were designed and made out of a refractory mortar. The top part has a groove to fit the wedge and the bottom part to fit the parallelepipedic support for the sample. Since the testing machine is a multi-user equipment, these parts were designed to allow three or four-point bend experiments to be performed by rotating the top part 90° about the loading axis. The bottom part 150 mm in width helps the sample to be held after fracture, lowering the risk of damaging the heating elements.

To build such loading parts, the molds were first made from additive manufacturing as shown in Figure 3.9. For the first trial, duct tape was applied in the PLA molds together with grease to allow for unmolding. However, sharp corners around the circular parts (see Figure 3.9) where the actuators would be supported induced cracking of the refractory parts during drying. For the second trial, the geometry had smoother corners to solve such issues. ABS was used instead of PLA to enable acetone vapor to be utilized for achieving smoother surfaces and also for drying in slightly higher temperatures if needed. These second molds were used not long after being removed from acetone vapor, such that it shrank and blocked unmolding. The molds had to be destroyed to remove the parts, but the refractory parts were successfully made and are used for the analysis dis-

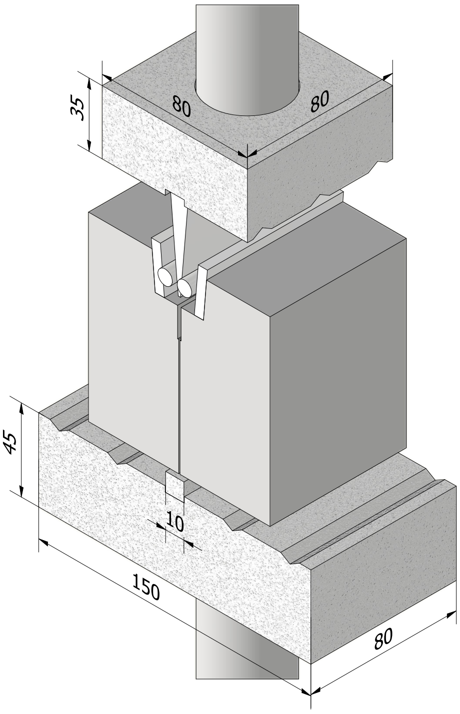

Figure 3.8: 900 °C WST setup showing the overall dimensions (in mm).

cussed herein. One advantage of such route is that it allows for fast prototyping with different geometries and fast replacement in case these parts break during experiments.

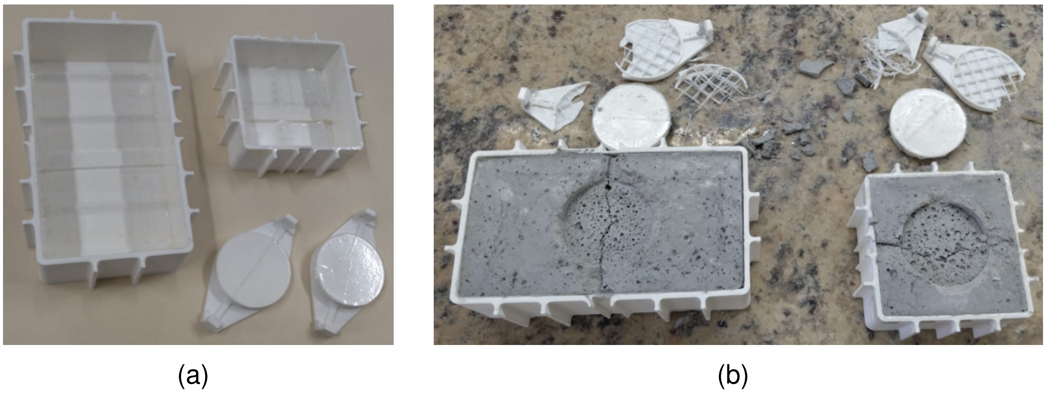
(a) (b)

Figure 3.9: (a) First empty molds made of PLA for producing loading parts from refractory mortar and (b) during unmolding with cracked refractory parts.

Similarly, the actuators were made of refractory mortar, but using a PVC pipe as mold with a machined polyethylene cap at the bottom. The challenge lied in the drying phase, since the open surface for drying was only a circle of 50 mm in diameter for the whole part (300 mm in height). After some trials, two viable actuators could be fabricated. The top one had a small reduction in diameter ground some millimeters away from one flat surface for fixing it on the moving part of the testing machine to apply load.

Windows, illumination and filters

Six transparent modules were used, three in each sliding window of the F900 setup. Each module consisted of two quartz disks, separated by an alumina tube of approximately 50 mm in height and 5 mm in thickness. Each window has a bigger central module for visualization purposes and two lateral modules for illumination, at 30° angle from the former, with transparent FOV of 110 mm and 50 mm in diameter, respectively. For illumination purposes, two 10 W mounted blue LEDs with 800 lumens were used for each module. They were attached to an illumination support (Figure 3.7) to allow for easier positioning.

Some filters are also used during image acquisition. A hot mirror (FM201 from Thorlabs) was first utilized to protect the camera by reflecting the infrared radiation. Then, a blue bandpass filter (In the 360–580 nm range, FGB39S from Thorlabs) was selected to avoid acquisition of the strong red light radiated by the heated sample, to have constant gray levels (temperature-wise) of the monitored samples. Last, neutral density filters (one ND2000 from Rise(UK) and one variable ND2-ND400 from K&F Concept) allowed the brightness in the images to be controlled even for high exposure durations (*i.e.,* above one second), to mitigate heat haze effects.

3.2.3 WST geometry for *in-situ* (tomography) experiments

Cylindrical samples were selected in order to reduce beam hardening effects related to the X-rays traversing different lengths of material in prismatic samples. This effect is seen in the slice of the tomographic volume of one prismatic sample (Figure 3.10(a)) in the form of diagonal lines and darker hues on the corners. Such artifact is not visible in the slice of the cylindrical sample shown in Figure 3.10(b). It is worth emphasizing that such artifacts do not make DVC analyses impossible, but additional corrections for them could be needed.

Based on the mold used for standard WST samples [37], similar molds were

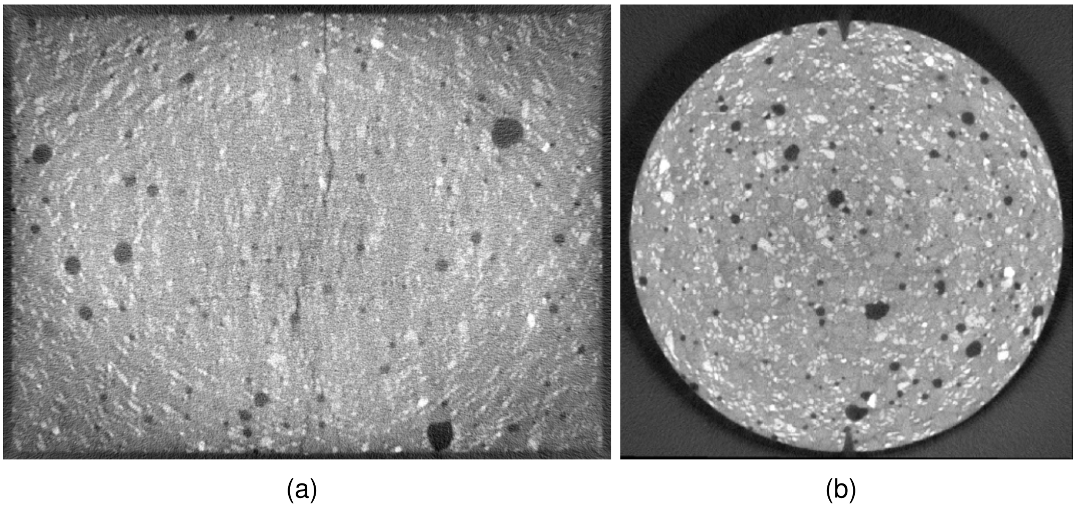
(a) (b)

Figure 3.10: Slices of tomographic volumes for WST samples made from the same material studied in this thesis but with a (a) prismatic and (b) cylindrical geometry. In sub-figure (a), the tomographic artifact known as beam hardening is as diagonal lines and darker hues closer to the corners.

designed and 3D printed for the studies of this thesis (Figure 3.11), considering the same loading parts that already existed. For the notch to initiate crack propagation, a commercial snap off blade was attached to the mold. This mold geometry was designed to allow it to be well fastened and avoid leakage of the castable while on the vibratory table during processing. Small triangular protrusions are also used to make lateral grooves to guide crack propagation (Figure 3.10(b)). Although this geometry allowed the methodology to be developed, some improvements may be implemented for more trustworthy investigations of materials, as will be discussed in Section 4.3.6.

3.3 Experimental WST setups and experiments

3.3.1 Loading parts

For the WST setup used herein, a wedge, two cylinders, two lateral blocks and a support for the bottom surface of the sample are required (see Figure 2.1). They were already made prior to this thesis of steel for room temperature experiments. However, aluminum parts were also required to perform in-situ WSTs inside a tomograph to reduce artifacts close to the load application region. Moreover, for high-temperature tests, these parts were produced in alumina by Ceraltec (Ibaté, Brazil). All the three sets were polished to decrease frictional effects during the

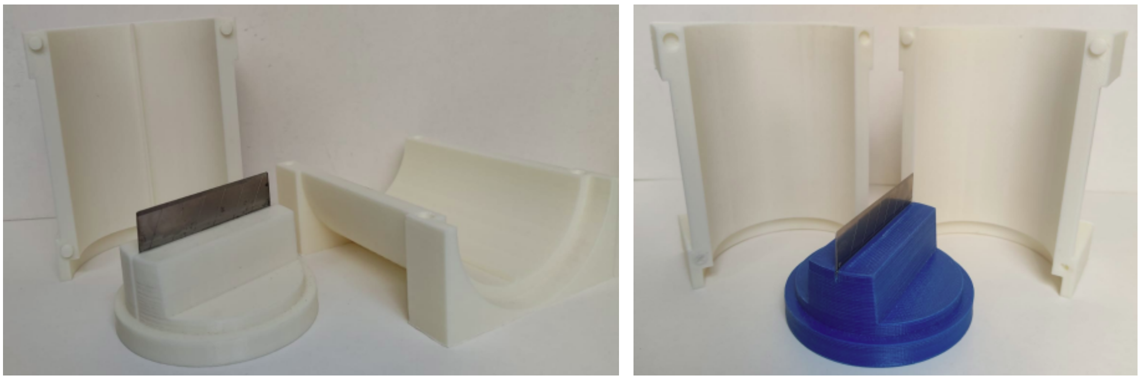

(a) (b)

Figure 3.11: Mold used to cast cylindrical WST samples (a) with and (b) without lateral grooves to guide the crack propagation (see geometry of (a) in second row of Figure 2.2).

tests.

3.3.2 F600 setup

Five samples were tested at the F600, mounted on one hydraulic testing machine equipped with a 5 kN load cell, as shown in Figure 3.12. The uncertainty of the load cell measured as the standard deviation of data gathered while a constant vertical force of 50 N was enforced in one WST sample is in the order of 10 N in terms of the splitting force. Moreover, the first sample was monotonically tested at room temperature (but inside the furnace) as a reference before the other experiments were performed at 600℃. The second sample was also tested under monotonic loading to have a first estimate of the maximum force and displacement at higher temperatures, before performing the following three samples with five cycles each. These cycles were designed such that the first and third ones would be loaded up to 350 N (vertical force), while the second would go up to the peak load, and the three unloaded until 200 N. The fourth cycle would then load up to 200 N and unload to 100 N, and the fifth cycle load up to 10% of the peak load and unload to 20 N. All the samples were pre-loaded to 50 N, all the loadings were performed at a rate of 10 µm.min^{-1}, and unloaded at 10% of the ultimate load. During heating, the testing machine was load controlled to maintain a 50 N pre-load.

This setup did not allow for the visualization of the full surface of the sample

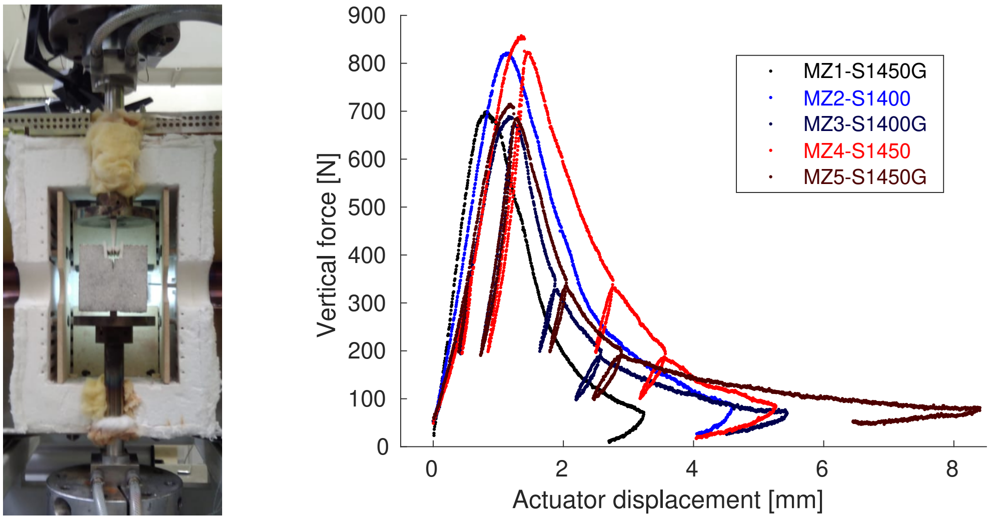

(a) (b)

Figure 3.12: (a) MZ2-S1400 sample inside the F600 and (b) loading curves obtained in this setup

(Figure 3.4(a)), which called for the development of an extrapolation from NOD to CMOD (discussed in Section 3.2.1). Paint suitable for high-temperatures was applied onto the samples for improving the contrast for DIC purposes. After sample MZ1-S1450G was tested, the post-mortem specimen was turned 90° counterclockwise and used for a dilatometry experiment up to 600℃ for checking the heating protocol and image acquisition. The reference image acquired at room temperature is shown in Figure 3.13(a) aside the last image after the experiment in Figure 3.13(b). Severe contrast loss was seen in this experiment, which led to tests of different commercial paints, all indicating its possible use for temperatures above 600℃. Although contrast was improved for the following samples, some changes occurred during the experiments. This issue led to the development of a methodology to update references images for DIC analyses considering this loss of contrast based in Principal Component Analyses (PCA) [123].

Further details about the acquired images and setup are given in Table 3.1. One hundred reference images were acquired before the test for quantifying DIC uncertainties. At the same image acquisition rate, the number of images are directly related to the length of the test, with considerably less images for the two monotonic tests than for the cyclic ones. Last, even if the speckle pattern

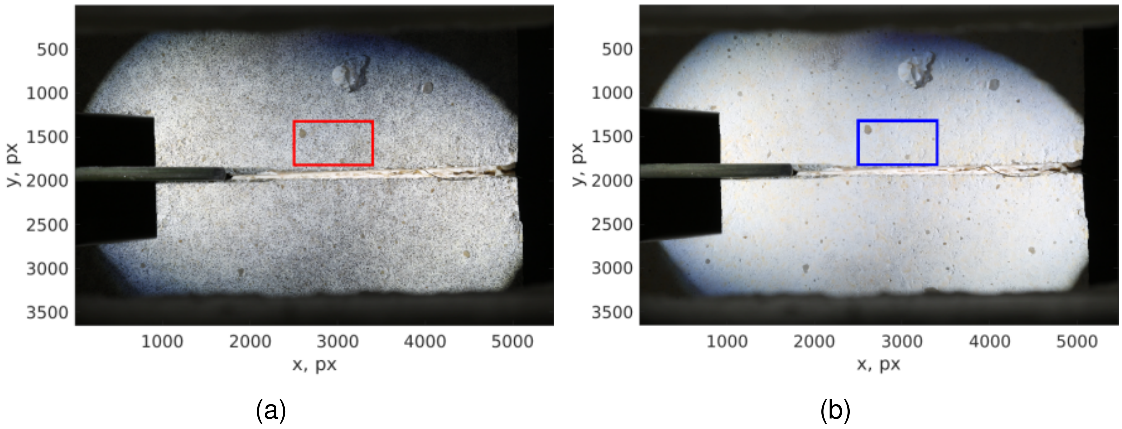

Figure 3.13: (a) Reference image acquired at the beginning of the dilatometry test on sample MZ1-S1450G. (b) Last image after the test showing severe loss of contrast. The rectangles depict the regions further discussed in Ref. [123].

was applied in a similar way to the samples, the contrast was finer for the first three than the last two samples. This trend could be caused by the longer time between patterning and performing the test, where the paint may have diffused into the specimen or partially evaporated.

Table 3.1: DIC hardware parameters for the F600 setup

Camera	Canon 70D
Reference images	100 (each sample)
Images during load	681 (MZ1-S1450G), 931 (MZ2-S1400), 1600 (MZ3-S1400G), 1659 (MZ4-S1450), 2351 (MZ5-S1450G)
Definition	5472×3648 px
Gray Levels amplitude	8 bits
Lens	Canon Macro 100
Exposition time	1/50 s
Aperture	f/8 (MZ1-S1450G) and f/10 (others)
Filters	none
Field of view	104×69 mm^2
Image scale	19 µm / px
Stand-off distance	50 cm
Image acquisition rate	0.1 fps
Patterning technique	sprayed paints
Pattern size	5 px (MZ1-S1450G, MZ2-S1400, MZ3-S1400G) 12 px (MZ4-S1450, MZ5-S1450G)

3.3.3 F900 setup

One specimen was tested on the F900 setup. As shown in Figure 3.14(a), the bottom loading part discussed in Section 3.2 was used, but not the top one, as during setup it was observed that the specimen remained more stable without it, and that the size of the actuator was sufficient to directly support the wedge. Heating was performed at 10℃/min, and a dwell of 2h30 was applied at 900℃ for stabilizing the setup. During heating, the (eletromechanical) testing machine was controlled to keep the applied force between 40 N and 50 N. From heating and, consequently thermal expansion of the setup, about 3 mm in actuator displacement were required to maintain the pre-load during this first stage. Ten reference images were acquired after reaching a pre-load of 50 N. During this acquisition, the standard deviation of the force measurements was 0.4 N, which represents about 2.3 N in terms of the splitting force. Loading then started at a rate of 10 µm/min for direct comparison to the experiments performed in the F600 setup. The splitting curve for the MZ6-S1450 specimen is shown in Figure 3.14(b), showing not only a stable crack propagation, but with a considerably higher ultimate load than those reported in Figure 3.12(b). The test was stopped post-peak at 20% of the ultimate load.

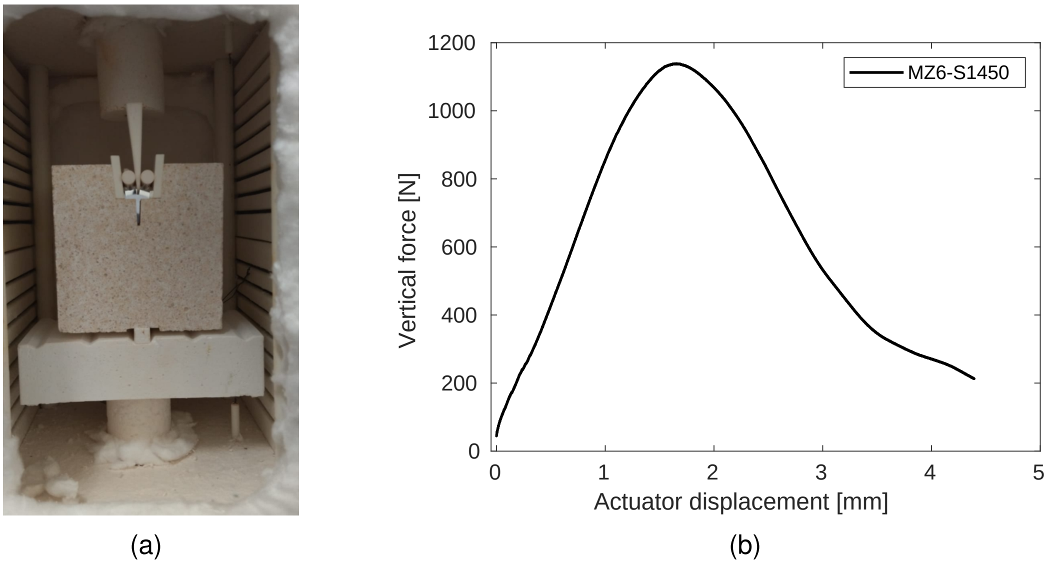

(a) (b)

Figure 3.14: (a) *Post-mortem* MZ6-S1450 sample inside the F900 furnace. (b) Loading curve obtained with the 900℃ setup

All the DIC hardware parameters for this experiment are gathered at Table 3.2. It is worth noting that although the FOV was very similar to the one reported in Table 3.1, the fact that this setup allowed this FOV to be vertical (*i.e.,* portrait orientation instead of landscape) is preferable since it gives more information about boundary conditions related to loading of the specimen. The use of blue LEDs and bandpass filters to decrease the influence of black body radiation led to a narrow range of usable gray levels (coded in 16 bits) with a dynamic range of about 2000 gray levels, considering only the blue channel. The speckle pattern created by spraying a SiC slurry provided good contrast and did not degrade during the test.

Table 3.2: DIC hardware parameters for the F900 setup

Cameras	Canon 5DS
Reference images	10
Images during load	848
Definition	8736×5856 px
Gray Levels amplitude	16 bits
Lens	Canon Macro 180 with 2x Extender
Exposition time	2 s
Aperture	f/7.1
Filters	Hot-mirror, blue bandpass filter, and ND filters
Field of view	100×67 mm^2
Image scale	11.4 µm / px
Stand-off distance	132 cm
Image acquisition rate	0.033 fps
Patterning technique	sprayed SiC slurry
Pattern size	5 px

3.3.4 *In-situ* (tomography) setup

The first sample tested *in-situ* (*i.e.,* inside a tomograph) together with the aluminum alloy loading parts are shown in the *post-mortem* state still in the testing machine in Figure 3.15(a). A total of five cylindrical WST samples were tested in this setup, and their loading curves are displayed in Figure 3.15(b). Sample MZC1-S1450G underwent a monotonic test in which loading was stopped at plateaus for acquiring full scans. During these acquisitions, load drops were seen, which could be caused by some motions due to misalignment, accommodations, or small crack propagation. This displacement level was estimated to be less than the DVC uncertainty [124]. Projections were also acquired during loading and dwells with no rotation. These data could be used in projection-based DVC [125]. Sample MZC2-S1450G was experienced a cyclic loading. Samples MZC3-S1450, MZC4-S1450 and MZC5-S1450G were performed for projection based DVC (P-DVC) purposes [38, 125–128]. Projections were acquired on the fly while the sample was rotating non-stop in addition to the application of axial loading. Some plateaus were planned as well to have full scans to be analyzed via DVC.

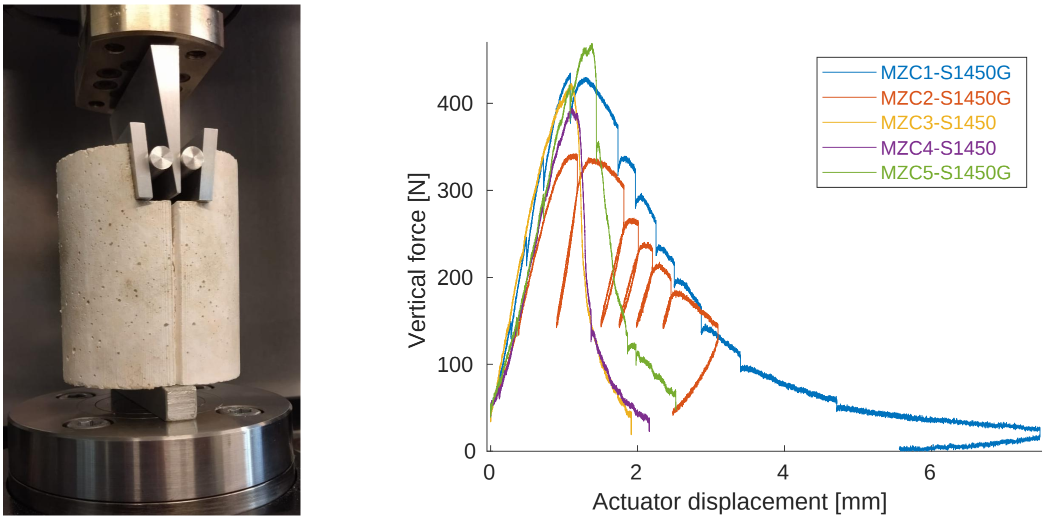

(a) (b)

Figure 3.15: (a) *Post-mortem* MZC1-S1450G sample inside the tomograph. (b) Loading curves obtained with the in-situ setup

Both MZC1-S1450G and MZC2-S1450G tests had fifteen scans acquired with the tomograph and testing machine parameters shown in Table 3.3 and were analyzed with FE-based DVC with the parameters gathered in Table 3.7. Last, for MZC3-S1450, MZC4-S1450, and MZC5-S1450G samples, the crack did not propagate as expected as discussed in Section 4.3.5.

3.4 Methods

3.4.1 DIC/DVC applications

This section gathers selected results from all DIC and DVC analyses performed in the studied setups such as the reference images that are used, meshes

Table 3.3: DVC hardware parameters

Tomograph	North Star Imaging X50+
X-ray source	XRayWorX XWT-240-CT
Target / Anode	Tungsten (reflection mode)
Filter	none
Voltage	200 kV
Current	400 µA
Focal spot size	5 µm
Tube to detector	505 mm
Tube to object	226 mm
Detector	Dexela 2923
Definition	1536×1944 pixels (2×2 binning)
Number of projections	1000
Angular amplitude	360°
Frame average	10 per projection
Frame rate	10 fps
Acquisition duration	about 17 min (continuous rotation mode)
Reconstruction algorithm	filtered back-projection
Gray Level amplitude	8 bits
Volume size	$554 \times 568 \times 677$ voxels (after $2 \times 2 \times 2$ binning and crop)
Field of view	$74.6 \times 76.5 \times 91.1$ mm^3 (after $2 \times 2 \times 2$ binning and crop)
Image scale	135 µm/voxel
Testing machine	Deben TTC
Load cell capacity	± 20 kN
Actuator velocity	1 µm/s
Force uncertainty	1.4 N (standard deviation of acquisition on unloaded frame)

and their creation, as well as the choice of analysis parameters.

Experiments in the F600 setup

Since the F600 setup had a rectangular horizontal window that did not allow for the visualization of the full sample surface (Section 3.2.1), some adaptations were required for DIC analyses. The reference image for each tested sample is shown in Figure 3.16 together with the ROIs for NOD measurements (in yellow), positioned right below the end of the notch and with a distance between the squares about the width of the lateral groove. Moreover, the ROIs for analyzing the overall kinematics are also shown (in cyan, with the meshes' elements in red) trying to exploit most of the pixels while avoiding shadows in the corners and from the thermocouple on the left (starting from sample MZ2-S1400). All DIC analysis parameters for these samples are gathered in Table 3.4.

Uncertainty analyses were performed by running usual DIC calculations on the

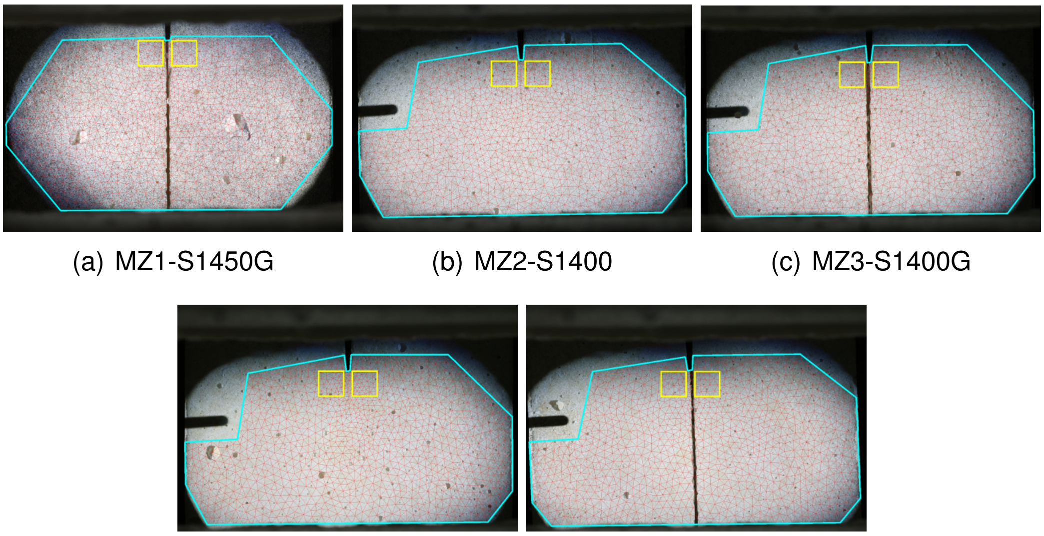
(a) MZ1-S1450G (b) MZ2-S1400 (c) MZ3-S1400G

(d) MZ4-S1450 (e) MZ5-S1450G

Figure 3.16: DIC meshes over reference images of the five tests performed inside the F600 setup. The cyan contours are the regions of interest for DIC analyses. The yellow boxes depict the areas used for NOD calculations (adapted from Ref. [116]).

Table 3.4: DIC analysis parameters for all tests performed in the F600 setup [116].

DIC software	Correli 3.0 [129]
Image filtering	none
Element length	80 px
Shape functions	linear (T3)
Mesh	see Figure 3.16
Matching criterion	penalized sum of squared differences
Interpolant	cubic
Displacement noise-floor	0.02 px (see Table 3.5)

100 reference images acquired before loading. A temporal standard deviation of the degrees of freedom for displacement and maximum principal strains ϵ_1 gives the respective maps of uncertainties. These maps for sample MZ1-S1450-G, which was tested at room temperature, are shown in Figure 3.17. It is noticeable that uncertainties are higher at outer nodes, as expected [56]. The horizontal degrees of freedom (Figure 3.17(a)) of these nodes were influenced by less pixels closer to the left or right contours, while less pixels were considered for the vertical degrees of freedom (Figure 3.17(b)) at the top and bottom contours. For the strains (Figure 3.17(c)), a higher uncertainty at the middle vertical line is seen due to the lateral groove that induced shadows in the reference images, and therefore

with very low contrast. Two small points, one on each side of the sample, are seen with higher uncertainties, which are related to big surface pores (Figure 3.16(a)).

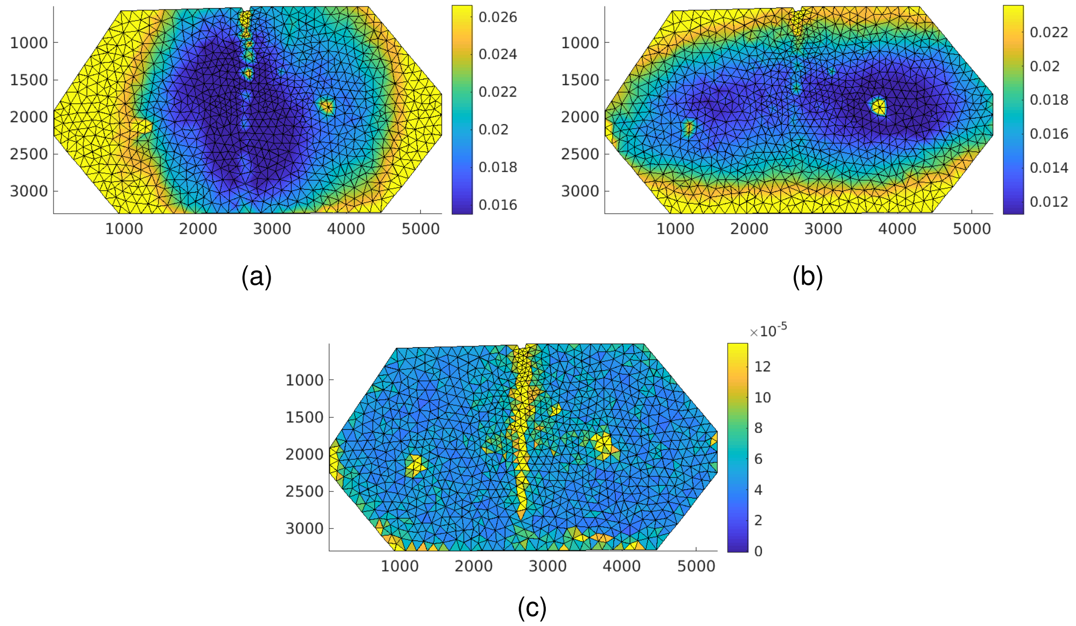

(a)

(b)

(c)

Figure 3.17: Standard uncertainty fields for sample MZ1-S1450G. Nodal displacements (expressed in px) in the (a) horizontal and (b) vertical directions, and (c) ϵ_1 for each element.

In contrast to what was shown for room temperature, similar maps but for sample MZ2-S1400, tested at 600 ℃, are given in Figure 3.18. Although the same trend around the contour is seen, heat haze effects are also visible, leading to higher values for the horizontal displacements (Figure 3.18(a)), which are caused by hot air flow inside the furnace. For the strain maps (Figure 3.18(c)), the trend follows a combination of the pattern seen in displacement maps since there was no groove in this sample (Figure 3.16(b)).

The average values of these uncertainty maps are reported in Table 3.5. An uncertainty of 2 cpx is usual for room temperature DIC setups [56], further validating the setup. It is remarkable how uncertainties rose one order of magnitude at 600 ℃ in comparison to the room temperature case, for both displacements and strains. Moreover, the horizontal uncertainty being about the double of the vertical, which is explained by heat haze and air convection inside the furnace as

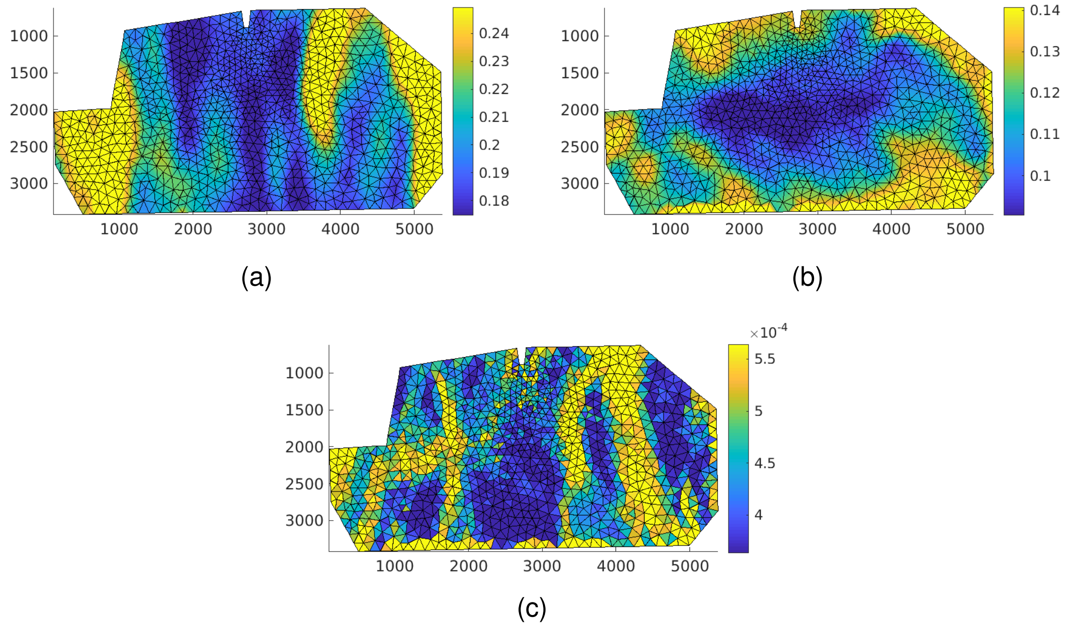

(a) (b) (c)

Figure 3.18: Standard uncertainty fields for sample MZ2-S1400. Nodal displacements (expressed in px) in the (a) horizontal and (b) vertical directions, and (c) ϵ_1 for each element.

illustrated in Figure 3.18. Standard NOD uncertainties are also of the same order of magnitude as the average displacement uncertainties in the whole ROIs.

Table 3.5: Standard displacement uncertainty for each test made in the F600 setup, in the horizontal and vertical directions, for the (horizontal) NOD and standard strain ε_1 uncertainty (adapted from Ref. [116]).

Test	Testing temperature	γ_{u_x} [cpx]	γ_{u_y} [cpx]	γ_{NOD} [cpx]	γ_{ε_1} [-]
MZ1-S1450G	room temperature	2	2	1.5	6.7×10^{-5}
MZ2-S1400	600℃	21	12	20	4.6×10^{-4}
MZ3-S1400G	600℃	19	11	23	4.8×10^{-4}
MZ4-S1450	600℃	18	9	22	4.5×10^{-4}
MZ5-S1450G	600℃	21	14	25	6.2×10^{-4}

Experiment in the F900 setup

Most of the height of the sample was visible in the F900 setup, especially the crack propagation region and almost the entire load application area. However, each side was illuminated by four blue LEDs, which could not fully illuminate the monitored surface. Therefore, it was chosen to focus two of the lights on each CMOD measurement region, and the other two where the crack would propagate. With this strategy, it was possible to have a better illumination in the region highlighted by red contours, where a first mesh with the parameters gathered in Table 3.6 was constructed. This first mesh was used to check the overall displacement uncertainty and to study crack propagation and its path on both surfaces. Two additional analyses were performed in which the mesh consisted of four noded squares (divided into two triangles) in the CMOD and in the NOD regions (Figure 3.19). It is worth noting that half of the region used for the CMOD calculation was located in darker zones, which affect the displacement uncertainties.

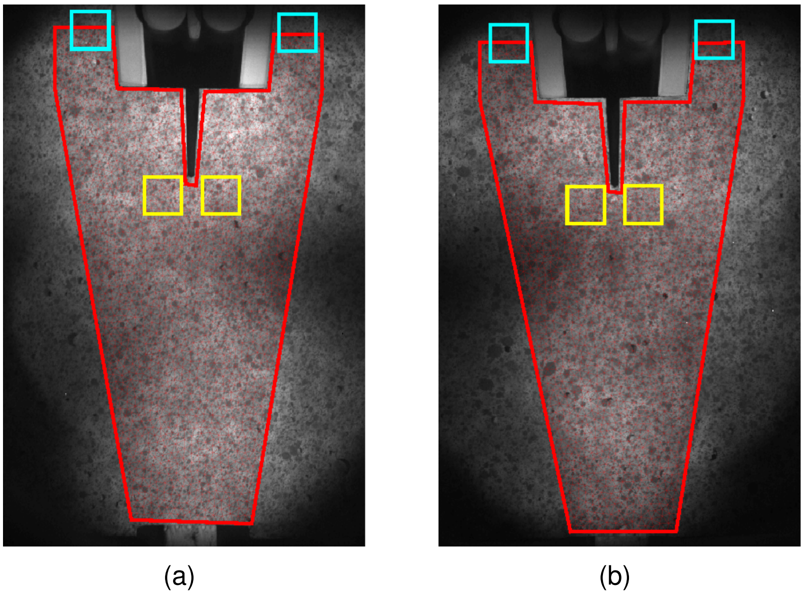
(a)

(b)

Figure 3.19: Three sets of meshes used for analyzing the test performed at 900 ℃ for the (a) front and (b) back faces of the specimen. The red contours depict the mesh used for analyzing the more illuminated region in both sides. Regions used to calculate the CMOD and NOD are depicted in cyan and yellow boxes, respectively.

It is worth noting that the displacement noise floor of the test performed at 900 ℃ is slightly lower than those observed at 600 ℃ (see Table 3.5). At this higher temperature, radiations play a bigger role in the heating of the sample, which may homogenize the temperature field inside the furnace, and therefore the heat haze may affect less the acquired images. This phenomenon could also be related to the contrast and illumination of the samples. However, it is more likely that this trend is directly related to the exposure time used in both situations. At 600 ℃, an exposure time of 1/50 s was used, while 2 s were used at 900 ℃

with the utilization of neutral density filters. Higher integration times correspond to temporal averages, which mitigate heat haze effects [130].

Table 3.6: DIC analysis parameters for specimen MZ6-S1450 tested in the F900 setup.

DIC software	Correli 3.2
Image filtering	none
Color channel	blue
Element length	80 px
Shape functions	linear (T3)
Meshes	see Figure 3.19
Matching criterion	penalized sum of squared differences
Interpolant	cubic
Displacement noise-floor	0.09 px

In-situ experiments

For the WSTs performed *in-situ*, scans were acquired instead of images. Therefore, adaptations of the mesh and procedures were necessary. For instance, while triangular T3 meshes were used in 2D-DIC, for the 3D cases, T4 meshes were used (tetrahedra with four nodes). Two ortoghonal slices of the volume acquired for sample MZC1-S1450G are shown in Figure 3.20(a,b) with the contour of the first coarse mesh that was used for DVC purposes. Its positioning was finely made using a backtrack procedure [131]. A fake binary volume perfectly located at the nominal mesh location is constructed, with the internal value being the average gray value of the sample and the external of the air (around 150 and 0 gray levels, respectively, see Figure 3.20(a,b)). This fake volume is then correlated with the reference volume to reposition the mesh using a DVC procedure using an auxiliary mesh that encompasses the whole sample. Then, the same correction is applied to the fine mesh, resulting in a fine positioning (Figure 3.20(a,b)).

The resulting opening displacement field for the scan of the most loaded state (in displacement) is shown in Figure 3.20(c) with a maximum amplitude of the order of 10 vx in the region where the load is applied. However, considerably smaller displacements occurred in the crack path region, showing the difficulty of such analyses. This DVC calculation also results in gray level residual, which in

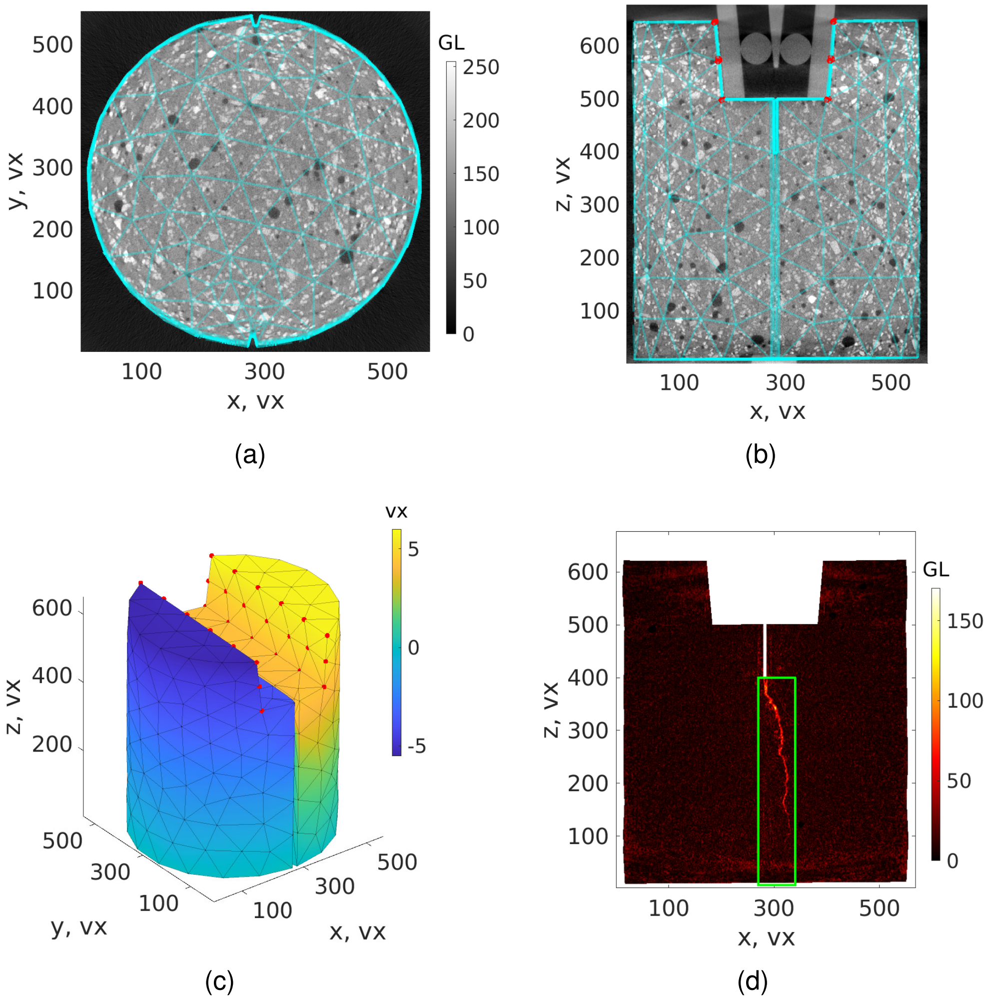

(a) (b)

(c) (d)

Figure 3.20: Coarse mesh shown in (a) $x-y$ and (b) $x-z$ planes for the reference configuration of MZC1-S1450G sample. (c) Measured displacement field (expressed in vx) in the x-direction for the most loaded state. (d) $x-z$ section of the resulting DVC residuals. The color bar in sub-figures (a,b) encodes the material attenuation to X-rays, the displacement in the x-direction in sub-figure (c), and the absolute gray level of the voxel-wise DVC residual in sub-figure (d). The red circles depict the nodes considered as Dirichlet entities in the mechanical regularization scheme. The green box highlights the area where the gray level residuals were calculated to probe the trustworthiness of the two considered crack paths (adapted from Ref. [124]).

this case, under the assumption of displacement continuity, beautifully highlight the crack surface. A frontal view of the residual volume in the middle of the sample (Figure 3.20(d)) shows the crack, although defining its end requires a user defined criterion.

Finer meshes (Figure 3.21) were also used. They were made to have duplicated nodes suitable for using cohesive elements in the crack path. Starting from a mesh with a straight crack path (Figure 3.21(a)), a second mesh (Figure 3.21(b)) was created by adapting the crack path to the real 3D crack path, whose slice is illustrated in Figure 3.20(d). First, the nodal x-coordinates of the straight crack path surface were fitted to the location of the maximum absolute voxel-wise residual, after penalizing maximum residuals located too far from the cracked region to mitigate noise effects. Then, the mesh was deformed with care to not change the external surfaces.

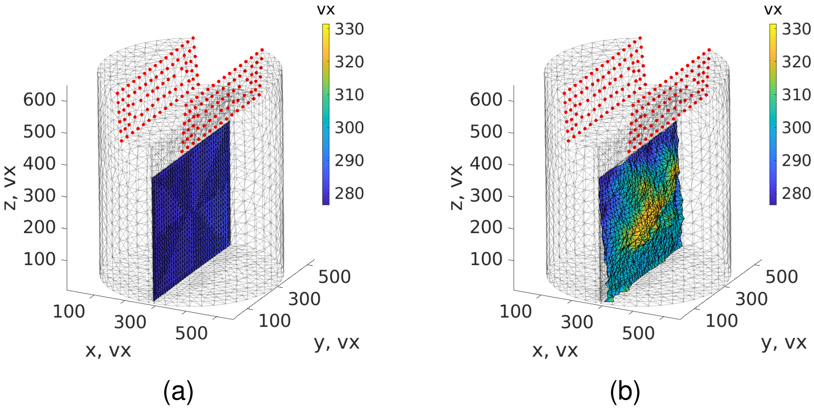

Figure 3.21: Elements on the surface of the finer meshes used in DVC analyses to measure crack opening displacements and in FE simulations to define cohesive elements. Crack path on a perfect plane (a) or adapted to the cracked surface (b). The color bar encodes the node position in the x-direction. The red circles depict Dirichlet nodes in the mechanical regularization scheme and as boundary conditions in FE simulations (adapted from Ref. [124]).

Last, the red dots on the DVC meshes (Figures 3.20(b,c) and 3.21(a,b)) depict where the boundary conditions are applied. The very same procedure introduced in this section exemplified with sample MZC1-S1450G was also performed for MZC2-S1450G sample. For the DVC analyses, two scans in the reference configuration were acquired to assess the displacement uncertainties. All the DVC parameters are shown in Table 3.7.

3.4.2 Finite Element models

This section introduces all the considerations for the numerical simulations performed in Abaqus in this thesis.

Table 3.7: DVC analysis parameters

DVC software	Correli 3.0 [129]
Image filtering	none
Element length (mean)	27 and 18 vx
Shape functions	linear (T4 elements) [132]
Meshes	see Figures 3.20 and 3.21
Matching criterion	penalized sum of squared differences
Convergence criterion	RMS of nodal displacement correction $\leq 10^{-4}$ vx
Regularization length	$\ell_{reg} = 10$ vx
Interpolant	cubic
Displacement noise floor	1 and 3 cvx

Cohesive zone model

The so-called PPR cohesive model [101, 103, 133] is used herein with zero-thickness elements. For the 2D models, they use four-node quadrilateral elements collapsed into two lines (one at each crack side), while for the 3D situations, six-node prisms collapsed into two triangles (one at each side of the crack). Although this cohesive law allows mixed-mode fracture to be modeled, the nature of the WST makes the sensitivity of mode I parameters predominant, and thus, all parameters for the other modes are considered to be equal to their mode I counterparts. Among the required parameters, the initial stiffness parameter is kept constant and equal to 0.005 [70]. Two fracture parameters to be calibrated in the identification procedure are shown in Figure 3.22. The cohesive strength σ_f defines the maximum stress. The fracture energy J_c corresponds to the area of the traction-separation curve. The curve shown in Figure 3.22 uses the initial parameters that are selected for the 600 °C analyses (see Table 3.8). Moreover, the shape parameter $\alpha = 7$ is used, providing an exponential decay (Figure 3.22). This choice is motivated by the investigations of Ref. [117]. Comparing this choice with a bi-linear traction-separation law (*i.e.,* with $\alpha = 2$) proved that the former is more suitable for the cases studied herein. Thus, $\alpha = 7$ will be used in the discussions from here on.

Boundary conditions corrections

In all discussed WSTs, the reference state image (or volume) was acquired with a small load to accommodate the loading parts. The kinematics from the

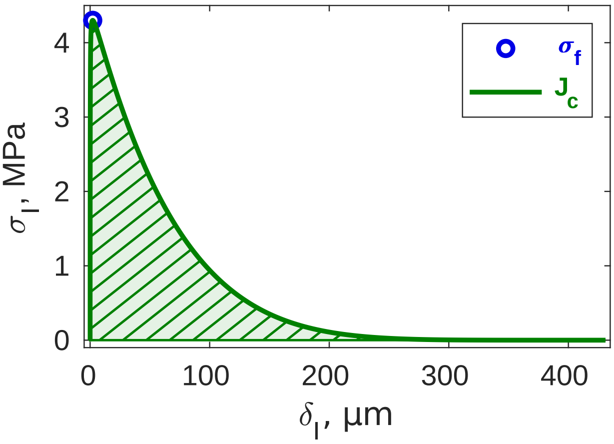

Figure 3.22: Mode I traction-separation law using the initial parameters of the PPR model used in the 600℃ case. An exponential decay is considered by using the shape parameter $\alpha = 7$. The cohesive strength σ_f corresponds to the maximum traction (blue circle). The fracture energy J_c is the integral of the traction-separation curve (green dashed area). Adapted from Ref. [117].

unloaded to this pre-loaded state is unknown. One parameter that will be called Boundary Condition correction (BCc) [70] is calibrated together with the fracture parameters to compensate for this effect in the numerical simulations. It is defined by a scalar and a boundary condition displacement from a user-defined time step, which should be taken when measured displacements are greater than their uncertainty and no or very little damage has taken place. For the studied cases, the closest time step to the load about 50% of the ultimate load (before it is reached) is considered. BCc is then defined as the fraction of this displacement that is needed to correct the loading curve in the calibration procedure plus one. Choosing to initialize BCc=1 is usual since it indicates that no correction is needed. To exemplify, if BCc=1.15 after calibration, it indicates that 15% of the chosen time step displacement is used to approximate the unknown displacement, and is added in the boundary conditions for all time steps in the numerical simulation. Last, if the calibration results into a BCc<1, a (horizontal) closing of the CMOD correction is needed.

WST in the F600 setup

All the five samples analyzed in the F600 setup, and the one in the F900 setup, were investigated using the mesh shown in Figure 3.23, properly positioned for each sample considering their reference image. A plane strain hypothesis is considered due to the non-negligible out-of-plane dimension of the sample. Zero thickness cohesive elements of about 200 µm are depicted in red, with the nodes highlighted in red dots in Figure 3.23(b). CPE4 elements are used around the cohesive elements to define the region where the thickness is reduced (for the grooved samples). Compatible CPE3 elements are used close to the cohesive elements, with a size gradient as one moves away from them, going up to ≈ 5 mm in length in regions where fine discretization is not needed. Boundary conditions from images gathered down to 15% of the peak load were used. For the room temperature case, NODs measured from the cyan boxes shown in Figure 3.23(a) are extrapolated to the nodes highlighted by green dots (at the mid-height of the regions where the force is applied), by using the methodology described in Section 3.2.1, and then applied as Dirichlet boundary conditions.

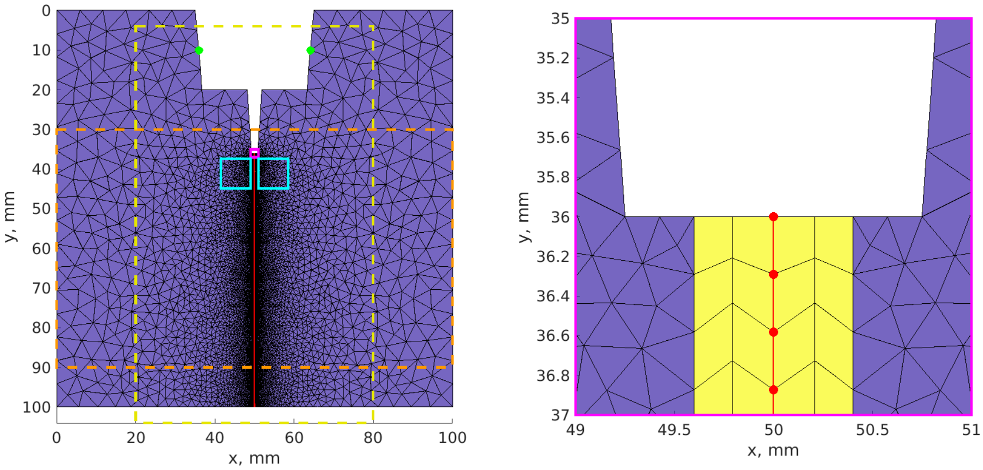

(a)

(b)

Figure 3.23: (a) Mesh for the finite element analyses of the data gathered in the F600 and F900 setup. The NOD region is depicted as cyan squares, and the two nodes where the boundary conditions were applied as green circles. One line of zero thickness cohesive elements was used in the crack propagation region and is shown as a red line. The (approximately) available field of view for the F600 and F900 are depicted as the dashed orange and yellow boxes, respectively. (b) Zoom about the pre-notch (small magenta box in sub-figure (a)). CPE3 elements are shown in blue and CPE4 elements in yellow. The red circles highlight the duplicated nodes used in the PPR cohesive elements (adapted from Ref. [117]).

For the tests performed at 600 ℃ (samples MZ2-S1400 to MZ5-S1450G), with uncertainties about one order of magnitude higher, large oscillations occurred if NODs were used directly. Therefore, their high frequency oscillations were first filtered out by using the so-called Hermite splines [134], with four degrees of freedom that comprises the function value and its derivative at both ends of given interval. Figure 3.24 exemplifies this filtering for sample MZ2-S1400 using a total of 20 degrees of freedom once continuity of the function and its derivative was enforced in nine intervals. The filtering was done by a least squares minimization between the raw NODs and the aforementioned interpolation function. It is worth noting that the standard deviation of the difference between the filtered and the raw NOD shown in Figure 3.24 is equal to 1.6 times the corresponding measurement uncertainty, and was always less than twice its value for all the analyzed experiments. For the 600℃ cases, the filtered NOD was then extrapolated to CMOD and applied as Dirichlet boundary conditions.

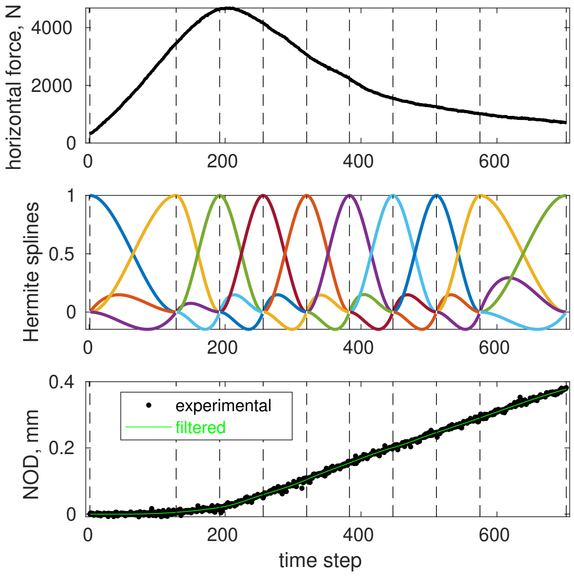

Figure 3.24: Experimental horizontal force (test MZ2-S1400), Hermite splines, experimental and filtered NODs as functions of time steps. The vertical dashed lines depict the ten points of interest used to define the splines.

An isotropic and linear elastic behavior is considered in all elements apart from the cohesive elements. The Young's modulus is equal to 46 GPa, as identified at room temperature using sample MZ1-S1450G [122], and is kept constant since its sensitivity was already low, and leading to unrealistic levels if calibrated at 600℃ with higher uncertainties. A total of five parameters are calibrated together using the FEMU-F-NOD procedure. Two of them are the cohesive strength σ_f and fracture energy J_c. The other three are related to the boundary conditions, with R and c defining the extrapolation (see Section 3.2.1) and BCc the correction to account for the kinematics related to pre-loading at the reference state (Section 3.4.2). Their initial values in the procedure, based in Ref. [122], are given in Table 3.8

Table 3.8: Initial parameters for FEMU-F-NOD for the 600℃ tests (adapted from Ref. [117]).

Parameter	Description	Initialization
σ_f [MPa]	Cohesive strength	4.3
J_c [J/m^2]	Fracture energy	280
R [-]	NOD/CMOD ratio at ultimate load	2.2
c [-]	Post-peak NOD vs. CMOD affine slope	1.5
BCc [-]	Boundary condition correction	1

WST in the F900 setup

For specimen MZ6-S1450 tested at 900℃, the very same mesh discussed in Figure 3.23 was used with a smaller height (of 1.5 mm) to better describe the experimental geometry. It was positioned to best fit the sample in the reference images for both opposite sides independently, as shown in Figure 3.25, where the CMOD and NOD measurement regions are also displayed. The required mesh rotation for adapting to the images was $-1.2°$ and 0.8°, respectively. Contrary to the 600℃ setup, it was possible to directly measure the CMOD, and therefore it was used to prescribe boundary conditions without having to extrapolate the NOD and using splines for filtering. FEMU-F was used for the calibration of parameters, as performed in Ref. [70], with the addition of the Young's modulus in the cost function as will be shown hereafter.

The parameters of interest were initialized from the converged set of the identification of MZ4-S1450 specimen (Table 4.4) since it was the closest considering sintering and testing temperatures, and had no lateral grooves. First, a FEMU-F calibration without the Young's modulus was performed, and the resulting parameters were then used to initialize the next case with the added Young's modulus,

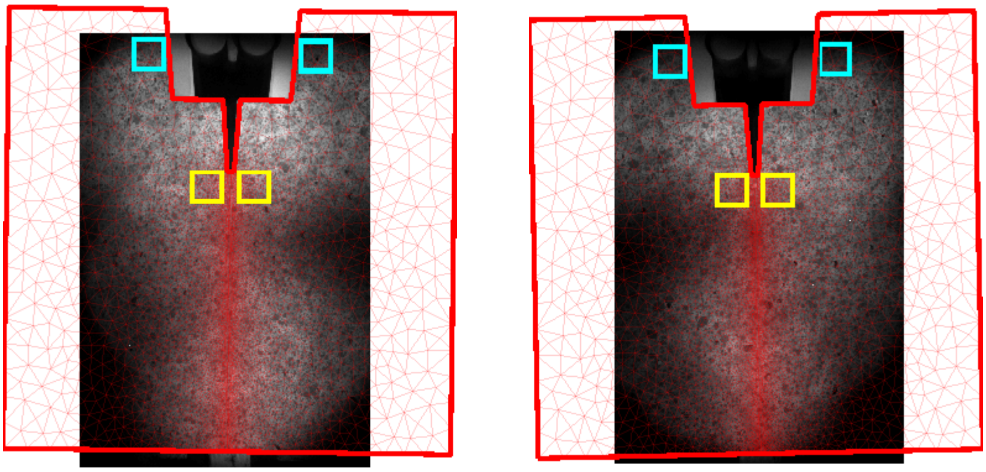

(a) (b)

Figure 3.25: Mesh from Figure 3.23 (in red) positioned in the reference images of the test performed at 900 ℃ for the (a) front and (b) back surfaces of the specimen. The regions used for calculating the CMOD and NOD are shown in cyan and yellow, respectively. For the sake of comparison, a similar disposition is shown in Figure 3.4(a) for the 600 ℃ setup.

initialized with the value used for the specimens tested in the 600 ℃ setup.

In-situ WSTs

Displacement fields measured using the coarse mesh (Figure 3.20) were first interpolated for the nodes of finer meshes (Figure 3.21) to mitigate the influence of measurement uncertainties. Then, nodal displacements in both surfaces where forces were applied (see red dots in Figure 3.21) were prescribed as boundary conditions. For sample MZC1-S1450G, the last three scans were not used since the model could not properly account for that high level of damage. Thus, data from twelve scans (two in the reference state) with data up to scan #10 were employed, which corresponds to a (post-peak) force of the order of 20% of the ultimate load. A temporal enrichment was made by adding four more points linearly interpolated between DVC data, totaling 51 time steps in the numerical simulation. In other words, from the 51 time steps in the simulations, 11 had the boundary conditions directly measured via DVC while the other 40 were linearly interpolated. Additionally, the forces calculated in these 51 simulation steps were linearly interpolated into 11,368 points, the same number of force data acquired by the testing machine, in order to fully employ the gathered data in the minimization procedure.

Both meshes shown in Figure 3.21 are used in the investigation. Apart from the cohesive elements, C3D4 elements are used in the remainder of the sample with an isotropic and linear elastic behavior. FEMU-F was used after checking that no great benefits would come from coupling the other available measurements in the calibration procedure [124]. Four parameters are calibrated in this case, initialized with the values of Table 3.4, namely, the Young's modulus E (after Ref. [122], the cohesive parameters σ_f and J_c (after Ref. [117]), and the BCc as previously discussed (Section 3.4.2).

Table 3.9: Initial parameters for the FEMU-F analyses of the MZC1-S1450G sample. Adapted from Ref. [124].

Parameter	Description	Initial value
E [GPa]	Young's modulus	46
σ_f [MPa]	Cohesive strength	4.3
J_c [J/m^2]	Fracture energy	270
BCc	Boundary condition correction	1

4 RESULTS AND DISCUSSION

4.1 Tests performed in the F600 setup

4.1.1 Crack paths

From the five samples analyzed in the F600 setup, three samples had lateral grooves that guided the crack, and no surface cracks were visible out of the imaged grooves. For samples MZ2-S1400 and MZ4-S1400 however, the crack path being not driven by such grooves, multiple branching may occur [135], and thus, the resulting crack path needs to be further analyzed. Maximum principal strain fields were investigated and are shown for both specimens in Figure 4.1 at 50% of the ultimate load (post-peak). The ROI was reduced to focus on the crack path, and smaller elements (9 px in length) were used to refine the fields. For sample MZ2-S1400 (Figure 4.1(a)), the crack exhibited no branches and was slightly tilted, yet propagated very closely to the center of the specimen, while a bifurcation was seen for sample MZ4-S1450, which propagated a little farther away from the middle plane.

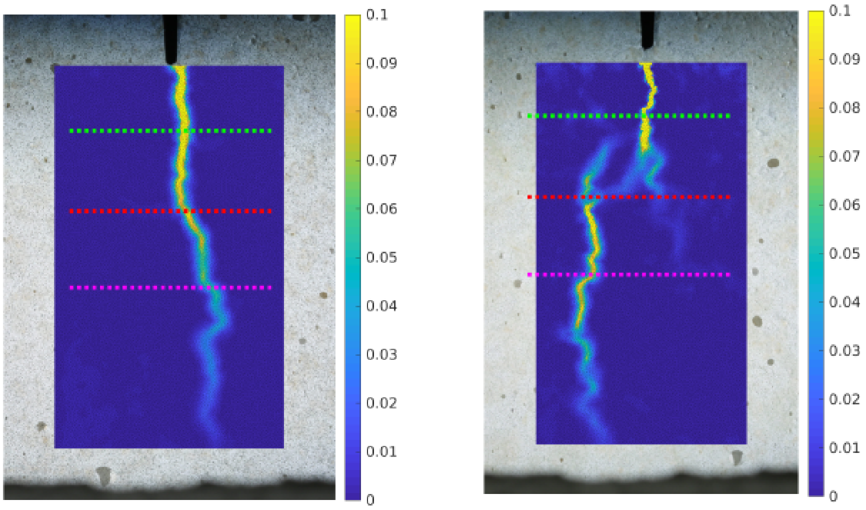

(a) (b)

Figure 4.1: Maximum principal strain fields for 50% of maximum load (post-peak regime) for samples (a) MZ2-S1400 and (b) MZ4-S1450. The red dashed line depicts the section of the tomographic scan analyzed in Figure 4.2. The three horizontal segments depict the width and location of the sections shown in Figure 4.3 (adapted from Ref. [116]).

Both samples were scanned *post-mortem* in the same tomograph used for the

DVC analysis in order to check the crack path. The vertical slices of the bulk data from the reconstructed volume at the height of the red dashed lines in Figure 4.1 are shown in Figure 4.2(a,c) with the highlighted cracks in sub-figures (b,d). Such images indicate that one single macrocrack propagated in the bulk for both cases, while the branch remained very close to the surface of specimen MZ4-S1450.

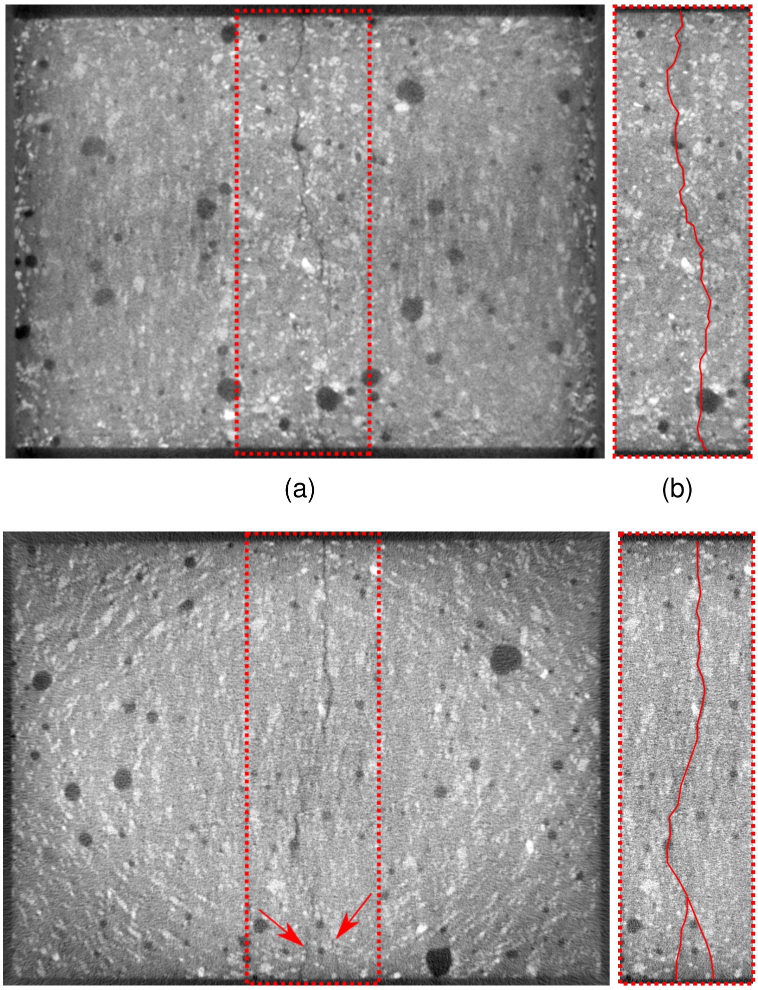

(a) (b)

(c) (d)

Figure 4.2: Slices of the reconstructed volumes of samples (a) MZ2-S1400 and (c) MZ4-S1450 imaged post-mortem via tomography (see dashed red lines in Figure 4.1). One single macrocrack is observed in the bulk for both cases, with sample MZ4-S1450 having a branched crack close to its surface (red arrows). The cracks are highlighted in sub-figures (b) and (d), adapted from Ref. [116].

Figure 4.3 represents a similar analysis for the other heights shown as dashed lines in Figure 4.1. For sample MZ2-S1400, the crack propagated closer to the central plane in the opposite side (not visible through the window), since they appear closer to the center of the dashed boxes in Figures 4.3(a-c). For specimen MZ4-S1450, the macrocrack in the other two slices (Figures 4.3(d,f) appears even straighter.

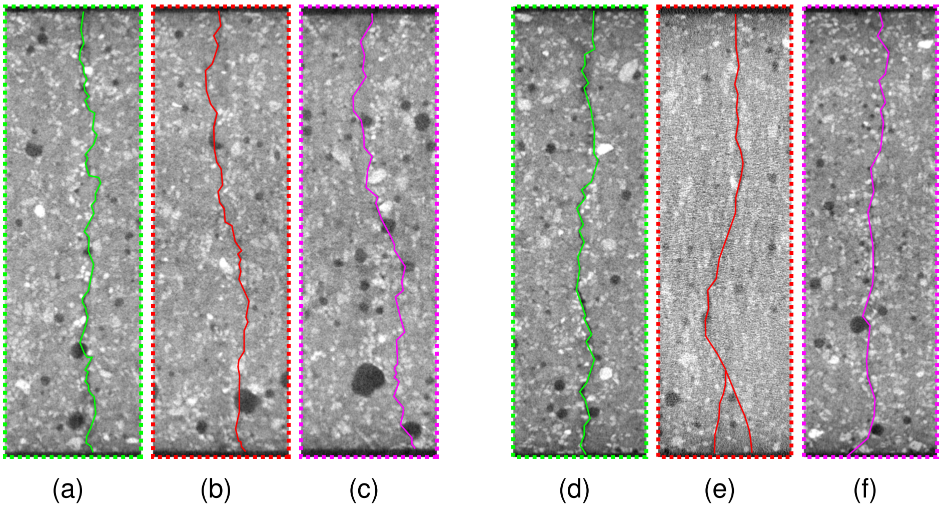
(a) (b) (c) (d) (e) (f)

Figure 4.3: Three horizontal slices of samples MZ2-S1400 (a-c) and of MZ4-S1450 (d-f) (see dashed lines in Figure 4.1). They are positioned (a,d) closer to the notch, (b,e) in the branching region, and (c,f) below the latter. The surface shown in Figure 4.1 corresponds to the bottom line of the slices

These *post-mortem* tomographic results highlight the importance of volume data and bulk measurements. They also illustrate how one may be misled by surface observations alone, for instance, analyzing surface branching when essentially one dominant crack was created. Moreover, they reinforce the hypothesis of one single macrocrack propagating in the central plane, which was made in the FE models of all 2D FEMU analyzes performed in this thesis.

4.1.2 Sensitivity analysis

Before proceeding to FEMU calibration, a sensitivity analysis was performed to be sure that the parametrization was well adapted, following the guidelines discussed in Section 2.8. Sample MZ1-S1450G is chosen to illustrate this analysis, but very similar results arise from the other samples. Part of the results presented in this section were first reported in Ref. [122], where the whole set of 584 images was compared to cases using only one in ten or one in fifty images. Such analysis showed that uncertainties decreased the more images were available, but also that few images were required for trustworthy results. For instance, identical sensitivity trends were qualitatively seen when only twelve (equally spaced) images of the data-set were used. For the sake of conciseness, only the case using every image is discussed herein. FEMU calibration took two hours per iteration and converged in three iterations, when initialized with the resulting parameters of the case considering one in ten images, which, itself, took seven iterations of fifteen minutes each.

The sensitivity curves using the parameters after convergence are shown in Figure 4.4, when normalized by their respective uncertainties. It is worth noting that qualitatively similar curves were also obtained for the DD40 material (used for the NOD extrapolation discussed in Section 3.2.1) and for samples with no lateral grooves [122], and it is thus believed to be strongly related to the WST setup. As an example, force sensitivities of J_c and c parameters are alike post-peak (when multiplied by a factor of minus one), but they can be better distinguished when their very different NOD sensitivities are also considered. All the chosen parameters showed sensitivities several times above the uncertainty (*i.e.,* with SNRs > 1) for several time steps, further highlighting their likely calibration.

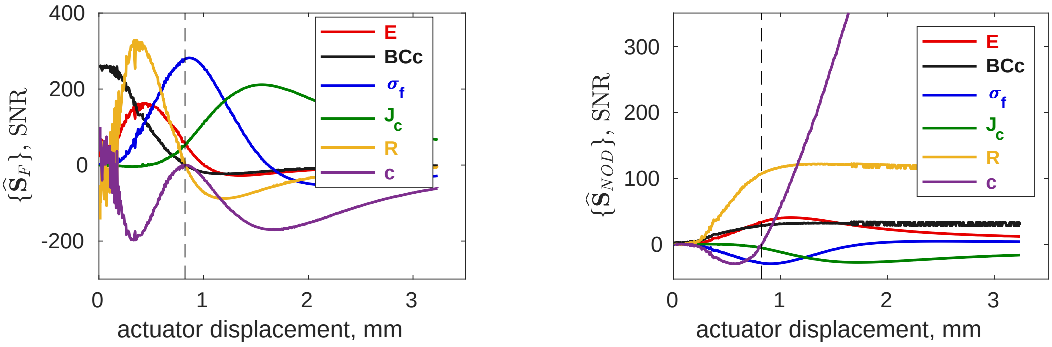

(a) (b)

Figure 4.4: Parameter sensitivities of (a) splitting force $\{\mathbf{S_F}\}$ and (b) NOD $\{\mathbf{S_{NOD}}\}$ using the whole (584) image set of sample MZ1-S1450G, normalized by their respective uncertainty (represented as signal-to-noise ratios). The vertical dashed line depicts the ultimate load instant (adapted from Ref. [122]).

From the sensitivity matrices, the Hessian matrix for FEMU-F-NOD applied to all test cases performed in the F600 setup is expressed as

$$[\mathbf{H}] = [\mathbf{S}_F]^\top [\mathbf{S}_F] + [\mathbf{S}_{\text{NOD}}]^\top [\mathbf{S}_{\text{NOD}}] \tag{4.1}$$

where the elements of the $[S_{\text{NOD}}]$ and $[S_F]$ matrices are shown in Figure 4.4. The corresponding Hessian matrix is displayed in Figure 4.5(a) when normalized by the number of used time steps such that it can be interpreted as average changes in squared SNRs. Its diagonalization, *i.e.,* its eigenvalues and vectors, is respectively presented in Figure 4.5(b,c). Each column in Figure 4.5(c) shows linear combinations of parameters associated with each eigenparameter (eigenvector), with the ones on the left with the highest sensitivity and on the right those with the smallest ones. From this trend alone, it is visible that the Young's modulus is the least sensitive parameter while c is the most sensitive, since they are highly predominant in the first and last eigenparameter, respectively. Moreover, the eigenvalues span over three orders of magnitude, but, if E is removed from the calibration, this ratio is reduced by at least one order of magnitude. After c, the R parameter is the second most sensitive, followed by the fracture parameters (σ_f and J_c) being correlated in the third and fourth eigenparameter, the BCc being dominant in the second and last the Young's modulus E.

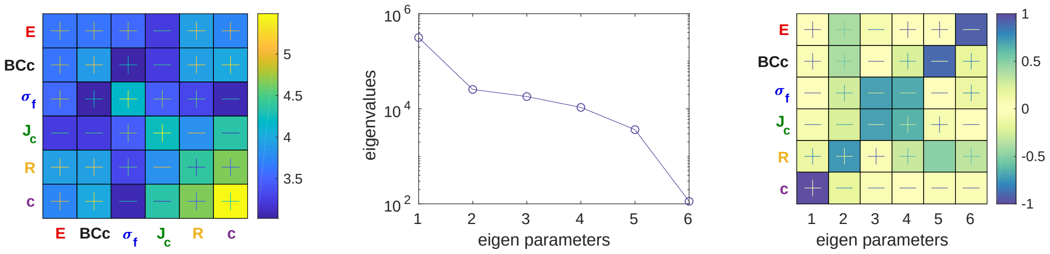

(a) (b) (c)

Figure 4.5: (a) Dimensionless Hessian normalized by the number of time steps and respective (b) diagonal and (c) eigen vector matrices. The first two matrices are shown in decimal logarithms. The components that may have negative values are shown with the signs represented on it (adapted from Ref. [122]).

After the aforementioned sensitivity analysis on the room temperature test, it became clear that the tenfold higher uncertainty in NOD for the 600 °C experiments would lead to unreliable values of E, and therefore, it is removed from the following analysis. A value of 46 GPa, as obtained for this first calibration for sample MZ1-S1450G, is used for all the samples. FEMU-F-NOD calibration of the five remaining parameters is then performed in all five experiments [117]. Time steps were truncated at 15% of the ultimate force of the test, since the numerical model did not well describe the very end of crack propagation.

Last, before proceeding to the calibration results, Figure 4.6 gathers the eigenvalues for the five eigenparameters (or eigenvectors) of the decoupled Hessians (*i.e.,* considering force or NOD data only), ranked in decreasing power order for the three grooved samples, MZ1-S1450G, MZ3-S1400G, and MZ5-S1450G. The ratio between the last and the first eigenvalues is directly the conditioning of the system; the smaller, the better for the calibration procedure. It is interesting to notice a rapid decay when calculated only with NOD data, meaning that force measurements are required for calibrating such parameters. Even if the eigenvalues when forces data alone are considered are quite stable, the last one is two to three orders of magnitude smaller than the others. This weaker eigenparameter for the force is mainly a combination of c and J_c parameters for the three studied samples, whose distinction could not be made if force data alone were used.

The previous trend is even worse for the 600℃ tests, where one eigenvalue tends to unity, meaning an average sensitivity of the order of the force uncertainty. For the sake of illustration, the weakest eigenparameters of the NOD data (which are very close to unity) are mainly based on BCc for the MZ1-S1450G, and a combination of J_c and σ_f for the others. However, when NOD and force data are coupled, all the eigenvalues shows a flat tendency, indicating a better conditioning of the system. This result shows the importance of performing the sensitivity analysis and coupling different quantities in the calibration, in order to allow proper calibration of all the sought parameters.

4.1.3 Room temperature experiment

Experimental and numerical NOD and splitting force as functions of the actuator displacement for sample MZ1-S1450G (the only experiment performed at room temperature in the F600 setup) are shown in Figure 4.7 after calibration considering five parameters (*i.e.,* with fixed Young's modulus). Both NOD curves are almost indistinguishable (Figure 4.7(a)), with $\chi_{NOD} = 3.8$, meaning an average difference between experimental and simulated NODs of the order of 1 µm (or 6 cpx). For the forces, $\chi_F = 6.6$ is obtained, *i.e.,* about 66 N in average (for

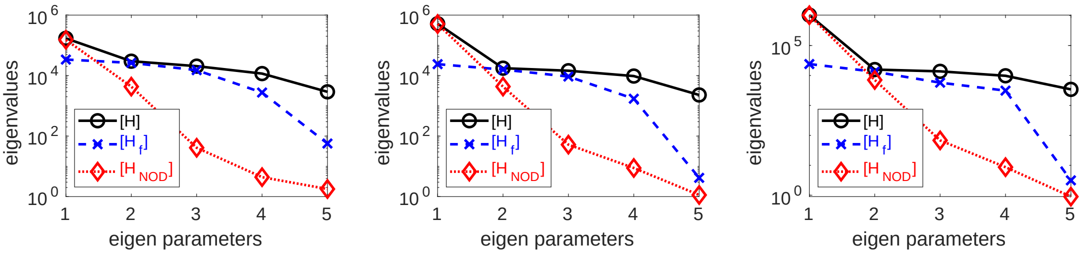

(a) (b) (c)

Figure 4.6: Eigenvalues for the five eigenparameters (or eigenvectors) of the diagonalization of the FEMU-F-NOD Hessian matrix and its decoupled counterparts, namely, Hessian matrices only considering force or NOD data, for samples (a) MZ1-S1450G, (b) MZ3-S1400G, and (c) MZ5-S1450G.

a maximum force of the order of 4000 N), with the numerical and experimental curves shown in Figure 4.7(b). The highest deviation arises in the very beginning of the test, due to very low displacements and the accommodation of the loading setup. Difference from the experimental peak load and that simulated is less than 2%. Globally, both NOD and force histories are well captured with a global $\chi = 5.2$, meaning that on average the numerical quantities were different from their experimental counterparts by five times their uncertainties.

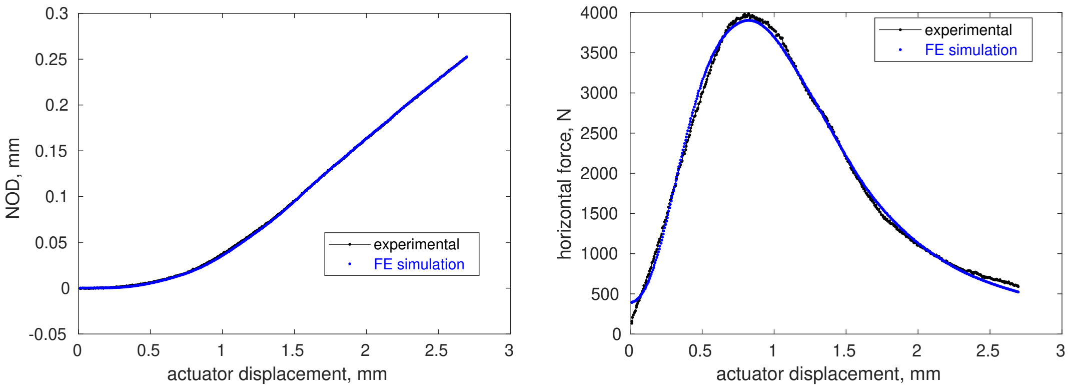

(a) (b)

Figure 4.7: Experimental and simulated force (a) and NOD (b) vs. actuator displacement for test MZ1-S1450G, performed at room temperature in the F600 setup (adapted from Ref. [117]).

As a further confirmation, the simulated displacements after calibration (also using the Young's modulus E, as reported in Ref. [122]) were compared to the experimental fields of the whole visible sample surface (see cyan ROI in Figure 3.16(a)). Rigid body motions were also allowed to ensure that the positioning was not giving rise to higher residuals. This comparison is shown in Figure 4.8(a) when normalized by the displacement uncertainty. The groove region was not accounted for due to poor contrast. Their RMS difference is on average 16 times the standard uncertainty (*i.e.,* 6 µm or 0.32 px). The rising trend is explained by crack initiation and propagation together with any displacements that the numerical model could not capture (*e.g.,* some small out of plane motions due to small rotations). Moreover, the gray level residuals were also independently measured using both displacement fields, resulting in the curves shown in Figure 4.8(b), with a difference less than 1% of the dynamic range. These two kinematic verifications provide further evidence that the applied procedure was well adapted to this case.

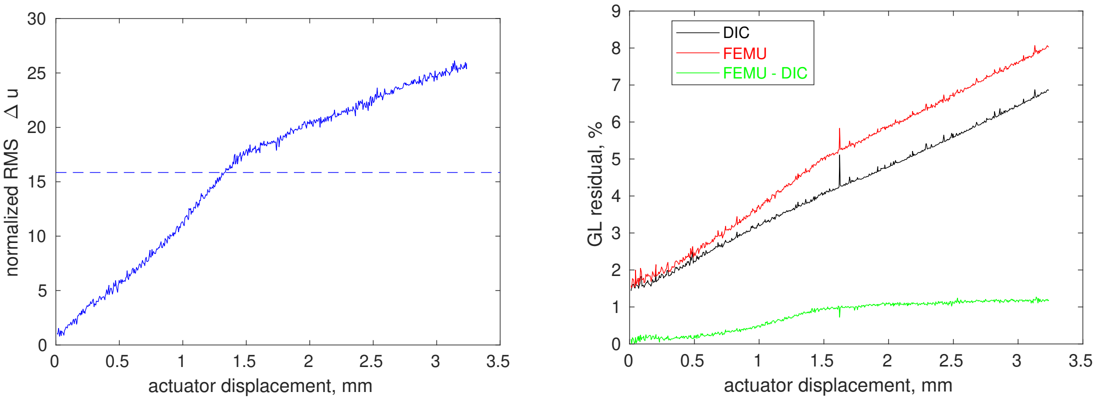

(a)

(b)

Figure 4.8: (a) Instantaneous RMS residual between FEMU and DIC measured displacement fields, whose average is represented by the dashed blue line. (b) Corresponding gray level residuals (adapted from Ref. [122]).

4.1.4 NODs for experiments performed at 600 °C

All the cost functions χ_{NOD} for the experiments performed at 600 °C are reported in Table 4.1, and the respective curves are displayed in Figure 4.9. It is worth noting that these NODs were filtered before extrapolation, with differences from the raw measurements always less than twice their standard uncertainty. To compute χ_{NOD}, the resulting NODs from the numerical simulation are compared to the raw NOD measurements. The very small values of χ_{NOD} of the order of the filtering error of twice the uncertainties confirms that the simulated kinematics in this region was trustworthy for all the experiments. Apart from sample MZ3-S1400G, all χ_{NOD} are less than those reported for the room temperature test (MZ1-S1450G), which is due to its standard uncertainty (which χ_{NOD} uses) that is one order of magnitude lower.

Table 4.1: NOD cost functions for the 600℃ tests (adapted from Ref. [117]).

Test	MZ2-S1400	MZ3-S1400G	MZ4-S1450	MZ5-S1450G
χ_{NOD}	1.9	4.5	2.6	1.7

When comparing to the results for sample MZ1-S1450G (at room temperature), the higher uncertainty for the NODs when measured at higher temperature is seen in Figure 4.9. Test MZ3-S1400G is the one with the highest deviations, especially around the peak load, where the starting quadratic trend changes to an affine slope in the NOD vs. CMOD curve. A small deviation in the same region is also observed for sample MZ4-S1450, while for tests MZ2-S1400 and MZ5-S1450G the numerical simulation does not deviate from the experimental data.

4.1.5 Forces for experiments performed at 600℃

All cost functions χ_F calculated for samples tested at 600℃ are gathered in Table 4.2 and the respective curves given in Figure 4.10. Apart from sample MZ4-S1450, all the values are at least twice that of test MZ1-S1450G, which was expected since for the forces the experimental uncertainty was constant (*i.e.,* 10 N in horizontal force). The force errors were higher than the NOD data reported before (*i.e.,* , χ_F was higher than χ_{NOD}), which is believed to be partially due to the way boundary conditions were prescribed.

Table 4.2: Force cost functions for the tests conducted at 600℃ (adapted from Ref. [117]).

Test	MZ2-S1400	MZ3-S1400G	MZ4-S1450	MZ5-S1450G
χ_F	13.4	14.7	5.9	19.8

Small discontinuities are seen in the lase three experimental curves since they are envelopes of cyclic loading histories. The response of sample MZ2-S1400

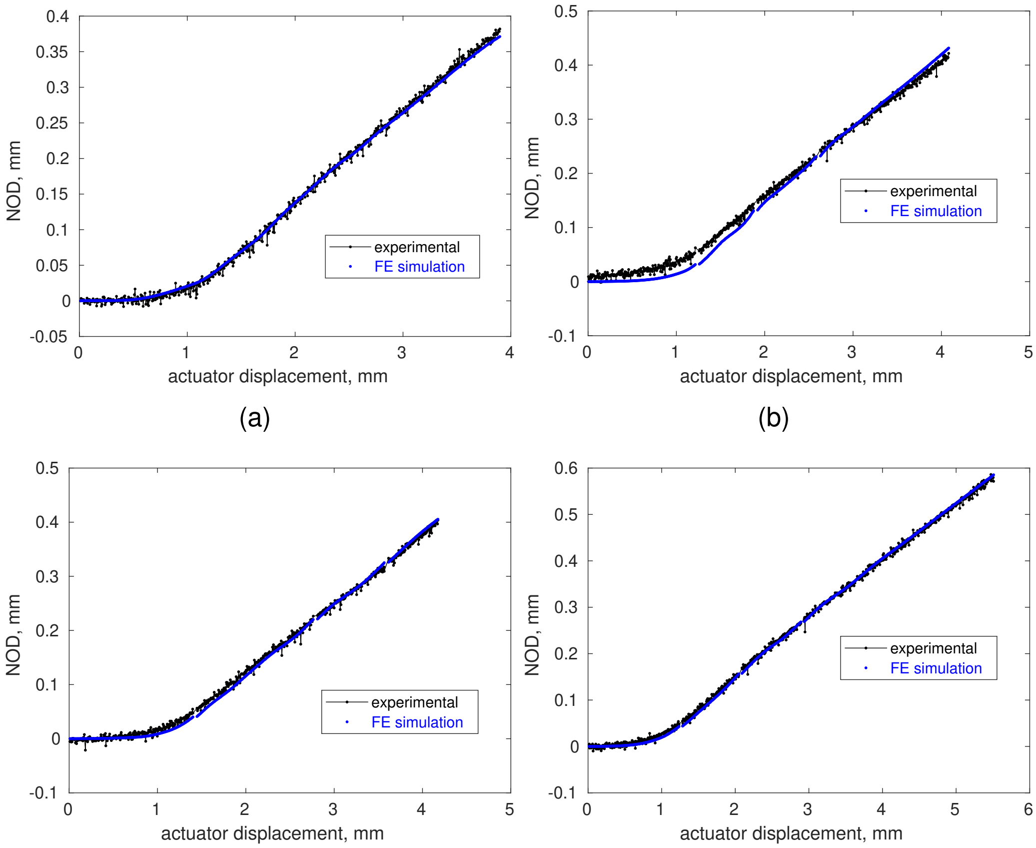

(a) (b) (c) (d)

Figure 4.9: Experimental and simulated NOD vs. actuator displacement for samples (a) MZ2-S1400, (b) MZ3-S1400G, (c) MZ4-S1450, and (d) MZ5-S1450G, performed at 600 °C in the F600 setup (adapted from Ref. [117]).

trend was well captured apart from the very beginning, which is not fully understood. The highest deviations arose for the grooved samples (MZ3-S1400G and MZ5-S1450G) in which probably a higher shape parameter for the cohesive zone model was required for having a longer tail on the exponential decay. However, even for these two “worst” cases, the beginning of the curve is very well captured, and the maximum load error is of the order of 10% of the experimental peak load.

4.1.6 Boundary condition parameters

All the parameters related to boundary conditions (*i.e.,* R, c, and BCc) are reported in Table 4.3. No trend can be inferred for the R parameter due to its high scatter ranging from 1.4 up to 2.4, more so when comparing to the values 2.3 and 2.7 obtained for the cases used in investigation of Section 3.2.1 about the

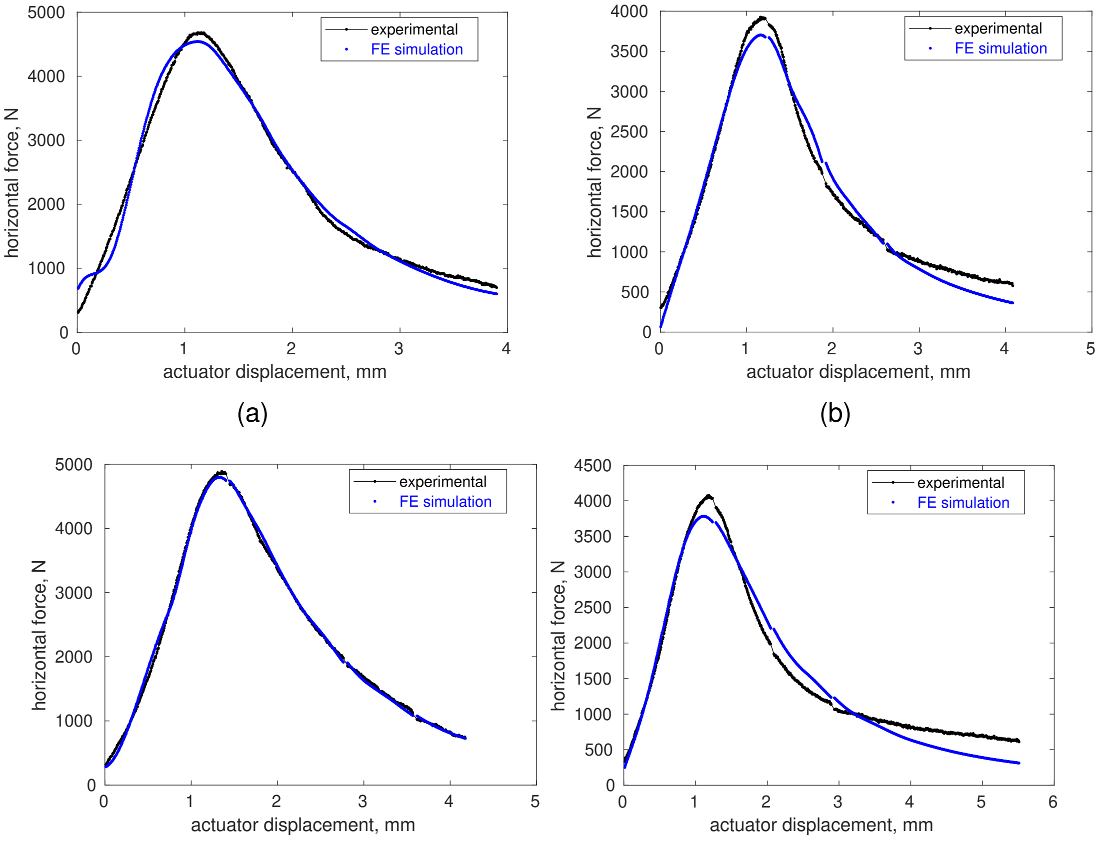

(a)

(b)

(c)

(d)

Figure 4.10: Experimental and simulated force vs. actuator displacement for samples (a) MZ2-S1400, (b) MZ3-S1400G, (c) MZ4-S1450, and (d) MZ5-S1450G, performed at 600℃ in the F600 setup. Adapted from Ref. [117].

NOD vs. CMOD relationship. Even if the c parameter varied less, only a range is given between 1.41 and 1.62, which also comprises the values 1.54 and 1.61 obtained for the DD40 samples and the 1.57 when considering brittle propagation in an FE analysis [118]. High scatter is also observed for the BCc parameter (*i.e.,* from 1.2 up to 2.2), even if its definition was similar in all cases. This fact may be due to misalignments of the wedge at the beginning of the test, which may result from sample heterogeneity that makes the crack to initiate on one side of the sample. Last, these results and variations highlight the interest in using full-field measurements such as DIC to measure boundary conditions with increased trustworthiness for numerical simulations. Another interest is to have information from both sides of the sample (which was not possible in the 600℃ setup) in order to mitigate possible effects of misalignment of the loading parts in the calibration results and to better understand this scatter [54].

Table 4.3: Converged parameter sets related to boundary conditions for FEMU-F-NOD calibration of the samples tested in the F600 setup (adapted from Ref. [117]).

	MZ1-S1450G	MZ2-S1400	MZ3-S1400G	MZ4-S1450	MZ5-S1450G
R	2.26	2.36	1.41	1.59	1.68
c	1.45	1.41	1.61	1.53	1.51
BCc	1.22	2.19	1.08	1.22	1.69

4.1.7 Material parameters

Both fracture-related parameters, σ_f and J_c, are gathered in Table 4.4 for the five studied samples. One first point of interest is the fact that all 600℃ experiments led to smaller cohesive strengths, which is explained by the smaller bonding energy with increases in temperature. Moreover, when measured at 600℃, the fracture energies were higher, which is related to different coefficients of thermal expansion between phases [29]. When comparing samples sintered at 1450℃ to those sintered at 1400℃ (*i.e.,* MZ4-S1450 to MZ2-S1400 and MZ5-S1450G to MZ3-S1400G), the former had higher fracture energies, which is related to stronger bonds between mullite zirconia aggregates and the alumina matrix [136], thus causing more interlocks and friction between aggregates during crack propagation. However, no significant changes in cohesive strength were seen, since the biggest defect remained the pre-notch.

Table 4.4: Converged parameter sets for identifications of the tests performed in the F600 setup (adapted from Ref. [117]).

	MZ1-S1450G	MZ2-S1400	MZ3-S1400G	MZ4-S1450	MZ5-S1450G
σ_f [MPa]	4.34	3.54	3.85	3.68	3.80
J_c [J/m^2]	266	327	361	405	456

Interesting differences are also seen on the effect of the lateral groove to guide the crack, whose presence increased both CZM parameters by about 10% when comparing samples MZ2-S1400 to MZ3-S1400G or MZ4-S1450 to MZ5-S1450G. This trend is explained by toughening mechanisms acting on crack propagation after its initiation, as described by the weakest link theory for brittle materials. For the samples with grooves, the weakest path is not necessarily followed by the crack [135]. Thus, it dissipates less energy [117], as seen in the fracture energy estimated from NOD data or from the raw vertical load vs. actuator displacement [116] for the very same experiments. However, an inversion of this trend is observed in the CZM fracture energy (*i.e.,* higher J_c for cases with grooves). One possible source of error in such assumptions is the straight crack path on the non-grooved case, but if the crack path was finely defined for these cases, the calibrated fracture energy is expected to be lower [71], further increasing the difference among the grooved and non-grooved cases. The highest values of χ_F for the grooved sample may indicate that some improvements in the FE model are still required to better describe experiments with grooves, which could shed light on these differences in fracture energies.

The fractured surfaces of samples MZ3-S1400G and MZ5-S1450G were investigated to better understand the increase in fracture energy with the highest sintering temperature. They were imaged in an SEM under backscattered electron mode, with the polarity inverted for one of the four detectors to improve topographic perception. Mullite-zirconia aggregates (cyan dotted contours in Figure 4.11) were considerably flatter in sample MZ3-S1400G (Figure 4.11(a)) when compared to MZ5-S1450G (Figure 4.11(b)). The dotted pattern on the cyan contour at the top of Figure 4.11(a) indicates a flat fracture in contrast to that at the top of Figure 4.11(b) where planes were cut at different orientations. Similar observations were consistently made in other analyzed regions and also in the aggregate shown in the center of the fractographies. It is believed that the more tortuous crack path inside the eutectic aggregates for the sample sintered at 1450℃ is related to stronger bonds of the interface between aggregates and the matrix since there is no phase transformation or liquid phase expected between 1400℃ and 1450℃.

4.1.8 Fracture Process Zone (FPZ)

Since Cohesive Zone Model (CZM) were used, the definition of the Fracture Process Zone (FPZ) is straightforward, namely, the region where damage is developing. To illustrate this point, the space-time horizontal tractions in the cohesive elements are shown in Figure 4.12(a) for sample MZ1-S1450G. Very similar

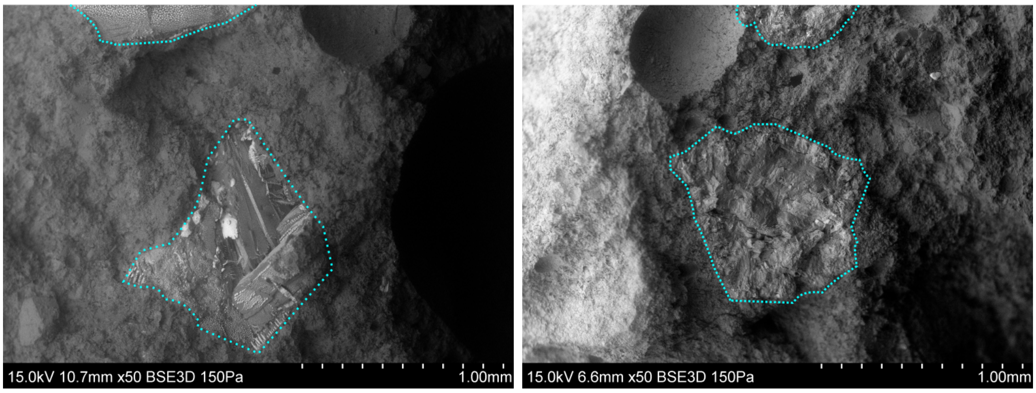

(a) (b)

Figure 4.11: SEM micrographs of fractured surfaces of samples MZ3-S1400G (a) and MZ5-S1450G (b). The cyan dotted lines highlight mullite-zirconia aggregates. Roughness differences indicate that the crack propagated along a more tortuous path for the latter, especially inside the mullite-zirconia aggregate (adapted from Ref. [117]).

conclusions are drawn from the other four samples tested at 600℃ [117], but for the sake of conciseness, they are not shown here. Each row represents a given element while each column one time step of the mode I tractions (σ_I). Some chosen levels of damage are also shown in colored solid lines. The time step when each element starts to be damaged is depicted by a magenta line, while a red line represents when 20% of damage in the element is reached, and the elements are 90% damaged for the green line. For the present implementation, no element was fully damaged. Therefore, the FPZ size was estimated counting the number of damaged elements between the magenta curve and the top of the spacetime images.

The loading curve of sample MZ1-S1450G, normalized by its ultimate load, together with the FPZ size over the experiment are given in Figure 4.12(b), where three points are highlighted, which were consistently observed in the other analyzed samples in the same F600 setup. Damage initiated in cohesive elements when the test was around 0.5 in normalized force, indicating that the BCc parameter was considered very close to damage initiation. Moreover, when the normalized force reached 0.5 but after the ultimate load, about 90% of the cohesive elements were already damaged. Last, for all samples, when the peak load was reached, more than half the height of the cohesive ligament already exhibited

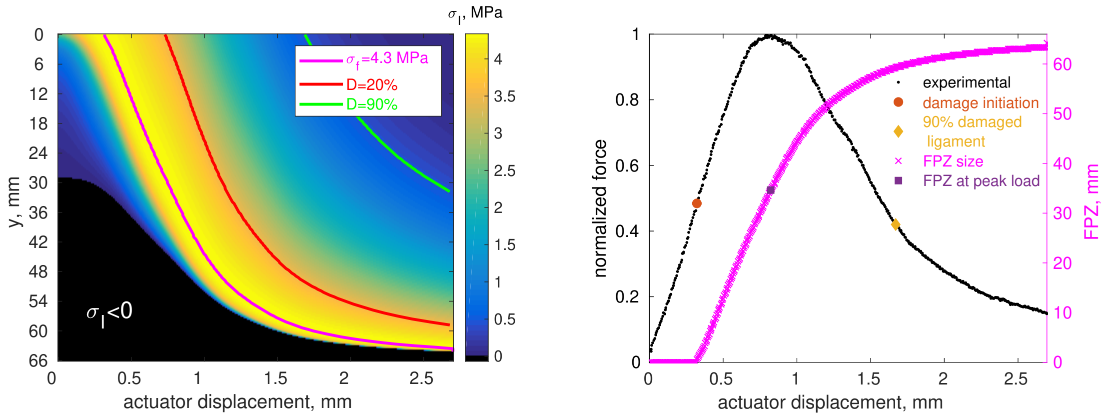

(a) (b)

Figure 4.12: (a) Space-time mode I tractions for the cohesive elements of sample MZ1-S1450G. Each row and column of the image represents one element and one time step, respectively. The full lines depict the initiation and propagation stages of damage. The black region indicates compressive stresses. (b) Normalized force and FPZ size measured by counting the number of damaged elements at given time steps. The colored markers depict points of interest discussed in the text (adapted from Ref. [117]).

some damage.

4.2 Test performed in the F900 setup

4.2.1 Crack path

To visualize the crack path, the absolute gray level residual from the DIC analyses of sample MZ6-S1450 is shown in Figure 4.13 for both surfaces. They were normalized by the effective dynamic range of the images, and thus, represent the percentage of the total number of gray levels that were not explained by the chosen kinematics. Only one major crack is visible in this test, with no bifurcation nor branch at the faces. Moreover, the crack almost followed a vertical straight path, which further reinforces the usage of the straight crack path hypothesis discussed in Figures 3.23 and 3.25. In the remainder of the ROI, only white noise is seen (as expected).

4.2.2 CMODs and NODs

The CMOD region was visible in the F900 setup. The work of fracture is calculated by integrating the splitting force vs. CMOD curves shown in Figure 4.14. The CMODs measured on the back side of the specimen are slightly higher than the levels for the front face up to the peak load, and from this point to the end of the

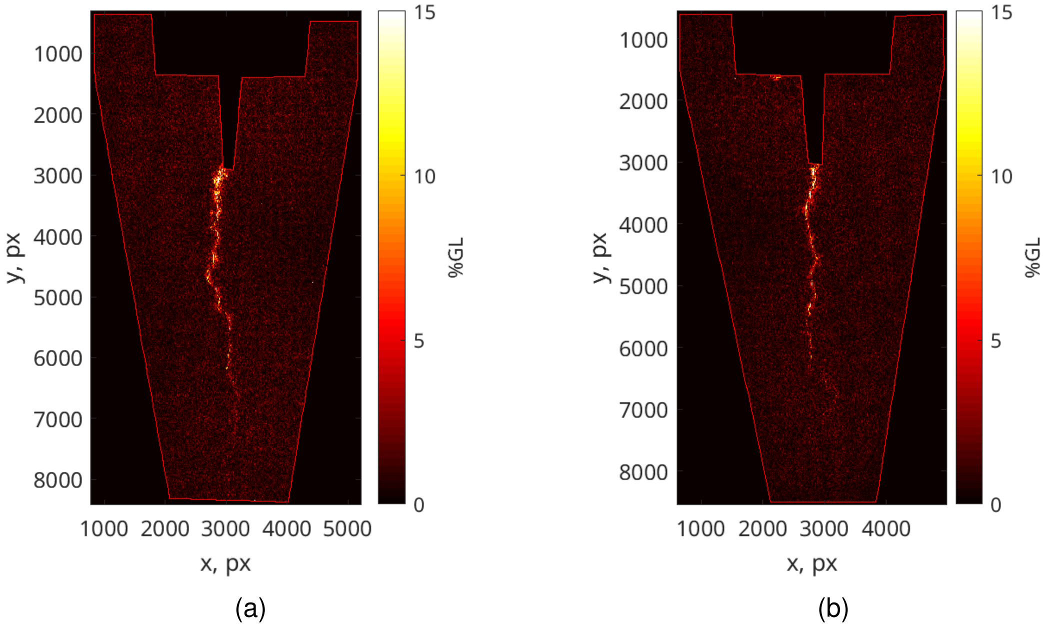

Figure 4.13: Absolute gray level residuals normalized by the effective dynamic range of the reference images acquired at 900 ℃ for the (a) front and (b) back surfaces of specimen MZ6-S1450.

experiment, they almost coincide. This symmetry is further confirmation that the setup was well positioned, apart from some small initial misalignments. Then, the fracture energy was estimated by dividing the work of fracture by twice the area of the ligament since two new surfaces were created. These calculations resulted in values of 261 J/m^2 and 255 J/m^2 for the front and back faces, respectively. If the work of the vertical force is used instead, which is calculated by integrating the vertical force vs. actuator displacement (Figure 3.14(b)), the resulting fracture energy is equal to 301 J/m^2, namely, 15% higher than the levels calculated using CMOD data. Twice these values (due to different hypotheses on the cracked area) are used for FEMU initialization of the fracture energy J_c if no better initial guess is known. However, it is worth remembering that this test was stopped at 20% of the peak load, and thus, the final energy that would be dissipated by the propagating crack beyond this point remains unknown.

In Section 3.2.1, the extrapolation from NOD to CMOD data was discussed. The development of the procedure was carried out with room temperature tests that were available from previous studies. The WST at 900 ℃ is an additional

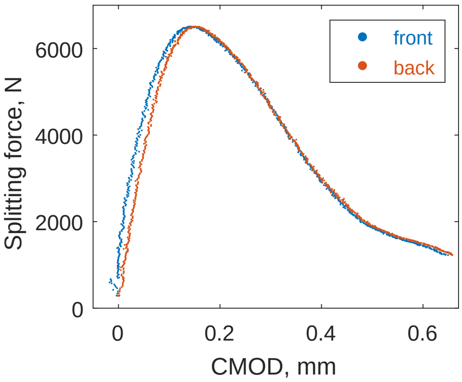

Figure 4.14: Horizontal loading curves for 900 ℃ WST of sample MZ6-S1450 with the CMODs measured for both opposite surfaces.

(and independent) source of validation for such proposition. The experimental NOD vs. CMOD curves for both analyzed faces of sample MZ6-S1450 are shown in Figure 4.15, together with their fit using Equation (3.1) for the pre-peak part, and Equation (3.2) for the post-peak regime, both with a very good agreement. These new results (obtained at 900 ℃) together with the room-temperature tests analyzed in Section 3.2.1 further validate these equations, which were utilized to analyze the experiments performed in the F600 setup.

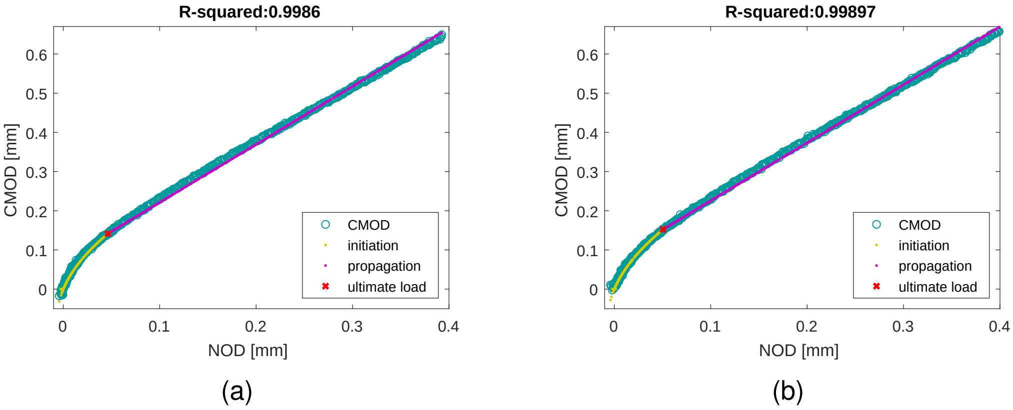

(a)

(b)

Figure 4.15: CMOD vs. NOD histories for the (a) front and (b) back faces of the 900 ℃ WST performed on specimen MZ6-S1450. The quadratic and affine interpolations are shown in yellow and purple, respectively. The ultimate load is depicted with a red cross.

The two parameters used in Equations (3.1) and (3.2) for sample MZ6-S1450 are gathered in Table 4.5. The c parameter is in the range of those reported in Table 4.3 for the five samples tested in the F600 setup, while the second one,

R, is considerably higher. Therefore, although these results confirm that such equations can be used to extrapolate the NOD vs. CMOD data, they also highlight the importance of properly calibrating R and c for each test case since no obvious trend was observed among all analyzed tests.

Table 4.5: Parameters for Equations (3.1) and (3.2) obtained for the WST performed in the F900 setup with specimen MZ6-S1450 by interpolating the NOD to CMOD data for both analyzed faces.

	front	back
R	3.06	3.01
c	1.42	1.44

4.2.3 Sensitivity analysis

Before starting the FEMU-F calibration, a sensitivity analysis of the force with respect to parameter variations was performed, which is illustrated by Hessian matrices (normalized by the standard uncertainties) at the converged state in Figure 4.16 for both analyzed faces. The four chosen parameters had very similar sensitivities to those shown in Figure 4.4(a) for the F600 setup, and to what is shown in Refs. [70, 122].

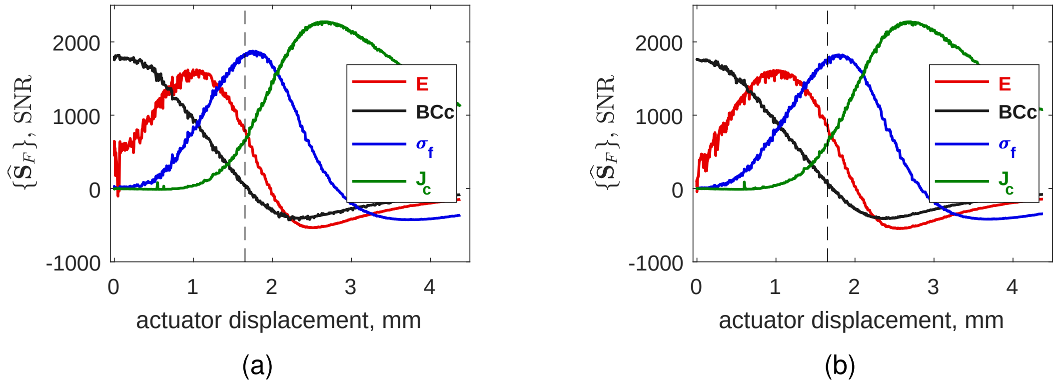

(a)

(b)

Figure 4.16: Sensitivities of splitting force $\{\mathbf{S_F}\}$ for sample MZ6-S1450, normalized by their respective uncertainty (represented as signal-to-noise ratios) for the (a) front and (b) back surfaces. The vertical dashed line depicts the ultimate load.

The Hessian matrices for both surfaces are dispalyed in Figure 4.17, along with their diagonalization. It is worth noting that the force uncertainty used for normalizing the sensitivity matrix consisted of a lower estimate, since no filtering was applied in the CMOD measurements before it was applied as boundary conditions. The values span indicates that the sensitivity is between two and three orders of magnitude higher than their uncertainty, which is higher than the previous cases, partially due to the lower force uncertainty. Both conditionings of the Hessian matrices are about 25, which is deemed very low for such identifications. From the eigenparameters shown in the third column of Figure 4.17, it is concluded that the BCc is the most sensitive, while the least sensitive comprises a mix of J_c and σ_f. No significant differences are seen between both surfaces.

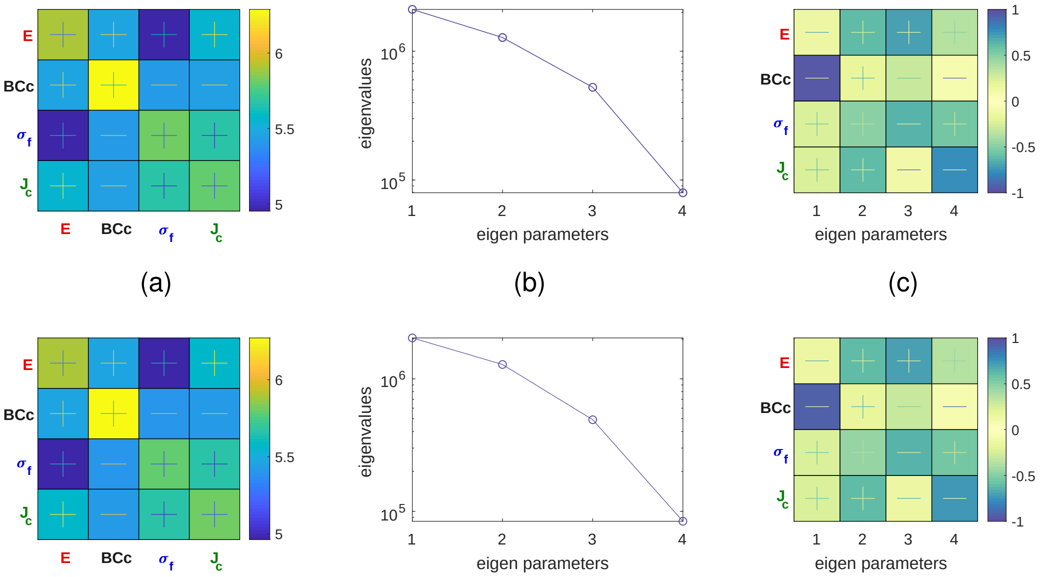

(a) (b) (c)

(d) (e) (f)

Figure 4.17: Normalized force Hessian matrices in decimal logarithm (a,d) together with their eigendecomposition. The eigenvalues are shown in sub-figures (b,e) and eigen parameters in sub-figures (c,f). The results related to the front face of specimen MZ6-S1450 are shown in the first row and those of the back surface in the second row.

4.2.4 FEMU-F calibration

A first calibration was performed only considering three parameters, namely, BCc, σ_f, and J_c, since the Young's modulus sensitivity was deemed too low to provide trustworthy results for the analyses performed for specimens tested at 600℃. They converged in eight iterations for each side, and the resulting loading curves, although not fully satisfactory, are shown in Figure 4.18(a). Then, using these new sets of converged parameters, a new calibration was run now including the Young's modulus. Ten more iterations were needed for each side, and the resulting loading curves are shown in Figure 4.18(b), providing an excellent agreement with the experimental data.

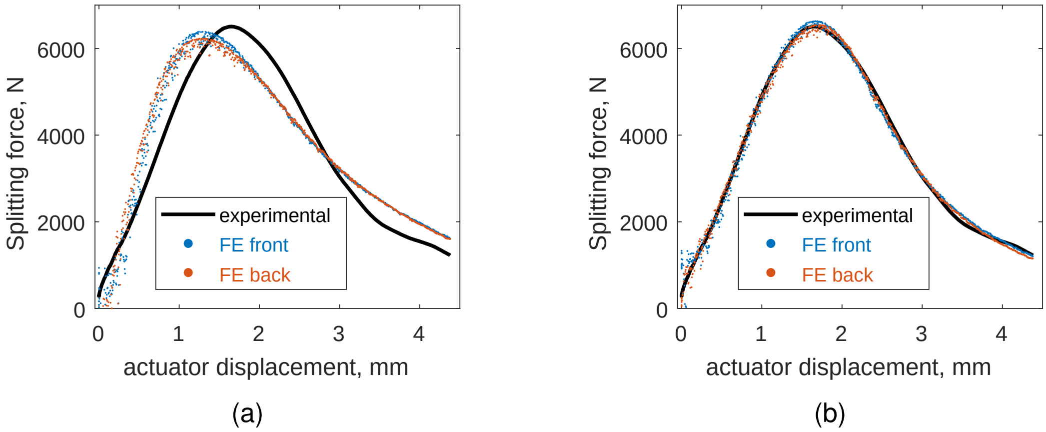

(a)

(b)

Figure 4.18: Loading curves for 900 ℃ WST of sample MZ6-S1450 together with their numerical counterparts for each surface. The case with a fixed Young's modulus is shown in sub-figure (a) and that were it was also calibrated via FEMU-F in sub-figure (b).

All the calibrated parameters for sample MZ6-S1450 are reported in Table 4.6. The differences between CZM parameters (*i.e.,* σ_f and J_c) were always less than 3% when both faces are compared. The error χ_F was reduced four and seven fold, for the front and back faces, respectively, when the Young's modulus was added in the procedure, which is remarkable for a single added parameter. Even if BCc parameters changed considerably, on both calibrations the front face had higher values, which indicates an initial misalignment of the wedge with the sample being more loaded on the back face. The calibrated Young's modulus E is 40% of its initialization. However, the 46 GPa level was calibrated from a test performed at room temperature, where images from only one side of the specimen were available and the CMOD could not be measured. It was shown in Ref. [122] that analyzing opposite faces independently could lead to Young's modulus with double the value of the other side (*i.e.,* 21 GPa and 44 GPa).

The values of χ_F (Table 4.6) are considerably higher than those gathered in Table 4.2 for the 600 ℃ tests, even if the goodness of the numerical results were as good if not better visually. Such fact comes from the smaller force uncertainty considered for the 900 ℃ WST. To further investigate this point, $\chi_F^\flat$ is also shown in Table 4.6, in which the uncertainty was calculated from the standard deviation of the first nine forces in the numerical simulation, since boundary conditions from the nine reference images were also added in the calibration. Under this hypothesis, an almost perfect match is seen, with $\chi_F^\flat \approx 1$, thereby indicating that the error came mostly from the uncertainty due to measured (Dirichlet) boundary conditions.

Table 4.6: Calibrated parameters and force cost functions for both faces and considering or not the Young's modulus (E) in the FEMU-F procedure for specimen MZ6-S1450G. $E = 46$ GPa is considered in the cases where it was fixed.

Parameter	Front, no E	Back, no E	Front, with E	Back, with E
E [GPa]	-	-	18.5	18.2
BCc	1.10	0.77	1.50	1.03
σ_f [MPa]	4.90	4.77	6.70	6.73
J_c [J/m^2]	741	733	660	642
χ_F	320	356	84	52
$\chi_F^\flat$	1.6	3.8	1.0	1.4

4.3 *In-situ* tests

4.3.1 Sensitivity analysis

Both force and COD sensitivities, *i.e.,* S_F and S_{COD}, are discussed for the case of the fine mesh adapted to the DVC residuals to justify the choice of using FEMU-F for the calibrations associated with in-situ experiments. These sensitivity matrices were calculated via finite differences with a 1% variation of each initial parameter estimate $\{\mathbf{p_0}\}$ (see Table 3.9). When normalized by the standard uncertainty as presented herein, checking if parameters are identifiable becomes straight forward since they are expressed in terms of Signal to Noise Ratios (SNR). For instance, S_F is shown in Figure 4.19, and all the sought parameters reached absolute values above three, meaning that sensitivities were higher than three times the uncertainty level at some time steps. Further, their weak temporal correlation is an additional benefit, reducing the probability of linear dependence among parameters. Their qualitative trend is also very similar to what was observed for 2D cases [70, 117, 122]. For instance, BCc is predominant at the beginning of the test, then σ_F around the ultimate load of the experiment, and

J_c is activated at later stages of the experiment.

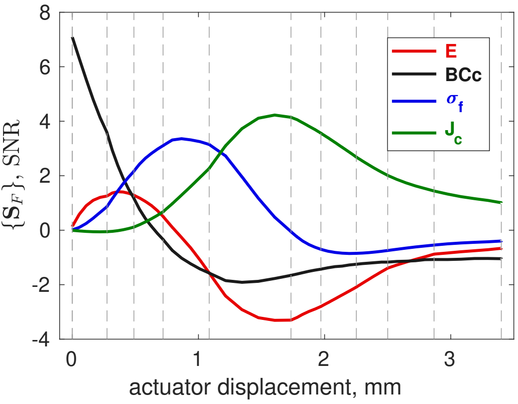

Figure 4.19: Force sensitivities for sample MZ-C1 with the initial set of parameters (Table 3.9) after a 1% perturbation normalized by the force uncertainty. The vertical dashed lines depict the tomographic scans (adapted from Ref. [124]).

Conversely, the COD sensitivity fields (for the x-direction), whose levels are two order of magnitude lower than the force sensitivities, are displayed in Figure 4.20, calculated for the same initial parameters (Table 3.9). Negative sensitivities are related to opening decreases when the parameter is increased. These very low sensitivities indicate that parameters would need updates of the order of 50% or more their initial value to decrease the COD cost function by one time its standard uncertainty. In that case, if force and COD data were used as the quantities in the cost function to be minimized, the calibration would be mostly guided by force measurements.

Further analyzing COD sensitivity fields helps to understand how these parameters influence crack propagation. For instance, increasing the Young's modulus (first row in Figure 4.20) would make the crack to open more, around scan #5, right after the ultimate load. This trend happens since the crack may initiate and propagate easier with a higher elastic energy in the system, as usually discussed in thermal shock theories [137, 138] and also in the introduction of the WST setup [36, 139]. By increasing BCc parameter, the prescribed opening itself is increased, and therefore, a similar opening trend is seen (second row in Figure 4.20), but with a stabilization from scan #4 to the end of the simulation. These first two fields also highlight that opening was higher at low y-coordinate values, and therefore deviate from symmetry assumptions that are usually considered for

2D cases.

Increasing the cohesive strength (third row in Figure 4.20) delays crack initiation (negative sensitivities), while further opening the crack at later stages since it would also decrease the maximum separation for full element failure (when other parameters are kept constant). The cohesive strength σ_f was also the least sensitive parameter, with a five-fold smaller sensitivity when compared to the others. Last, the fracture energy (fourth row in Figure 4.20) showed a near-zero sensitivity when few or no elements were damaged for the first scans. However, increasing J_c tends to close the crack since more energy would be required to open it. It is worth reminding that such sensitivities may considerably change when parameters are updated in the iterative scheme.

Similarly to what was shown for the 600℃ setup, the sensitivity matrices are used to calculate the Hessian matrices separately (*i.e.,* one for the force and one for the COD). Their absolute values are shown in decimal logarithm in Figure 4.21 along with their respective diagonalization. Most of the force Hessian matrix (Figure 4.21(a)) indicates an average sensitivity above uncertainty (*i.e.,* above zero in decimal logarithm), while the highest value in the COD Hessian matrix (Figure 4.21(d)) is considerably lower. Another point of interest is that their conditioning, which is calculated from the ratio of their first to last eigenvalue, whose values of 130 and 490,000 are obtained for the force (Figure 4.21(b)) and NOD (Figure 4.21(d)) data, respectively. The former provides a more stable parameter calibration. The lowest eigenvalue of the force diagonalization (Figure 4.21(c)) indicate that the sensitivity may not be sufficient to uncouple E and J_c, as can be seen from their anti-correlation in the force sensitivities in Figure 4.19 (apart from the very beginning). For the COD data, not only are the eigenvalues very small, with sensitivities considerably below the uncertainty, but the eigenparameters show stronger couplings among the sought parameters, which would make them unidentifiable if only COD data were used. Similar conclusions were obtained from full displacement fields or from gray level residuals [124], further confirming the choice of using FEMU only with forces in the cost function (*i.e.,* FEMU-F).

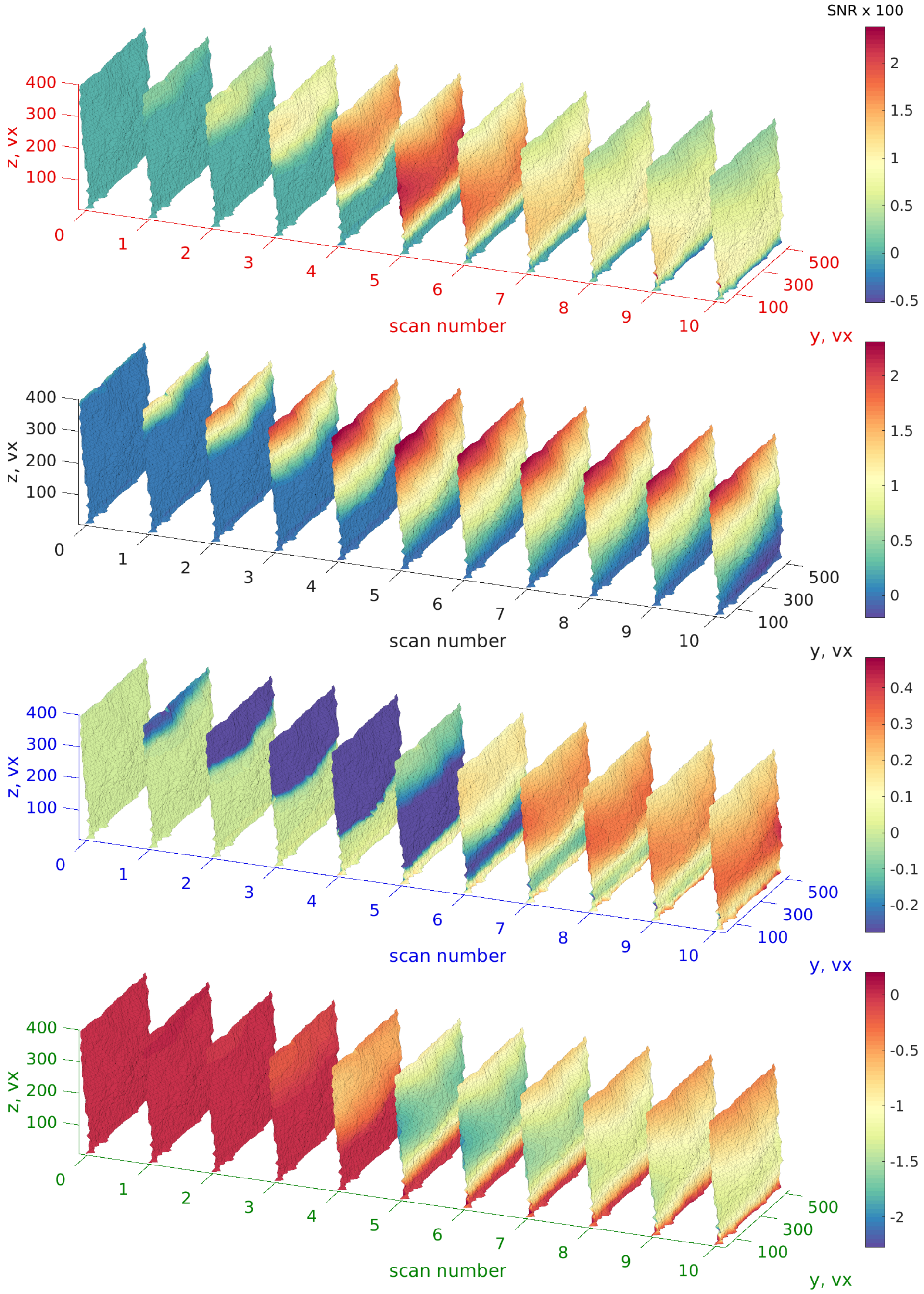

Figure 4.20: Sensitivity fields S_{COD} for the displacement jump in the x-direction of sample MZC1-S1450G for a 1% variation of the parameters E (top row), BCc (second row), σ_f (third row), and J_c (bottom row), (adapted from Ref. [124]).

4.3.2 FEMU-F calibration

Results for the straight crack path (Figure 3.21(a)) are first presented, with the loading curve for every iteration shown in Figure 4.22(a), together with its experimental counterpart. Each iteration made the simulated forces closer to the

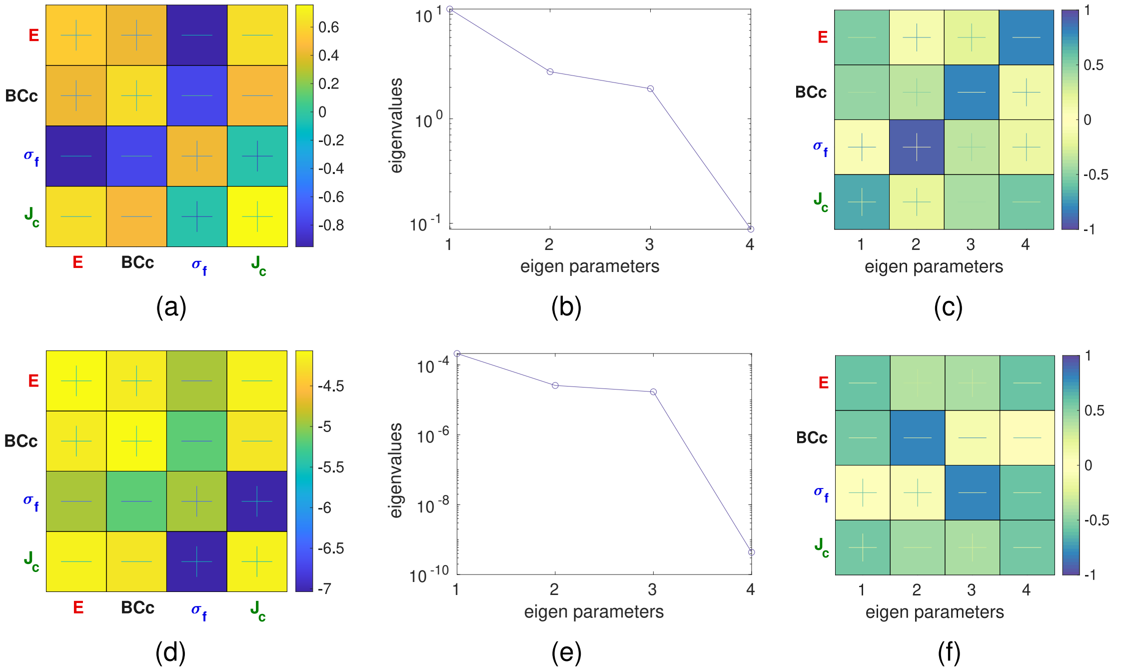

Figure 4.21: Normalized Hessian matrices in decimal logarithm (a,d) together with their eigendecomposition. The eigenvalues are shown in sub-figures (b,e) and eigenparameters in sub-figures (c,f). The results related to force measurements are shown in the first row and to COD data in the second row (adapted from Ref. [124]).

experimental data, reducing from 150 to only seven times the uncertainty level as shown by the χ_F level in Figure 4.22(b). Changes in parameters are displayed in Figure 4.22(c), normalized by the converged parameters, showing how most parameters needed small updates (*i.e.,* no more than 30%) apart from the Young's modulus that was initialized with three times its converged level. This difference could be partially explained by the mold made for producing the cylindrical samples that allowed air bubbles to enter from the bottom gaps, leading to a more porous mesostructure in comparison to the prismatic samples studied using the F600 setup [116]. Although tests would be necessary to prove this point, the bottom mold sealing could be improved to avoid such bubbles.

The results following the same calibration procedure but using the mesh with cohesive elements adapted to the crack path are reported in Figure 4.23(b). This case also converged in seven iterations when initialized with the same parameters. However, for the first iteration, even if χ_F was practically the same for both meshes, the load curve was considerably different, reaching ultimate split-

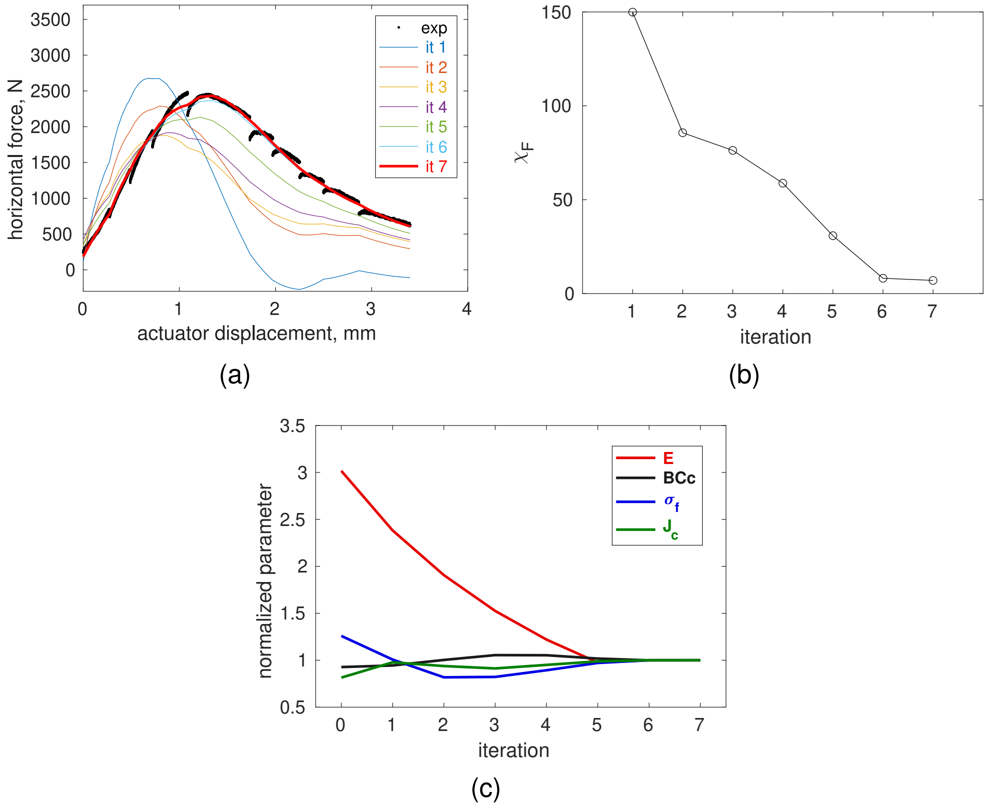

(a) (b)

(c)

Figure 4.22: Results for parameter calibration with a straight crack path (Figure 3.21(a)). Loading curves (a), global force residual χ_F (b), and calibrated parameters (c) for each iteration (adapted from Ref. [124]).

ting forces about 1000 N higher in the latter case. This observation reinforces the critical role of the definition of the crack path in such identifications, which is the sole difference among the two numerical simulations. A drastic reduction in χ_F is also seen in Figure 4.23(b), with almost identical initial and final values. For the calibrated parameters, the biggest difference comes from the cohesive strength σ_f (Figure 4.10(c)), which converged to a value almost half of its initialization.

The calibrated parameters gathered in Table 4.7 reinforce the importance of the crack path definition, with the cohesive parameters being the most affected, with 40% difference in σ_f and 10% in J_c. Therefore, the crack path plays a critical role on damage initiation (with a smaller σ_f when adapted to the realistic crack path), while the differences in fracture energy were proportional to changes in the surface area of the crack path. Differences in Young's moduli and on BCc were negligible; especially on BCc, this was expected since the same boundary

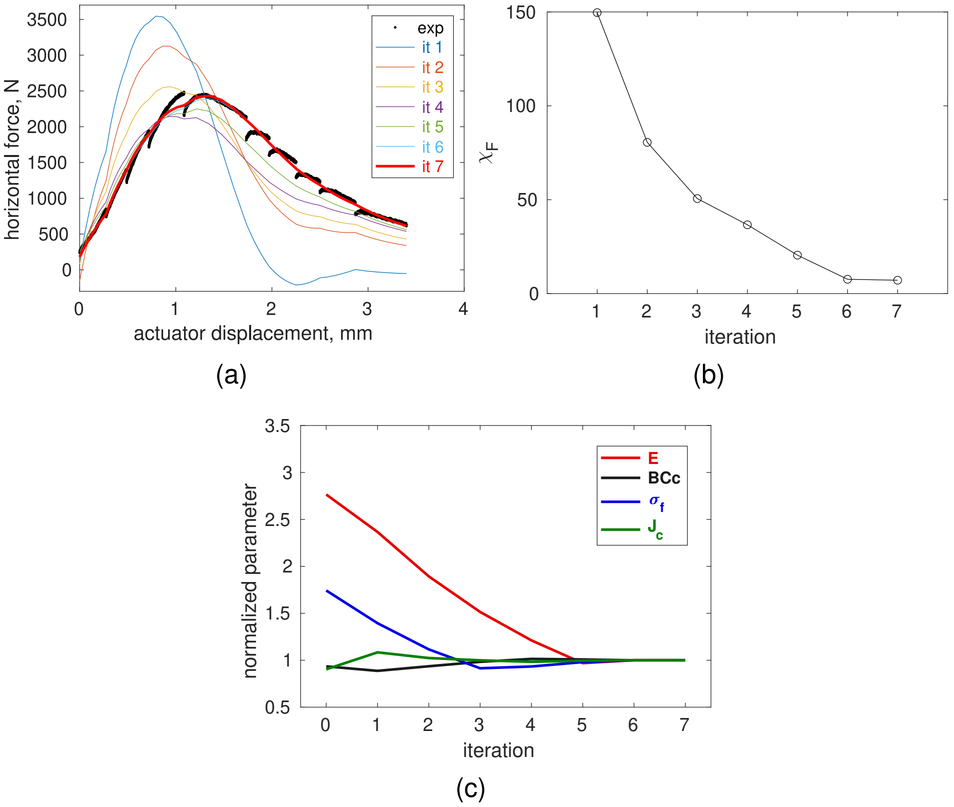

(a) (b) (c)

Figure 4.23: Results for parameter calibration with an adapted crack path (Figure 3.21(b)). Loading curves (a), global force residual χ_F (b), and calibrated parameters (c) for each iteration.

conditions were used, which were obtained with the coarse mesh (Figure 3.20(a-c)).

Table 4.7: Calibrated parameters for the two crack paths for MZC1-S1450G specimen (adapted from Ref. [124]).

Parameter	Straight crack	Adapted crack
E [GPa]	16	17
BCc	1.08	1.07
σ_f [MPa]	3.4	2.5
J_c [J/m^2]	325	295
χ_F	7.0	7.1

One interesting fact is that a value between 50% and 60% of the so-called nominal tensile strength was claimed to be a good initialization for the cohesive strength σ_f [117], using the same material but with a prismatic sample and a 2D numerical simulation. This hypothesis corresponds to 4.6 MPa for the present experiment, whose 55% leads level to 2.5 MPa, the same value calibrated for the adapted mesh. The PPR traction-separation law using the initialization parameters and those after convergence for both cases are plotted in Figure 4.24 to show the influence of the crack topography on their calibration.

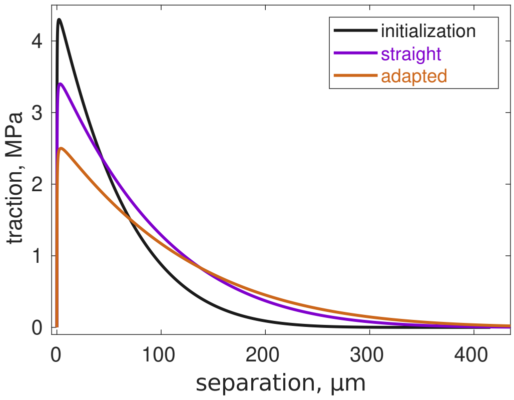

Figure 4.24: PPR traction-separation law using the initial parameters σ_f and J_c (Table 3.9) or the converged ones (Table 4.7) for both studied meshes (adapted from Ref. [124]).

Last, the χ_F difference of 0.1 at convergence (Table 4.7) proves that a very similar description of the loading curve was achieved in both cases, with their average difference being ten times lower the uncertainty levels, hence statistically indistinguishable. Thus, kinematic residuals are used in the sequel to investigate the calibration trustworthiness.

4.3.3 Kinematic residuals

Although kinematic cost functions were not used in the calibration procedure due the low COD sensitivities (Section 4.3.1), they are reported hereafter to evaluate the faithfulness of the FE simulations. First, the gray level residuals are presented in Figure 4.25(a). They were calculated either deforming one volume using displacements obtained from DVC calculations or resulting from FE simulations, for all three meshes. Such analyses are possible since measured boundary conditions were used, together with the proper positioning of the meshes. When the same meshes are compared, the residuals are higher when the FE kinematics was used to correct volumes of deformed configurations, in comparison to DVC where more degrees of freedom were allowed to improve such description instead of only four chosen parameters. However, they are very close, especially with all the kinematic constraints in the FE simulations. Among finer meshes, the one adapted to the crack path provided smaller residuals since it was optimized for it. DVC with the coarser mesh provided very similar results at the beginning, but started to deviate from the others when the crack started to propagate since it was not accounted for by its kinematic basis. Last, higher residuals around scan #5 are due to the fact that dark field corrections for the tomographic volumes could only be acquired at the beginning and at the end of the experiment, while the increase of residuals from scan#8 onward was mainly related to higher crack openings.

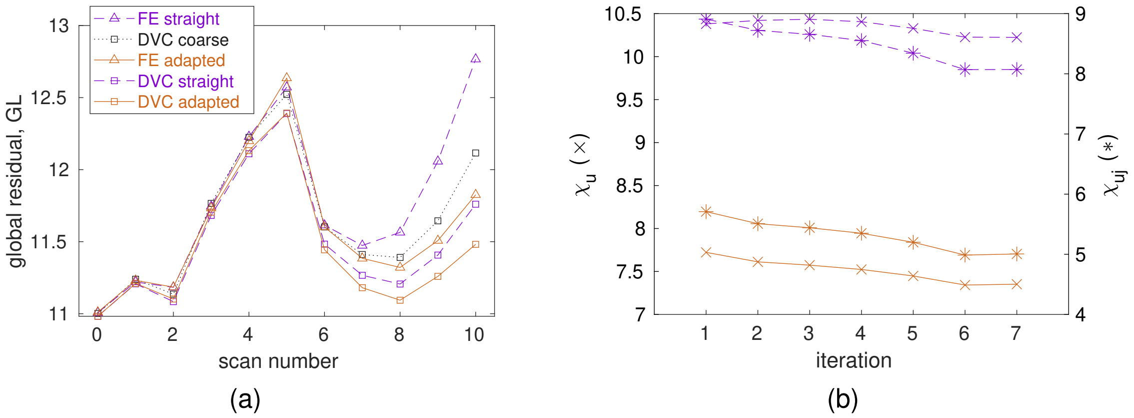

Figure 4.25: (a) Gray level residuals for DVC analyses using different meshes (squares) or FE simulations driven by measured boundary conditions (triangles). The black dotted line depicts the analysis using the coarse mesh (Figure 3.20), while dashed and solid lines represent the usage of meshes with a straight crack path or adapted to the real crack path, respectively (see Figure 3.21). (b) Cost functions using full displacement fields (χ_u, depicted with crosses) or only the crack opening displacement in the x-direction (χ_{uj}, depicted with stars), adapted from Ref. [124].

The two cost functions related to the displacements are displayed in Figure 4.25(b), namely, χ_u on the full displacement fields (crosses) and χ_{uj} calculated from the displacement jump, *i.e.,* the crack opening displacement in the x-direction (stars). It is worth emphasizing that they were not used in the minimized cost function, even if they were consistently reduced for each iteration. However, their decrease was smaller than one, representing that overall a similar kinematic description was achieved for every iteration, in relation to its uncertainty. Moreover, at initialization, the kinematic cost functions χ were around 10 times the uncertainty level, which is very low compared to the 150 level from the force measurements (even if at the converged state χ_F were even smaller than

χ_u and χ_{uj} for both meshes). When comparing both meshes, the one adapted to the crack path had smaller residuals both in displacements and crack opening displacements by three times their uncertainty. This result proves that even if both meshes gave very similar results on the macroscopic level when globally comparing the forces, on the mesoscopic (using displacements) and microscopic (voxel-wise gray level residuals) the adapted mesh provided a better description, and therefore, the calibrated parameters are more representative of the analyzed test.

The displacement jump residuals used to calculate χ_{uj} for the adapted mesh at the converged state are shown in Figure 4.26. Before scan #4 (the ultimate load), the residuals were already very low. However, for later stages of the experiment, it increased reaching a maximum amplitude of twenty times the uncertainty for scan #10, which also illustrate why later time steps were not accounted for herein. These maps of residuals show spacetime-wise where (and when) improvements were possible in the numerical model to better describe the experiment. To exemplify, in order to better describe scan #10, the CZM would need more opening closer to the notch and even some closure at mid-height, while not changing at the bottom.

One single FEMU with COD in the cost function (FEMU-COD) iteration was run, initialized with the converged FEMU-F parameters, and χ_{uj} was reduced by 0.01 while χ_F increased from 7 to 52 (with similar trends on following iterations). Therefore, it is believed from the low levels of residuals reported that the current simulation using the adapted mesh and the converged FEMU-F parameters are close to the limits of the chosen CZM to simulate the present experiment.

If only the description of the loading curve was sought, the straight crack path could be used. However, the kinematic residuals shed light onto possible differences on the obtained parameters under different hypotheses about the crack path morphology. It is worth emphasizing that care should be taken using such parameters for design purposes, especially considering that variations between samples were not discussed herein.

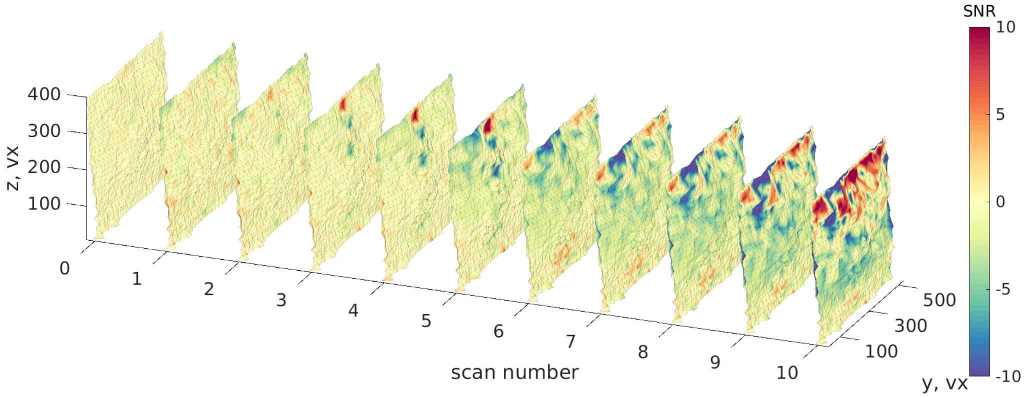

Figure 4.26: Displacement jump residual, in the x-direction, using the parameters after FEMU-F convergence. Positive residuals indicate that the opening measured via DVC was higher than that predicted by FE simulation.

4.3.4 Dissipated energy

The COD fields for FE simulations using both crack paths are shown in Figure 4.27 along with the experimental COD extracted from DVC analyses for the adapted crack path, all using the same dynamic range for easier comparison. They show a very close trend, as expected, since the simulations had the same boundary conditions. However, the FE fields (first and second row in Figure 4.27) are considerably smoother while the DVC results (third row in Figure 4.27) have higher fluctuations. These fluctuations are not due measurement uncertainties (Table 3.7) but are believed to be caused by the heterogeneous microstructure of the studied castable at the scale of Figure 3.20(a,b). Even if the calibrated fracture energy J_c was higher for the adapted crack case, this increase was shown to be directly related to the increased area in the crack path. However, initiation and propagation of damage were considerably changed due to the calibrated parameters. For instance, with the converged parameters, cohesive elements in the straight crack path started to be damaged with 3.1 µm opening and dissipated energy up to 626 µm, while for the adapted crack path these levels were 3.9 µm and 782 µm, respectively. Damage initiation started at levels slightly below the COD uncertainty (of 7 cvx or 9.4 µm), but could be evaluated with the present strategy.

One interesting additional information extracted from the FE simulations that

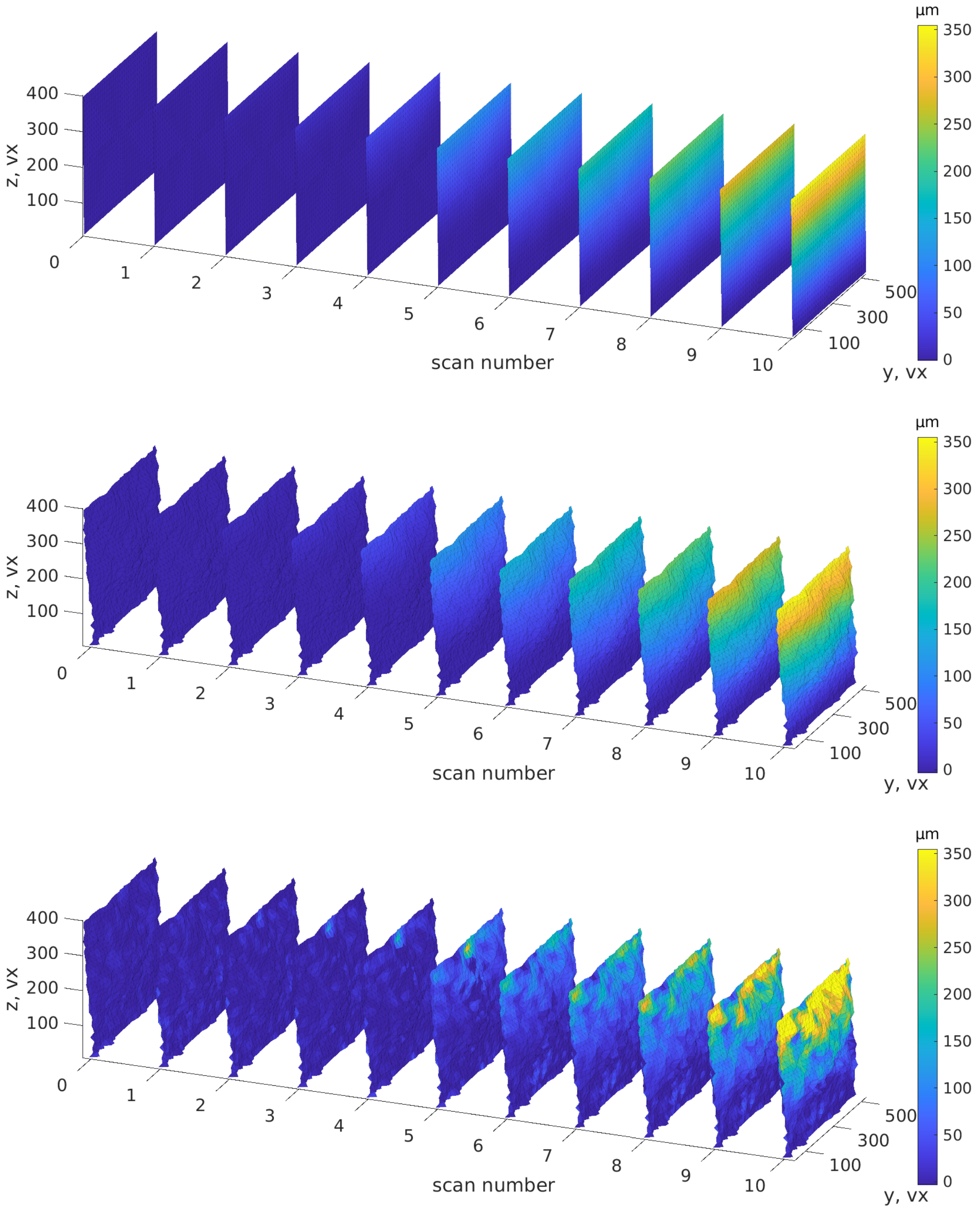

Figure 4.27: Crack Opening Displacement (COD) in the x-direction calculated for each cohesive element using the meshes with a straight (first row) or adapted (second row) crack path. The third row shows the measured COD fields via DVC using the adapted mesh (adapted from Ref. [124]).

cannot be directly measured is the normal traction maps for each time step, which are shown in Figure 4.28. Their maximum amplitude was set to the calibrated cohesive strength σ_f for each case. Thus, care should be taken to directly compare them since the color does not represent the same absolute traction, even if qualitatively their evolution remains similar. For instance, in scan #3, the first row of elements was already damaged, while in scan #5, right after the peak load, damage was seen even below mid-height of the specimen. From this point onward, the initiation front reached compressive zones at the bottom of the sample and was slowed down.

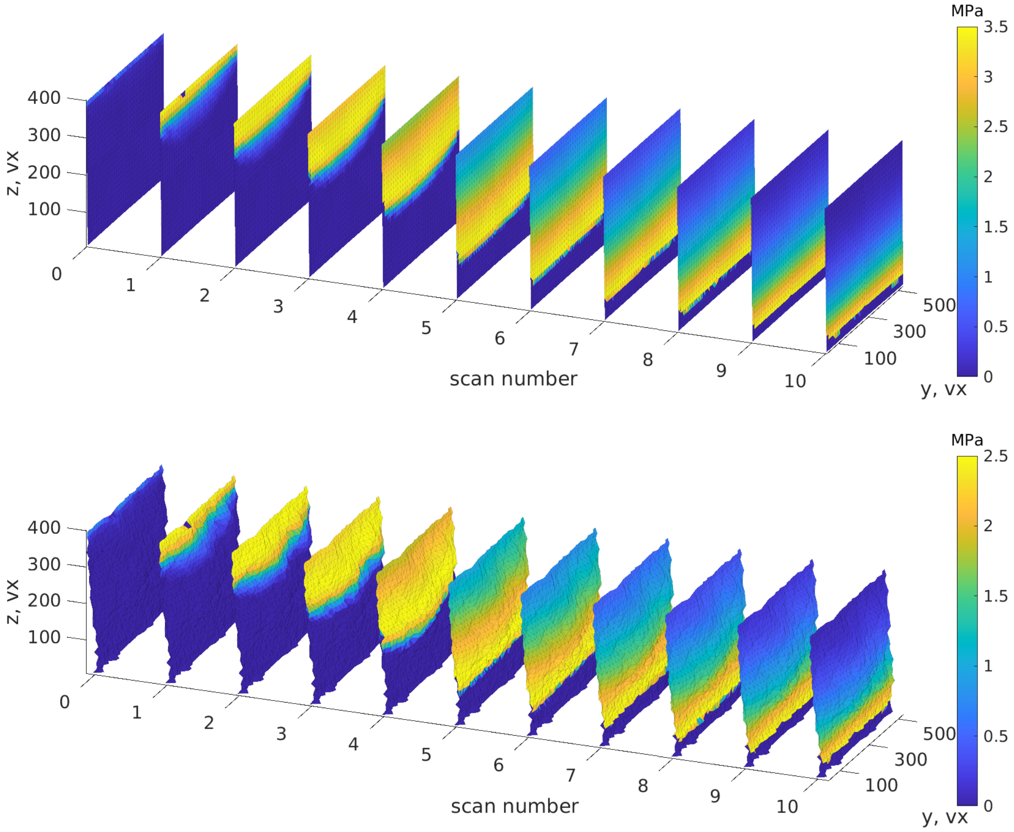

Figure 4.28: Tractions in the x-direction for each cohesive element using the mesh with straight (first row) or adapted (second row) crack path (adapted from Ref. [124]).

The cumulated work for the studied cases is reported in Figure 4.29. An upper bound is given by the line called vertical (in red), calculated after integration of the experimental actuator displacement vs. vertical force, which includes contributions from possible friction and energy stored in the loading frame. A second line named CMOD (in black) was computed with the opening of the load application area obtained from DVC together with the splitting force, and therefore considers only the work done of the force applied to the sample. Both calculations did not require results from FE simulations, and included the elastic energy stored in the sample, which should vanish as the crack reached the bottom of the specimen.

The last two lines (in purple and orange) were calculated for contributions of all

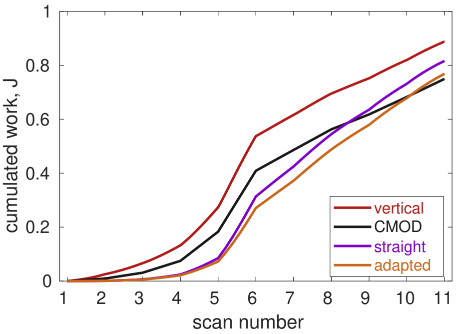

Figure 4.29: Cumulated work during the experiment assessed with four different approaches. The line called “vertical” is calculated using only point data gathered during the experiment, while ‘CMOD” employs DVC results, and the last two, “straight” and “adapted,” are computed using FE simulation results (adapted from Ref. [124]).

cohesive elements in the analyzed meshes for each time step, using the normal COD (Figure 4.27) and tractions (Figure 4.28) associated with the element area. Both contributions were very close for very low levels (or absence) of damage up to scan #4, when they started to deviate and the case with the straight crack path dissipated more energy. In these last calculations, the work to elastically load the sample was not considered, and therefore it was expected to be lower than the first two discussed curves, and also that they should converge to similar values at the end. Last, the mesh adapted to the crack path led the last value closer to the CMOD case.

The final elastic energy was removed from the cumulated work to calculate the dissipated energy displayed in Table 4.8. Three different cracked area assumptions were considered. To compare to cases with no FE simulations, both the applied force and the CMOD cases considered a full straight crack path along the full height of the sample, as commonly considered for fracture energy evaluation in WSTs [139–141]. For both cases, the cracked surface was the area of elements that were fully damaged at the end of the experiment. Then, fracture energies shown in Table 4.8 could be evaluated by dividing the dissipated energies by the cracked areas. It is worth noting that all the reported fracture energies were less than the calibrated fracture energy J_c since many cohesive elements were not fully damaged. The straight crack assumption gave a fracture energy even higher than that calculated from the applied force, which is an upper bound.

Conversely, the one for the adapted mesh was closer to that from CMOD data, further validating the mesh adaption.

Table 4.8: Dissipated and fracture energies for different methods of evaluation (see text).

	Dissipated energy, J	Cracked area, mm^2	Fracture energy, $J.mm^{-2}$
applied force	0.70	3550	198
CMOD	0.60	3550	169
straight	0.69	3280	212
adapted	0.62	3670	170

When the dissipated energy was sought, a simple choice of using CMOD data with the assumption of a straight crack path gaves values very close to the mesh adapted to the crack path. However, the fact that most of the fracture energies reported in Table 4.8 overestimate the one from the adapted mesh highlights that care should be taken when cohesive elements are used to simulate quasi-brittle fracture with toughening mechanisms.

4.3.5 Other *in-situ* experiments

Cyclic MZC2-S1450G test

The very same methodology discussed above for sample MZC1-S1450G was applied to the cyclic experiment performed on sample MZC2-S1450G. The parameter calibration procedure converged in six iterations to the (not so satisfactory) result shown in Figure 4.30(a). It became clear that some adjust had to be made, since the overall unloading and reloading trends could not be described. Further confirmation was given when the sensitivity analysis was performed (Figure 4.30(b)) with the points related to the envelope of the loading curve being the most sensitive and with the unloads barely seen. It is believed that the analysis of cyclic WSTs can be circumvented by using a constitutive model that couples damage and plasticity (*e.g.,* the Concrete Damaged Plasticity law implemented in Abaqus). Such discussion, however, is out of the scope of this thesis and is left as perspective for future studies.

Deviations from straight crack paths in cylindrical samples

Both MZC1-S1450G and MZC2-S1450G samples had cracks that followed the middle plane of the sample. However, this did not happen for all the other

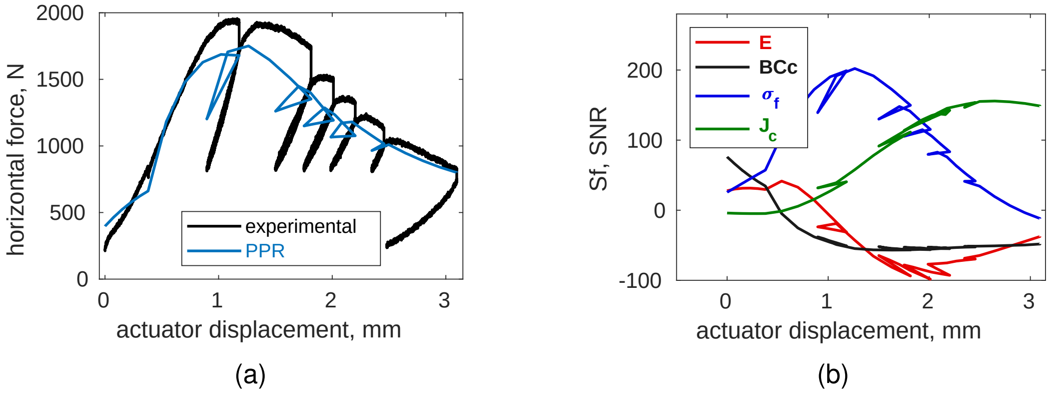

Figure 4.30: (a) Experimental loading curve for sample MZC2-S1450G together with the FE simulation using the PPR cohesive model with calibrated parameters for this test. (b) Sensitivity of the simulated forces for each sought parameter, calculated via finite differences with a variation of 1% of the parameters.

tested samples. To illustrate this point, before further discussing the last three experiments, two samples that were tested in late 2018, before the start of this thesis, are shown in Figure 4.31, both with lateral grooves to guide the crack. The first experiment with this geometry and material (Figure 4.31(a)) was performed in Brazil to check for stable crack propagation, which was successful. However, the crack deviated from the lateral grooves and propagated in a “J” shape, as highlighted by red arrows. The same trend was observed for the second specimen (Figure 4.31(b)) sent to France to test the feasibility of *in-situ* experiments for this thesis, which was also used for a research project with French students.

The last three specimens tested *in-situ* (*i.e.,* MZC3-S1450, MZC4-S1450, and MZC5-S1450G), whose testing protocol was aimed for P-DVC analyses, presented a third crack path. The crack initiated from the edge of the load application area, as shown by a slice of a residual volume from a DVC analysis in Figure 4.32. In that case, stable crack propagation was also achieved (Figure 3.15), even if a considerably smaller energy was dissipated in the process, in part due to the smaller fracture surface that was created.

This different crack path made the definition of the kinematics more complex, since the 3D displacement fields calculated for samples MZC1-S1450G and MZC2-S1450G could not be extrapolated. Moreover, the smaller cracked area

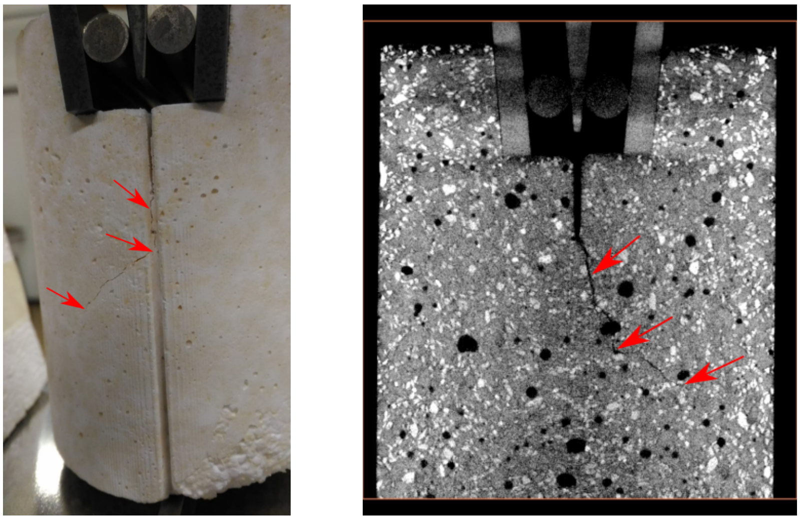

(a) (b)

Figure 4.31: Post-mortem images of samples tested before this thesis. (a) Photograph of the first specimen tested in Brazil and (b) one slice of tomographic volume of the second specimen tested in France. The crack path is highlighted with red arrows.

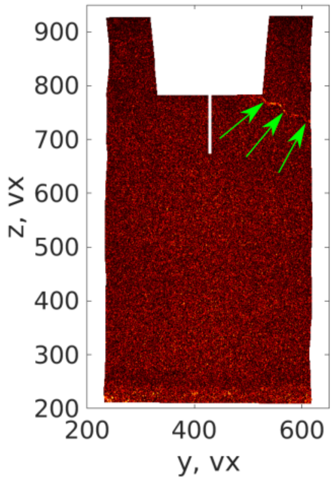

Figure 4.32: $y - z$ slice of the residual volume of one DVC analysis of sample MZC3-S1450, highlighting with green arrows the crack that propagated from the corner of the loading application region.

may lead to higher variations in calibrated parameters, or not be representative at all, considering that the biggest aggregate size is in the order of 3 mm. These considerations, together with time constraints, made that only preliminary P-DVC analysis with codes developed at LMPS were performed, but were not fully conclusive.

4.3.6 Geometrical improvements for cylindrical samples

It is believed that the three different crack paths seen in cylindrical samples are related to the chosen geometry and its fabrication process. For instance, for homogeneous cylindrical samples, the weakest path for crack propagation may deviate from the middle plane since the cross-section area is reduced and thus less energy is needed. However, especially crack initiation will depend on the heterogeneity of the sample (*e.g.,* the presence and location of big defects). For instance, both sample MZC1-S1450G and MZC2-S1450G heights were slightly smaller than the others (by about 10 mm), which was due to the mold not being completely filled during sample production. Thus, this difference could have helped to intensify less the stresses at the edges where load was applied so that the crack initiated from the notch as expected. Some air bubbles could also have occurred close to these edges for samples MZC3-S1450 to MZC5-S1450G, which would even worsen this stress concentration.

Mold sealing could be improved to avoid air going inside it during vibration for the initial conformation, which may induce porosity in the final samples. Printing higher rigidity molds and adding a rubber o-ring at its bottom part could improve this feature. Rounding the corner of the sample where the loading is applied with about 2 mm radius could also diminish the probability that crack would start there. Additionally, both lateral blocks that apply the load would need to be chamfered on the edge that is in contact with the specimen (*i.e.,* bottom right of Figure 2.1(b)), which could also be used in the setup of specimens with the geometry used herein. Last, especially for cylindrical samples, it is advised to maintain the lateral grooves to guide the crack in order to avoid severe deviations from the middle plane.

4.4 Discussion of results from the three experimental setups

A total of seven specimens were tested and had parameters calibrated via FEMU. Although a small number of samples were used as a proof of concept for the developed methodologies, comparisons may illustrate possible correlations between processing of the sample and calibrated properties. The variability of the obtained parameters, however, do need further investigation with more specimens, and the following comparisons should not be taken as rigid guidelines.

A summary of such results is given in Table 4.9 along with information about sample processing and testing setup and conditions. Overall, the χ_F levels indicate that the applied FEMU procedure led to errors between numerical simulations and experimental data of the order of (only) ten times the experimental uncertainty while using very few degrees of freedom (from three to six parameters). The higher values for sample MZ6-S1450 (*i.e.,* 84 and 52, see Table 4.6) were due to the lower standard force uncertainty together with not filtering the DIC results before applying them as boundary conditions. However, if the force oscillations for numerical simulations with boundary conditions measured from reference images was used as the normalizing factor, the obtained χ_F tended to unity, thereby indicating that sample MZ6-S1450 is the case where the experiment was best described among those presented in Table 4.9. It is worth remembering that samples MZ1-S1450G to MZ5-S1450G were monitored from a single side, and the CMOD was not measurable. Similar configurations presented a Young's modulus of almost double level for one face in comparison to the other (for a different material) [122], and therefore $E = 46$ GPa is not fully trustworthy. However, the Young's modulus around 18 GPa provided a higher confidence since it was consistent for both faces of sample MZ6-S1450G and also similar to those obtained for sample MZC1-S1450G, both tests with data accounting for 3D aspects of the experiment.

In the same study [122], the CZM parameters varied by about 10% among both analyzed faces, even with a very different Young's modulus. This fact makes these parameters obtained for the first five samples more likely to be comparable among specimens, even if care should be taken since they underwent different heat treatments. For instance, the sole difference among experiments MZ1-S1450G and MZ5-S1450G was the testing temperature of 600℃ for the latter, which decreased σ_f by 10% while increased J_c by 70%. The effect of further increasing the testing temperature is quantified comparing samples MZ4-S1450 and MZ6-S1450, where the 300℃ increase augmented σ_f by 80% and J_c by 60%.

Table 4.9: Summary of experiments analyzed via FEMU in this thesis (with compact designation for improving the table readability). For sample MZ6, the results are provided for the front and back faces analyzed independently, while for specimen MZC1 the results are given considering a straight crack path and one adapted to the DVC voxel-wise residual map.

Specimen	MZC1	MZ1	MZ2	MZ3	MZ4	MZ5	MZ6
Lateral grooves	yes	yes	no	yes	no	yes	no
Sintering temp. [℃]	1450	1450	1400	1400	1450	1450	1450
Experimental setup	XCT	F600	F600	F600	F600	F600	F900
Testing temp. [℃]	≈ 20	≈ 25	600	600	600	600	900
χ_F	7.0 | 7.1	6.6	13.4	14.7	5.9	19.8	1.0 | 1.4
E [GPa]	16 | 17	46	-	-	-	-	18 | 18
σ_f [MPa]	3.4 | 2.5	4.3	3.5	3.8	3.7	3.8	6.7 | 6.7
J_c [J/m^2]	325 | 295	266	327	361	405	456	660 | 642
ℓ_H [mm]	450 | 802	661	1228	1150	1361	1453	265 | 257

These trends reinforce the importance of performing such calibrations using experimental conditions as close as possible to the final envisioned application in order to have trustworthy and representative parameters for the studied material.

Another source of changes in parameters is the geometry of the sample. When specimens MZ2-S1400 and MZ3-S1400G are compared, or MZ4-S1450 and MZ5-S1450G, the presence or not of lateral grooves to guide the crack was the main difference. Even if little influence is seen in the cohesive strength, the fracture energy increased by 10% when grooves were used. This change could be caused by the preferential path for the crack being prescribed, and therefore not allowing it to be guided by the weakest spots dissipating less energy. For design purposes, the case with grooves provides a lower estimate and therefore could be used for increased safety. Similar treatments (*i.e.,* sintering and testing temperatures) were also undergone by samples MZ1-S1450G and MZC1-S1450G but with more discrepancies in geometry, the latter being cylindrical, slightly smaller in height and with triangular grooves (Figure 3.10). Even if sample MZC1-S1450G had smaller cohesive strength σ_f and higher fracture energy J_c, there was also a difference in numerical simulation (2D vs. 3D), which may have some influence on the calibrated parameters.

The sintering temperature of the specimens also influenced the calibrated CZM parameters. By comparing specimens MZ2-S1400 to MZ4-S1450G, and

MZ3-S1400G to MZ5-S1450G, an increase of 50℃ (from 1400℃ to 1450℃) was investigated. Similar cohesive strengths σ_f were obtained together with an increase of 25% in fracture energies. This observation illustrates that such methodologies could also be used to investigate different treatments, such as sintering temperature or different compositions, aiming for material selection for a given application.

In the last line of Table 4.9, the Hillerborg length [94] is reported, which is defined as

$$\ell_H = \frac{E J_c}{\sigma_f^2} \tag{4.2}$$

It can be used to estimate the FPZ size [142, 143], which is usually considered to be one order of magnitude lower than ℓ_H. With the ligament length around 66 mm in the used geometry (from the end of the notch to the bottom of the sample), the reported values indicate that the FPZ could be developed throughout the whole ligament. It is interesting that ℓ_H for sample MZ1-S1450G was in between both assumptions considered for the MZC1-S1450G analysis, and that testing the samples at 600℃ seemed to increase ℓ_H before a considerable drop was seen at 900℃. However, as stated above, the Young's modulus can be severely affected when only one side of the sample is analyzed, and this variation may considerably change the value of ℓ_H for the first five samples. It is worth remembering that zirconia in the mullite-zirconia aggregates may undergo phase transformation between 950℃ and 1150℃, and therefore, properties could drastically change when approaching such temperatures. Unfortunately, it was not possible to perform experiments above 900℃ during this thesis, which remains an interesting perspective for future studies.

5 CONCLUSION AND PERSPECTIVES

Throughout this thesis, the philosophy of the synergetic relationships between experiments and numerical simulations was followed to further understand fracture in refractories. Time was devoted to design and perform experiments optimized for full-field measurements that could be further exploited using robust identification techniques. It started from the choice of material with interesting properties at high temperatures while also providing good contrast for tomography, going up to the development of new experimental setups such as parts for high-temperature WSTs, a furnace allowing for thermomechanical experiments with windows suited for full-field measurements, and performing experiments at 600 ℃, 900 ℃, or at room-temperature *in-situ* inside a tomograph.

All these experiments were then analyzed with full-field measurement techniques (*i.e.,* DIC or DVC), which provided not only insight into crack propagation, the underlying kinematics, the uncertainties, and their relationship with the experimental setup, but also the boundary conditions for trustworthy numerical simulations to best exploit the experimental data. Last, by calibrating few parameters for each case, the numerical results using cohesive elements governed by traction separation laws satisfactorily matched the experimental data (*e.g.,* forces, displacements, gray level residuals), with errors of the order of ten times the experimental standard uncertainty. These results indicate that such simplification of toughening mechanism by the chosen model accurately described the fracture phenomena at the studied scale in monotonic loading conditions.

These results allowed for the investigation of the influence of specimen heat treatment and geometry together with testing conditions on the calibrated parameters. For example, the studied material showed that an increase of less than 4% in the sintering temperature led to fracture energies 25% higher, which is relevant for material and processing parameter selection, and industrial considerations of lifetime, reliability, profitability, and energy reduction. Moreover, when tested at 600 ℃ instead of room temperature, the fracture energy increased by 70%, and increased 60% more when 300 ℃ were added to perform the test at 900 ℃, while the cohesive strength was reduced by 10% and then increased by 80% in the same temperature range. These very different parameters reinforce the idea that materials should be tested in experimental conditions as close as possible to the envisioned application. Otherwise, large errors can be made fully compromising the use of such materials.

Care should also be taken when different geometries are used, such as prismatic or cylindrical samples, since they may also affect the final parameters. The experiments performed inside the tomograph allowed for further verification about the crack path in the bulk of the sample, and how it may affect parameter calibration, by positioning the cohesive elements following the real 3D crack path. For instance, a 25% decrease in the cohesive strength and 10% in fracture energy was observed when compared to a straight crack path assumption.

On the methodological aspect, some contributions of this work can be highlighted. Considerable effort was made to illustrate how experiments when only the NOD was visible could be exploited for FEMU calibrations. It is believed that several experimental setups would provide a limited FOV, especially at higher temperatures, and that it is not always possible to best position the specimen due to setup constraints. Therefore, such methodology may be expanded for other kinds of experiments and for different setups. The construction of the F900 furnace was also another major contribution, since it was designed for allowing the biggest FOV possible, with a fine resolution and visibility from both sides of the specimen. Refractory loading parts were also produced thinking on other experiments such as bending tests, that although not exploited herein, expanded the possible usage of the new equipment for future users.

On the tomographic side, few results were reported in the literature about fracture propagation in brittle materials with the spatial and temporal resolution obtained herein. Now that the WST setup was tested *in-situ* and that the needed geometry was better understood, such usage may be easier in new projects. Consistent numerical simulations when using experimental data from these three different setups also showed the robustness of the FEMU methodology for exploiting full-field data, coupled with beautiful simplicity that provides the potential to be used in similar fashion for very different cases.

For every choice of investigation in this thesis, several interesting points needed to be left aside due to time, resources, and/or expertise constraints. The most critical and straightforward perspective is the study of variability among more samples, since the brittle nature of ceramics is usually attached to higher variability and dependence to defects that are hard to be fully mastered during sample production. Further exploitation of the F900 setup is another possible continuation, together with experiments performed in the similar furnace that is being built in the date of the present writing, aiming to reach up to 1400 °C. For the tomograph setup, P-DVC analyzes would allow to greatly increase the temporal sampling of gathered data, which could even be improved to gather information at optimal angles and time steps. Improvements could also be made in the numerical models when considering cyclic cases (being more representative of applications), *e.g.,* by using a constitutive model coupling damage and plasticity. 3D numerical simulations could be guided by information from both opposite photographed surfaces at high temperatures, while the cohesive elements could be positioned in the crack path gathered *post-mortem* from tomographic analyses. Last, performing WSTs in-situ a tomograph or synchrotron facility at high temperatures could also allow for finer investigations of toughening mechanisms and the interaction of the crack with the microstructure at different temperatures, in which zirconia transformation toughening could be a perfect proof-of-concept.

6 BIBLIOGRAPHY

[1] Lee, W.E., Vieira, W., Zhang, S., Ghanbari Ahari, K., Sarpoolaky, H., Parr, C.. Castable refractory concretes. International Materials Reviews 2001;46(3):145–167.

[2] Luz, A.P., Braulio, M.A.L., Pandolfelli, V.C.. Refractory Castable Engineering; vol. 1. 1 ed.; São Carlos, SP: Göller Verlag; 2015.

[3] Lee, W.E., Moore, R.E.. Evolution of in situ refractories in the 20th century. Journal of the American Ceramic Society 1998;81(6):1385–1410.

[4] Stevens, R.. Zirconia and zirconia ceramics. 2 ed.; Magnesium Elektron Twickenham; 1986.

[5] Wachtman, J.. Materials and Equipment - Whitewares - Refractory Ceramics - Basic Science: Ceramic Engineering and Science Proceedings, Volume 16. No. 1 in Ceramic Engineering and Science Proceedings; Wiley; 2009. ISBN 9780470316306.

[6] Aldunce, P., Blanco, G., Calvin, K., Cheung, W., Dasgupta, D., Denton, F., et al. Climate Change 2023: Synthesis Report. A Report of the Intergovernmental Panel on Climate Change. Contribution of Working Groups I, II and III to the Sixth Assessment Report of the Intergovernmental Panel on Climate Change. IPCC, Geneva, Switzerland 2023;.

[7] Nouri-Khezrabad, M., Braulio, M.A.L., Pandolfelli, V.C., Golestani-Fard, F., Rezaie, H.R.. Nano-bonded refractory castables. Ceramics International 2013;39(4):3479–3497.

[8] Roy, J., Chandra, S., Maitra, S.. Nanotechnology in castable refractory. Ceramics International 2019;45(1):19–29.

[9] Launey, M.E., Ritchie, R.O.. On the fracture toughness of advanced materials. Advanced Materials 2009;21(20):2103–2110.

[10] Studart, A.R.. Bioinspired ceramics: Turning brittleness into toughness. Nature materials 2014;13(5):433–435.

[11] Pivinskii, Y.E.. Cement-free refractory concretes. Part 1. General informa-

tion. HCBS and ceramic concretes. Refractories and Industrial Ceramics 2020;60(5):430–438.

[12] Bezerra, B.P., Morelli, M.R., Luz, A.P.. Design, characterization and incorporation of geopolymer binders in refractory ceramic compositions. International Journal of Applied Ceramic Technology 2023;:1–16.

[13] Harbison-Walker, . Handbook of Refractory Practice. Harbison-Walker Refractories Company; 2005.

[14] Dörre, E., Hübner, H.. Alumina: Processing, Properties and Applications. Springer-Verlag Berlin Heidelberg; 1984.

[15] Wolf, C., Kauermann, R., Hübner, H., Rodrigues, J.A., Pandolfelli, V.C.. Effect of mullite-zirconia additions on the creep behaviour of high-alumina refractories. Journal of the European Ceramic Society 1995;15(9):913–920.

[16] Ferrari, C.R., Rodrigues, J.A.. Refratários de alumina contendo agregado de mulita-zircônia: aspectos microestruturais. Cerâmica 2000;46(298):83.

[17] Subbarao, E.C., Maiti, H.S., Srivastava, K.K.. Martensitic transformation in zirconia. Physica status solidi (a) 1974;21(1):9–40.

[18] Dematteis, N., Giordan, D.. Comparison of digital image correlation methods and the impact of noise in geoscience applications. Remote Sensing 2021;13(2):327.

[19] Smith, K.C.A., Oatley, C.W.. The scanning electron microscope and its fields of application. British Journal of Applied Physics 1955;6(11):391.

[20] Shindo, D., Oikawa, T.. Analytical Electron Microscopy for Materials Science; chap. 4. Energy Dispersive X-ray Spectroscopy. Tokyo: Springer Japan; 2002, p. 81–102.

[21] Vermeij, T., Verstijnen, J.A.C., Ramirez y Cantador, T.J.J., Blaysat, B., Neggers, J., Hoefnagels, J.P.M.. A nanomechanical testing framework yielding front&rear-sided, high-resolution, microstructure-correlated semdic strain fields. Experimental Mechanics 2022;62(9):1625–1646.

[22] Radon, J.. On the determination of functions from their integral val-

ues along certain manifolds. IEEE Transactions on Medical Imaging 1986;5(4):170–176.

[23] Thompson, A.C., Llacer, J., Finman, L.C., Hughes, E.B., Otis, J.N., Wilson, S., et al. Computed tomography using synchrotron radiation. Nuclear Instruments and Methods in Physics Research 1984;222(1-2):319–323.

[24] Kinney, J.H., Nichols, M.C.. X-ray tomographic microscopy (XTM) using synchrotron radiation. Annual review of materials science 1992;22(1):121–152.

[25] Barsoum, M.W.. Fundamentals of ceramics. CRC Press; 2002.

[26] Callister, W.D., Rethwisch, D.G.. Materials Science and Engineering - An Introduction. 8 ed.; 2009.

[27] Ritchie, R.O.. The conflicts between strength and toughness. Nature materials 2011;10(11):817.

[28] Steinbrech, R.W.. Toughening mechanisms for ceramic materials. Journal of the European Ceramic Society 1992;10(3):131–142.

[29] Miyaji, D.Y., Tonnesen, T., Rodrigues, J.A.. Fracture energy and thermal shock damage resistance of refractory castables containing eutectic aggregates. Ceramics International 2014;40(9, Part B):15227–15239.

[30] Hannink, R.H.J., Kelly, P.M., Muddle, B.C.. Transformation toughening in zirconia-containing ceramics. Journal of the American Ceramic Society 2000;83(3):461–487.

[31] Garvie, R.C., Hannink, R.H., Pascoe, R.T.. Ceramic steel? Nature 1975;258(5537):703–704.

[32] Yang, L.W., Liu, H.T., Jiang, R., Sun, X., Mao, W.G., Cheng, H.F., et al. Weak interface dominated high temperature fracture strength of carbon fiber reinforced mullite matrix composites. Journal of the European Ceramic Society 2017;37(8):2991–2996.

[33] Pelissari, P.I.B.G.B., Bouville, F., Pandolfelli, V.C., Carnelli, D., Giuliani, F., Luz, A.P., et al. Nacre-like ceramic refractories for high temperature applications. Journal of the European Ceramic Society 2018;38(4):2186–

2193.

[34] Wong-Ng, W.. Transformation toughening. International Tables for Crystallography 2019;H:822.

[35] Tschegg, E.. Prüfeinrichtung zur Ermittlung von bruchmechanishen Kennwerten sowie hiefür geeignete, Prüfkörper, Austrian Pat. AT 390328B, registered. 1986.

[36] Brühwiler, E., Wittmann, F.H.. The wedge splitting test, a new method of performing stable fracture mechanics tests. Engineering Fracture Mechanics 1990;35(1-3):117–125.

[37] Ribeiro, S., Exposito, C.C.D., Rodrigues, J.A.. Projeto, adaptação, instalação e testes preliminares para um sistema de medida de energia de fratura de materiais cerâmicos pelo método da cunha. Cerâmica 2008;54:418–426.

[38] Jailin, C., Bouterf, A., Vargas, R., Hild, F., Roux, S.. Sub-minute In Situ Fracture Test in a Laboratory CT Scanner. Integrating Materials and Manufacturing Innovation 2019;8(3):413–422.

[39] Ribeiro, S., Rodrigues, J.A.. The influence of microstructure on the maximum load and fracture energy of refractory castables. Ceramics International 2010;36(1):263–274.

[40] Harmuth, H., Rieder, K., Krobath, M., Tschegg, E.. Investigation of the nonlinear fracture behaviour of ordinary ceramic refractory materials. Materials Science and Engineering: A 1996;214(1-2):53–61.

[41] Buchebner, G., Molinari, T., Rumpf, D.. Developing basic high-performance products for furnaces in the nonferrous metals industries. JOM 2000;52(2):68–72.

[42] Brochen, E., Dannert, C., Quirmbach, P.. Thermo-mechanical characterisation of magnesia-carbon refractories by means of wedge splitting test under controlled atmosphere at high-temperature. In: Proceedings of the Unified International Technical Conference on Refractories (UNITECR 2013). Wiley Online Library; 2014, p. 53–58.

[43] Sutton, M.A., Orteu, J.J., Schreier, H.. Image correlation for shape, motion and deformation measurements: Basic concepts, theory and applications. Springer Science & Business Media; 2009.

[44] Sutton, M.A.. Computer vision-based, noncontacting deformation measurements in mechanics: A generational transformation. Applied Mechanics Reviews 2013;65(AMR-13-1009, 050802).

[45] McNeill, S., Peters, W., Sutton, M.. Estimation of stress intensity factor by digital image correlation. Engineering Fracture Mechanics 1987;28(1):101–112.

[46] Abanto-Bueno, J., Lambros, J.. Investigation of crack growth in functionally graded materials using digital image correlation. Engineering Fracture Mechanics 2002;69:1695–1711.

[47] Forquin, P., Rota, L., Charles, Y., Hild, F.. A method to determine the toughness scatter of brittle materials. International Journal of Fracture 2004;125(1):171–187.

[48] Mathieu, F., Hild, F., Roux, S.. Identification of a crack propagation law by digital image correlation. International Journal of Fatigue 2012;36(1):146–154.

[49] Saracura, R.G.M., Canto, R.B., Pandolfelli, V.C., Schmitt, N., Hild, F.. Surface crack network detection on MgO-based refractory castable by digital image correlation. China's Refractories 2015;24(1):32–37.

[50] Besnard, G., Hild, F., Roux, S.. "Finite-Element" displacement fields analysis from digital images: Application to Portevin-Le Chatelier bands. Experimental Mechanics 2006;46(6):789–803.

[51] Leclerc, H., Neggers, J., Mathieu, F., Roux, S., Hild, F.. Correli 3.0. 2015. IDDN.FR.001.520008.000.S.P.2015.000.31500.

[52] Neggers, J., Mathieu, F., Hild, F., Roux, S.. Simultaneous full-field multi-experiment identification. Mechanics of Materials 2019;.

[53] Vargas, R., Neggers, J., Canto, R.B., Rodrigues, J.A., Hild, F.. Analysis of wedge splitting test on refractory castable via integrated DIC. Journal of

the European Ceramic Society 2016;36(16):4309–4317.

[54] Vargas, R., Neggers, J., Canto, R.B., Rodrigues, J.A., Hild, F.. Comparison of two full-field identification methods for the wedge splitting test on a refractory. Journal of the European Ceramic Society 2018;38(16):5569 – 5579.

[55] Hild, F., Roux, S.. Digital Image Correlation. Weinheim (Germany): Wiley-VCH; 2012, p. 183–228.

[56] Hild, F., Roux, S.. Comparison of local and global approaches to digital image correlation. Experimental Mechanics 2012;52(9):1503–1519.

[57] Belrhiti, Y., Pop, O., Germaneau, A., Doumalin, P., Dupré, J.C., Harmuth, H., et al. Investigation of the impact of micro-cracks on fracture behavior of magnesia products using wedge splitting test and digital image correlation. Journal of the European Ceramic Society 2015;35(2):823–829.

[58] Dai, Y., Gruber, D., Harmuth, H.. Observation and quantification of the fracture process zone for two magnesia refractories with different brittleness. Journal of the European Ceramic Society 2017;37(6):2521–2529.

[59] Dai, Y., Gruber, D., Harmuth, H.. Determination of the fracture behaviour of MgO-refractories using multi-cycle wedge splitting test and digital image correlation. Journal of the European Ceramic Society 2017;37(15):5035–5043.

[60] Dupré, J.C., Doumalin, P., Belrhiti, Y., Khlifi, I., Pop, O., Huger, M.. Detection of cracks in refractory materials by an enhanced digital image correlation technique. Journal of Materials Science 2018;53(2):977–993.

[61] Dai, Y., Yin, Y., Xu, X., Jin, S., Li, Y., Harmuth, H.. Effect of the phase transformation on fracture behaviour of fused silica refractories. Journal of the European Ceramic Society 2018;38(16):5601–5609.

[62] Pan, L., He, Z., Li, Y., Zhu, T., Wang, Q., Li, B., et al. Investigation of fracture behavior of cement-bonded corundum castables using wedge splitting test and digital image correlation method. Journal of the European Ceramic Society 2019;.

[63] Khlifi, I., Pop, O., Dupré, J.C., Doumalin, P., Huger, M.. Investigation of microstructure-property relantionships of magnesia-hercynite refractory composites by a refined digital image correlation technique. Journal of the European Ceramic Society 2019;39(13):3893–3902.

[64] Dai, Y., Li, Y., Xu, X., Zhu, Q., Yin, Y., Ge, S., et al. Characterization of tensile failure behaviour of magnesia refractory materials by a modified dog-bone shape direct tensile method and splitting tests. Ceramics International 2019;.

[65] Poirier, J., Blond, E., Bilbao, E., Michel, R., Coulon, A., Gillibert, J., et al. New advances in the laboratory characterization of refractories: testing and modelling. Metallurgical Research & Technology 2017;114(6):610.

[66] Lyons, J., Liu, J., Sutton, M.. High-temperature deformation measurements using digital-image correlation. Experimental Mechanics 1996;36(1):64–70.

[67] Berny, M., Archer, T., Mavel, A., Beauchêne, P., Roux, S., Hild, F.. On the analysis of heat haze effects with spacetime DIC. Optics and Lasers in Engineering 2018;111:135–153.

[68] Archer, T., Beauchêne, P., Huchette, C., Hild, F.. Global digital image correlation up to very high temperatures with grey level corrections. Measurement Science and Technology 2019;31(2):024003.

[69] Doitrand, A., Estevez, R., Thibault, M., Leplay, P.. Fracture and cohesive parameter identification of refractories by Digital Image Correlation up to 1200 ℃. Experimental Mechanics 2020;60(5):577–590.

[70] Vargas, R., Neggers, J., Canto, R.B., Rodrigues, J.A., Hild, F.. Analysis of a castable refractory using the wedge splitting test and cohesive zone model. Journal of the European Ceramic Society 2019;39(13):3903–3914.

[71] Vargas, R., Tsitova, A., Bernachi-Barbe, F., Bary, B., Canto, R.B., Hild, F.. On the identification of cohesive zone model for curved crack in mortar. Strain 2020;56(6):e12364.

[72] Buljac, A., Jailin, C., Mendoza, A., Neggers, J., Taillandier-Thomas,

T., Bouterf, A., et al. Digital volume correlation: review of progress and challenges. Experimental Mechanics 2018;58(5):661–708.

[73] Rannou, J., Limodin, N., Réthoré, J., Gravouil, A., Ludwig, W., Baïetto-Dubourg, M.C., et al. Three dimensional experimental and numerical multiscale analysis of a fatigue crack. Computer methods in applied mechanics and engineering 2010;199(21-22):1307–1325.

[74] Lachambre, J., Réthoré, J., Weck, A., Buffiere, J.Y.. Extraction of stress intensity factors for 3D small fatigue cracks using digital volume correlation and X-ray tomography. International Journal of Fatigue 2015;71:3–10.

[75] Hild, F., Bouterf, A., Chamoin, L., Leclerc, H., Mathieu, F., Neggers, J., et al. Toward 4D mechanical correlation. Advanced Modeling and Simulation in Engineering Sciences 2016;3(1):17.

[76] Saucedo-Mora, L., Mostafavi, M., Khoshkhou, D., Reinhard, C., Atwood, R., Zhao, S., et al. Observation and simulation of indentation damage in a SiC–SiC fibre ceramic matrix composite. Finite Elements in Analysis and Design 2016;110:11–19.

[77] Saucedo-Mora, L., Zou, C., Lowe, T., Marrow, T.J.. Three-dimensional measurement and cohesive element modelling of deformation and damage in a 2.5-dimensional woven ceramic matrix composite. Fatigue & Fracture of Engineering Materials & Structures 2017;40(5):683–695.

[78] Mostafavi, M., McDonald, S.A., Mummery, P.M., Marrow, T.J.. Observation and quantification of three-dimensional crack propagation in polygranular graphite. Engineering Fracture Mechanics 2013;110:410–420.

[79] Mostafavi, M., Baimpas, N., Tarleton, E., Atwood, R.C., McDonald, S.A., Korsunsky, A.M., et al. Three-dimensional crack observation, quantification and simulation in a quasi-brittle material. Acta Materialia 2013;61(16):6276–6289.

[80] Fish, J., Belytschko, T.. A first course in finite elements. John Wiley & Sons Limited; 2007.

[81] Clough, R.W.. Early history of the finite element method from the view point

of a pioneer. International Journal for Numerical Methods in Engineering 2004;60(1):283–287.

[82] Bathe, K.J.. Finite element procedures. Klaus-Jurgen Bathe; 2006.

[83] Bower, A.F.. Applied mechanics of solids. CRC press; 2009.

[84] Cook, R.D., Malkus, D.S., Plesha, M.E., Witt, R.J.. Concepts and Applications of Finite Element Analysis. 4 ed.; Wiley; 2001.

[85] Réthoré, J., Roux, S., Hild, F.. An extended and integrated digital image correlation technique applied to the analysis of fractured samples: The equilibrium gap method as a mechanical filter. European Journal of Computational Mechanics 2009;18(3-4):285–306.

[86] Tomičevć, Z., Hild, F., Roux, S.. Mechanics-aided digital image correlation. The Journal of Strain Analysis for Engineering Design 2013;48(5):330–343.

[87] Mathieu, F., Leclerc, H., Hild, F., Roux, S.. Estimation of elastoplastic parameters via weighted FEMU and integrated-DIC. Experimental Mechanics 2015;55(1):105–119.

[88] Sciuti, V.F., Vargas, R., Canto, R.B., Hild, F.. Pyramidal adaptive meshing for Digital Image Correlation dealing with cracks. Engineering Fracture Mechanics 2021;256:107931. doi:`10.1016/j.engfracmech.2021.107931`.

[89] Hild, F., Misra, A., dell'Isola, F.. Multiscale DIC applied to pantographic structures. Experimental Mechanics 2021;61(2):431–443.

[90] Henneberg, D., Ricoeur, A., Judt, P.. Multiscale modeling for the simulation of damage processes at refractory materials under thermal shock. Computational materials science 2013;70:187–195.

[91] Jin, S., Gruber, D., Harmuth, H.. Determination of Young's modulus, fracture energy and tensile strength of refractories by inverse estimation of a wedge splitting procedure. Engineering Fracture Mechanics 2014;116:228 – 236.

[92] Dai, Y., Gruber, D., Jin, S., Harmuth, H.. Modelling and inverse investigation of the fracture process for a magnesia spinel refractory us-

ing a heterogeneous continuum model. Engineering Fracture Mechanics 2017;182:438–448.

[93] Maginador, R.V.. Analysis of crack propagation in the wedge splitting test via digital image correlation and finite element analyses. Master's thesis; Federal University of São Carlos (UFSCar) - Brazil; 2019.

[94] Hillerborg, A., Modéer, M., Petersson, P.E.. Analysis of crack formation and crack growth in concrete by means of fracture mechanics and finite elements. Cement and Concrete Research 1976;6(6):773–782.

[95] Elices, M., Guinea, G., Gómez, J., Planas, J.. The cohesive zone model: advantages, limitations and challenges. Engineering Fracture Mechanics 2002;69:137–163.

[96] Duarte, C.A., Oden, J.T.. An h-p adaptive method using clouds. Computer Methods in Applied Mechanics and Engineering 1996;139(1):237–262. doi:`10.1016/S0045-7825(96)01085-7`.

[97] Melenk, J.M., Babuška, I.. The partition of unity finite element method: Basic theory and applications. Computer Methods in Applied Mechanics and Engineering 1996;139(1):289–314. doi:`10.1016/S0045-7825(96)01087-0`.

[98] Belytschko, T., Black, T.. Elastic crack growth in finite elements with minimal remeshing. International Journal for Numerical Methods in Engineering 1999;45(5):601–620. doi:`10.1002/(SICI)1097-0207(19990620)45:5<601::AID-NME598>3.0.CO;2-S`.

[99] Moës, N., Dolbow, J., Belytschko, T.. A finite element method for crack growth without remeshing. International Journal for Numerical Methods in Engineering 1999;46(1):131–150. doi:`10.1002/(SICI)1097-0207(19990910)46:1<131::AID-NME726>3.0.CO;2-J`.

[100] Belytschko, T., Gracie, R., Ventura, G.. A review of extended/generalized finite element methods for material modeling. Modelling and Simulation in Materials Science and Engineering 2009;17(4):043001. doi:`10.1088/0965-0393/17/4/043001`.

[101] Park, K., Paulino, G.H., Roesler, J.R.. A unified potential-based cohesive

model of mixed-mode fracture. Journal of the Mechanics and Physics of Solids 2009;57(6):891–908.

[102] Park, K., Choi, H., Paulino, G.H.. Assessment of cohesive traction-separation relationships in ABAQUS: A comparative study. Mechanics Research Communications 2016;78:71–78.

[103] Park, K., Paulino, G.H.. Computational implementation of the PPR potential-based cohesive model in ABAQUS: educational perspective. Engineering Fracture Mechanics 2012;93:239–262.

[104] Lee, J., Fenves, G.L.. Plastic-damage model for cyclic loading of concrete structures. Journal of engineering mechanics 1998;124(8):892–900.

[105] Lubliner, J., Oliver, J., Oller, S., Oñate, E.. A plastic-damage model for concrete. International Journal of solids and structures 1989;25(3):299–326.

[106] Kavanagh, K.T., Clough, R.W.. Finite element applications in the characterization of elastic solids. International Journal of Solids and Structures 1971;7(1):11–23.

[107] Avril, S., Bonnet, M., Bretelle, A.S., Grédiac, M., Hild, F., Ienny, P., et al. Overview of identification methods of mechanical parameters based on full-field measurements. Experimental Mechanics 2008;48:381–402.

[108] Pagnacco, E., Caro-Bretelle, A.S., Ienny, P.. Full-Field Measurements and Identification in Solid Mechanics; chap. 9. Parameter Identification from Mechanical Field Measurements using Finite Element Model Updating Strategies. Wiley-Blackwell; 2012, p. 247–274.

[109] Neggers, J., Allix, O., Hild, F., Roux, S.. Big data in experimental mechanics and model order reduction: today's challenges and tomorrow's opportunities. Archives of Computational Methods in Engineering 2018;25:143–164.

[110] Roux, S., Hild, F.. Optimal procedure for the identification of constitutive parameters from experimentally measured displacement fields. International Journal of Solids and Structures 2020;184:14–23.

[111] Neggers, J., Mathieu, F., Hild, F., Roux, S., Swiergiel, N.. Improving full-field identification using progressive model enrichments. International Journal of Solids and Structures 2017;118:213–223.

[112] Pierron, F., Grédiac, M.. Towards Material Testing 2.0. A review of test design for identification of constitutive parameters from full-field measurements. Strain 2021;57(1):e12370.

[113] Pierron, F.. Material Testing 2.0: A brief review. Strain 2023;59(3):e12434.

[114] Greca, M.C., Emiliano, J.V., Segadães, A.M.. Revised phase equilibrium relationships in the system Al_2O_3-ZrO_2-SiO_2. Journal of the European Ceramic Society 1992;9(4):271–283.

[115] Srinivasan, R., De Angelis, R.J., Ice, G., Davis, B.H.. Identification of tetragonal and cubic structures of zirconia using synchrotron x-radiation source. Journal of materials research 1991;6:1287–1292.

[116] Vargas, R., Pinelli, X., Smaniotto, B., Hild, F., Canto, R.B.. On the effect of sintering temperature on fracture energy of Alumina-Mullite-Zirconia castable at 600℃. Journal of the European Ceramics Society 2021;41(7):4406–4418.

[117] Vargas, R., Canto, R.B., Hild, F.. Cohesive properties of refractory castable at 600℃: Effect of sintering and testing temperature. Journal of the European Ceramic Society 2022;42(14):6733–6749.

[118] Vargas, R., Canto, R.B., Hild, F.. Fracture energy evaluation of refractories in wedge splitting tests from notch opening displacements. Journal of the European Ceramic Society 2021;41(10):5367–5379.

[119] Cabrelon, M.D., Pereira, A.H.A., Medeiros, J., Toledo-Filho, R.D., Rodrigues, J.A.. Efeito do tempo de exposição a uma atmosfera coqueificante na microestrutura e nas propriedades de um concreto refratário usado na indústria petroquímica. Cerâmica 2012;58:195–204.

[120] Miyaji, D.Y., Otofuji, C.Z., Cabrelon, M.D., Medeiros, J., Rodrigues, J.A.. The coke effect on the fracture energy of a refractory castable for the petrochemical industry. In: Proceedings of the Unified International Technical

Conference on Refractories (UNITECR 2013). Wiley Online Library; 2014, p. 1111–1116.

[121] Pereira, A.H.A., Miyaji, D.Y., Cabrelon, M.D., Medeiros, J., Rodrigues, J.A.. A study about the contribution of the α-β phase transition of quartz to thermal cycle damage of a refractory used in fluidized catalytic cracking units. Cerâmica 2014;60:449–456.

[122] Vargas, R., Canto, R., Hild, F.. On the calibration of cohesive parameters for refractories from notch opening displacements in wedge splitting tests. Journal of the European Ceramic Society 2021;41(14):7348–7361.

[123] Vargas, R., Canto, R.B., Hild, F., Roux, S.. On accounting for speckle extinction via DIC and PCA. Optics and Lasers in Engineering 2022;149:106813.

[124] Vargas, R., Canto, R.B., Smaniotto, B., Hild, F.. Calibration of cohesive parameters for a castable refractory using 4D tomographic data and realistic crack path from in-situ wedge splitting test. Journal of the European Ceramic Society 2023;43(2):676–691.

[125] Kosin, V., Fau, A., Jailin, C., Smaniotto, B., Wick, T., Hild, F.. A projection-based approach to extend digital volume correlation for 4D spacetime measurements. Comptes Rendus Mécanique 2023;351(1-2):265–280.

[126] Jailin, C., Bouterf, A., Poncelet, M., Roux, S.. In situ µ CT-scan mechanical tests: fast 4D mechanical identification. Experimental Mechanics 2017;57:1327–1340.

[127] Jailin, C., Buljac, A., Bouterf, A., Hild, F., Roux, S.. Fast 4D tensile test monitored via X-CT: Single projection based Digital Volume Correlation dedicated to slender samples. Journal of Strain Analysis for Engineering Design 2018;53(7):473–484.

[128] Mandić, A., Kosin, V., Jailin, C., Tomičević, Z., Smaniotto, B., Hild, F.. Damage Detection in a Polymer Matrix Composite from 4D Displacement Field Measurements. Materials 2023;16(18):6300.

[129] Leclerc, H., Neggers, J., Mathieu, F., Hild, F., Roux, S.. Correli 3.0. IDDN.FR.001.520008.000.S.P.2015.000.31500; Agence pour la Protection des Programmes, Paris (France); 2015.

[130] Leplay, P., Lafforgue, O., Hild, F.. Analysis of asymmetrical creep of a ceramic at 1350 ℃ by Digital Image Correlation. Journal of the American Ceramic Society 2015;98(7):2240–2247.

[131] Auger, P., Lavigne, T., Smaniotto, B., Spagnuolo, M., Dell'Isola, F., Hild, F.. Poynting effects in pantographic metamaterial captured via multiscale DVC. The Journal of Strain Analysis for Engineering Design 2021;56(7):462–477.

[132] Hild, F., Bouterf, A., Chamoin, L., Mathieu, F., Neggers, J., Pled, F., et al. Toward 4d mechanical correlation. Advanced Modeling and Simulation in Engineering Sciences 2016;3(1):1–26.

[133] Spring, D.W., Paulino, G.H.. A growing library of three-dimensional cohesive elements for use in abaqus. Engineering Fracture Mechanics 2014;126:190–216.

[134] Lipow, P.R., Schoenberg, I.J.. Cardinal interpolation and spline functions. III. Cardinal Hermite interpolation. Linear Algebra and its Applications 1973;6:273–304.

[135] Wittmann, F.H., Slowik, V., Alvaredo, A.M.. Probabilistic aspects of fracture energy of concrete. Materials and Structures 1994;27(9):499–504.

[136] Ferrari, C.R., Rodrigues, J.A.. Microstructural features of alumina refractories with mullite-zirconia aggregates. Boletin-Sociedad Española de Ceramica y Vidrio 2003;42(1):15–20.

[137] Hasselman, D.P.H.. Unified theory of thermal shock fracture initiation and crack propagation in brittle ceramics. Journal of the American Ceramic society 1969;52(11):600–604.

[138] Salvini, V.R., Pandolfelli, V.C., Bradt, R.C.. Extension of hasselman's thermal shock theory for crack/microstructure interactions in refractories. Ceramics International 2012;38(7):5369–5375.

[139] Harmuth, H.. Stability of crack propagation associated with fracture energy determined by wedge splitting specimen. Theoretical and Applied Fracture Mechanics 1995;23:103–108.

[140] Rieder, K.A., Tschegg, E.K., Harmuth, H.. Notch sensitivity of ordinary ceramic refractory materials. Journal of Materials Science Letters 1998;17(8):675–678.

[141] Grasset-Bourdel, R., Alzina, A., Huger, M., Chotard, T., Emler, R., Gruber, D., et al. Tensile behaviour of magnesia-spinel refractories: Comparison of tensile and wedge splitting tests. Journal of the European Ceramic Society 2013;33(5):913–923.

[142] Saucedo, L., Rena, C.Y., Ruiz, G.. Fully-developed FPZ length in quasi-brittle materials. International Journal of Fracture 2012;178(1-2):97–112.

[143] Dong, W., Zhou, X., Wu, Z.. On fracture process zone and crack extension resistance of concrete based on initial fracture toughness. Construction and Building Materials 2013;49:352–363.

APPENDIX A: RÉSUMÉ SUBSTANTIEL (LONG ABSTRACT IN FRENCH)

Cette thèse a pour objectif le développement de méthodes numériques et expérimentales couplées pour la caractérisation thermomécanique des réfractaires, une classe de matériaux qui maintiennent leurs propriétés, même sous ambiances très agressives. Les réfractaires sont essentiels pour de nombreuses industries de base et sont majoritairement utilisés à des températures très élevées dans des procédés souvent très énergivores. Leur formulation et leur caractérisation menée sous ces conditions d'application deviennent cruciales, par exemple, pour l'optimisation énergétique ou pour réduire les risques avec une meilleure prévision de la défaillance. La complexité microstructurale des réfractaires fait que la simulation directe et complète des phénomènes de fissuration, sans une base expérimentale, n'est pas encore possible. Bien que ces matériaux soient très étudiés, peu d'essais de fissuration à hautes températures ont été analysés avec des techniques de mesure de champ (qui fournissent des données très nombreuses pour la validation et l'identification des modèles numériques). Ce travail propose de combler, en partie, ces lacunes avec l'analyse d'essais de fendage à hautes températures en utilisant deux fours, le premier allant jusqu'à 600℃ et le second jusqu'à 900℃ avec un suivi par corrélation d'images. Dans ces approches, les mesures de champ donnent accès à la cinématiques surfacique. Dans la littérature, il existe très peu d'essais de fissuration sur réfractaires avec un suivi par rayons-X, ce qui permet l'analyse du chemin de fissuration à l'intérieur de l'échantillon. Dans ces travaux, des essais in situ, à température ambiante, ont été menés et ont été analysés par corrélation d'images volumiques.

Un réfractaire alumineux avec des agrégats de mullite-zircone a été sélectionné comme matériau modèle pour ces investigations, avec une augmentation anticipée de la ténacité avec la température et un bon contraste pour les images obtenues par tomographie aux rayons-X. Avec ces analyses, il devient possible de guider et de valider des simulations de propagation de fissure avec des codes d'éléments finis. Des éléments cohésifs sont utilisés pour décrire la fissuration dont les paramètres sont identifiés par recalage de modèles éléments finis (FEMU), par minimisation des différences entre des données expérimentales et leurs homologues numériques. Des développements méthodologiques spécifiques ont été nécessaires pour chaque essai traité. Les images prises pendant les essais dans le four à 600 ℃ avaient un champ de vision réduit qui ne permettait pas la visualisation de la région d'application d'effort. Ceci a motivé une étude sur l'extrapolation des ouvertures proches de l'entaille de l'échantillon pour leur utilisation comme conditions aux limites des simulations par éléments finis. Les résultats obtenus avec ces premiers essais ont guidé la conception d'un second four pour mener des essais jusqu'à 900 ℃. Ce four, construit pendant cette thèse, permet la visualisation de deux surfaces opposées de l'échantillon et la quantification des désalignements qui peuvent biaiser l'identification de paramètres thermomécaniques. Enfin, des essais in situ, à l'intérieur d'un tomographe de laboratoire, ont été menés sur des échantillons cylindriques afin de minimiser les artefacts de reconstruction à partir des radiographies-X.

Les paramètres de fissuration ont été identifiés pour ces différentes configurations et sont discutés en considérant la géométrie des échantillons, le chemin de fissuration, la température de frittage et celle des essais. Pour le matériau étudié et les conditions testées, l'énergie de fissuration augmente considérablement lorsque la température de l'essai augmente, ainsi que la température de frittage, en comparant les résultats des échantillons frittés à 1400 ℃ et ceux frittés à 1450 ℃. Les données obtenues dans le tomographe indiquent qu'on peut obtenir des valeurs des paramètres plus élevés quand on ne connaît pas le vrai chemin de fissuration. La fissuration est ainsi mieux quantifiée dans le volume de l'échantillon et dans des environnements similaires aux conditions d'utilisation.

ANNEX A: SUPERCASTIBAR 85 MZ DATASHEET

IBAR **Indústrias Brasileiras de Artigos Refratários IBAR Ltda.**

FOLHA DE DADOS TÉCNICOS

NOME PRODUTO	**SUPERCASTIBAR 85 MZ**
DESCRIÇÃO DO PRODUTO	Concreto refratário aluminoso de baixo teor de cimento contento mulita zircônia fundida.
PRINCIPAL APLICAÇÃO	Uso geral.
METODO DE APLICAÇÃO	Vibrado.
EMBALAGEM	Saco de papel multifolhado.
IDENTIFICAÇÃO	Rótulo contendo: nome do produto, nome do cliente, quantidade, peso (bruto/líquido), nº do lote, data de fabricação e prazo de estocagem.
ARMAZENAMENTO	Manter em local coberto, arejado e protegido da umidade.
PRAZO DE ESTOCAGEM	6 meses (armazenado em condições adequadas).

COMPOSIÇÃO QUÍMICA	Unidade	Valor Típico
SiO_2	%	4,0
Al_2O_3	%	86,0
Fe_2O_3	%	0,1
CaO	%	1,8
ZrO_2	%	8,0

PROPRIEDADES	Unidade	Valor Típico
Qde de Água p/ Mistura	(%)	5,0
Tempo de Pega	(min)	100
Densidade de Massa Aparente (110ºCx24h)	(g/cm^3)	3,00
Densidade de Massa Aparente (1000ºCx5h)	(g/cm^3)	2,95
Densidade de Massa Aparente (1450ºCx5h)	(g/cm^3)	3,00
Variação Linear Dimensional (110ºCx24h)	(%)	0,0
Variação Linear Dimensional (1000ºCx5h)	(%)	0,0
Variação Linear Dimensional (1450ºCx5h)	(%)	-0,3
Resistência a Compressão (110ºCx24h)	(MPa)	37,0
Resistência a Compressão (1000ºCx5h)	(MPa)	54,0
Resistência a Compressão (1450ºCx5h)	(MPa)	110,0
Quantidade de Material Requerido	(Kg/m^3)	3040

1-Os ensaios são executados conforme Método Interno da IBAR, que são baseados nas normas ABNT, ASTM, DIN e/ou Normas de Cliente.
2-Para aplicação e manuseio, consultar a Folha de Instrução de Aplicação e a Ficha de Informações de Segurança de Produtos Químicos (FISPQ).
3-A Folha de Dados Técnicos refere-se a dados obtidos em laboratório.
4-A IBAR se reserva ao direito de realizar alterações na Folha de Dados Técnicos sem previa comunicação.
5-A Temperatura Máxima de Uso é um valor de referência obtido através do ensaio da variação linear dimensional (ABNT NBR 8385). Ela depende das condições físicas, químicas e térmicas da aplicação desse produto, portanto, não deve ser utilizada como especificação.

ANNEX B: X-RAY DIFFRACTOMETRY OF THE MULLITE-ZIRCONIA AGGREGATES

```
              **********     SEARCH / MATCH RESULT     **********
<Unknown Data>
 Group Name  : DRX_Fevereiro_2024
 Data Name   : 1609426B_MUZR
 File Name   : 1609426B_MUZR.PKK
 Sample Name : (Elfusa)
 Comment     : FX 18 MF
 Date & Time : 02-29-24 22:07:01
<Raw Data>
```

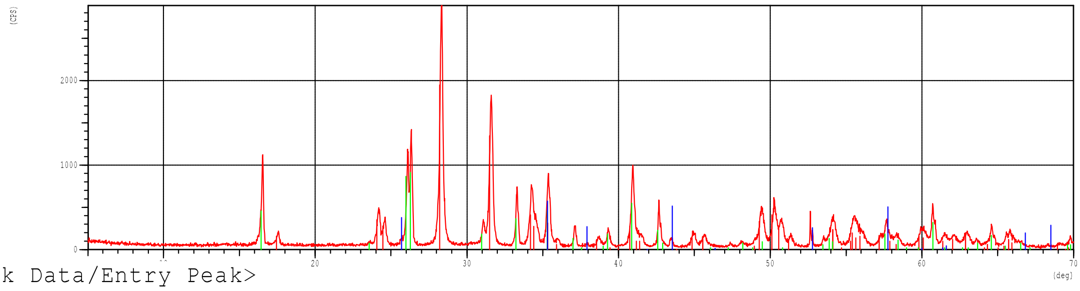

```
<Peak Data/Entry Peak>
```

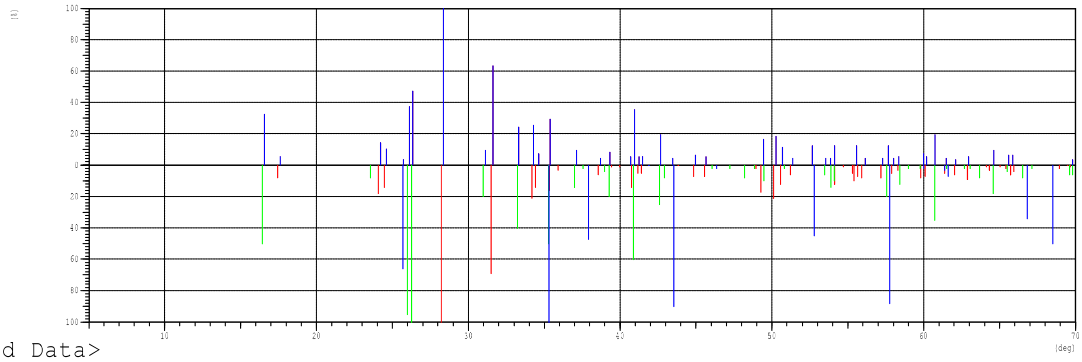

```
<Card Data>
```

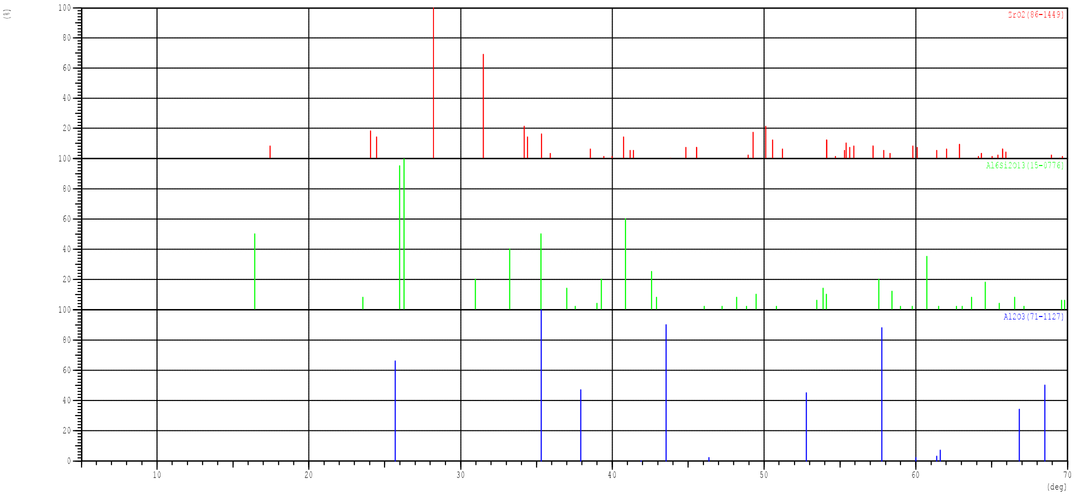

```
              **********     SEARCH / MATCH RESULT     **********
 Group Name  : DRX_Fevereiro_2024
 Data Name   : 1609426B_MUZR
 File Name   : 1609426B_MUZR.PKK
 Sample Name : (Elfusa)
 Comment     : FX 18 MF
<Entry Card>
No.   Card      Chemical Formula                     S        L          d     I     R
                Chemical Name (Mineral Name)                 Dx     WT%    S.G.
 1 🟥 86-1449 ZrO2                              0.871 0.635(33/100) 0.755 0.763 0.366
                ( Baddeleyite )                             5.82          P21/a
 2 🟩 15-0776 Al6Si2O13                         0.551 0.684(26/63) 0.790 0.750 0.000
               Aluminum Silicate ( Mullite, syn )           3.17          Pbam
 3 🟦 71-1127 Al2O3                             0.165 0.615( 8/25) 0.785 0.450 0.217
                ( Corundum )                                4.04          R-3c
```